

ORNL/TM-2015/59531/
REV-01

The Effect of Shallow Inside-Surface-Breaking Flaws on the Probability of Brittle Fracture of Reactors Subjected to Postulated and Actual Operational Cool-Down Transients: A Status Report



Approved for public release.
Distribution is unlimited.

ORNL

B. Richard Bass
Terry L. Dickson
Paul T. Williams
Hilda B. Klasky

Professional Consulting Services

Robert H. Dodds, Jr.

February 2016

DOCUMENT AVAILABILITY

Reports produced after January 1, 1996, are generally available free via US Department of Energy (DOE) SciTech Connect.

Website <http://www.osti.gov/scitech/>

Reports produced before January 1, 1996, may be purchased by members of the public from the following source:

National Technical Information Service
5285 Port Royal Road
Springfield, VA 22161
Telephone 703-605-6000 (1-800-553-6847)
TDD 703-487-4639
Fax 703-605-6900
E-mail info@ntis.gov
Website <http://www.ntis.gov/help/ordermethods.aspx>

Reports are available to DOE employees, DOE contractors, Energy Technology Data Exchange representatives, and International Nuclear Information System representatives from the following source:

Office of Scientific and Technical Information
PO Box 62
Oak Ridge, TN 37831
Telephone 865-576-8401
Fax 865-576-5728
E-mail reports@osti.gov
Website <http://www.osti.gov/contact.html>

This report was prepared as an account of work sponsored by an agency of the United States government. Neither the United States government nor any agency thereof, nor any of their employees, makes any warranty, express or implied, or assumes any legal liability or responsibility for the accuracy, completeness, or usefulness of any information, apparatus, product, or process disclosed, or represents that its use would not infringe privately owned rights. Reference herein to any specific commercial product, process, or service by trade name, trademark, manufacturer, or otherwise, does not necessarily constitute or imply its endorsement, recommendation, or favoring by the United States government or any agency thereof. The views and opinions of authors expressed herein do not necessarily state or reflect those of the United States government or any agency thereof.

Use of Plant Names

In this report the names of nuclear power plants that are currently operating in the United States are sometimes used. This investigation has used information from operating plants to develop representative models. However, these models and the associated analysis results that are reported herein do not replace, supersede, or contradict analyses and information that supports the licensing basis of the named plants.

The Effect of Shallow Inside-Surface-Breaking Flaws on the Probability of Brittle Fracture of Reactors Subjected to Postulated and Actual Operational Cool-Down Transients: A Status Report

Manuscript Completed: January 2016

Date Published: February 2016

Prepared by

**B. Richard Bass, Terry L. Dickson, Paul T. Williams, Hilda B. Klasky,
and Robert H. Dodds, Jr.**

Oak Ridge National Laboratory
Managed by UT-Battelle, LLC
Oak Ridge National Laboratory
Oak Ridge, TN 37831-6085

Prepared for
Division of Engineering
Office of Nuclear Regulatory Research
U.S. Nuclear Regulatory Commission
Washington, DC 20555-0001
NRC Job Code N6438

This page is intentionally left blank.

**The Effect of Shallow Inside-Surface-Breaking Flaws on the Probability of Brittle Fracture of Reactors Subjected to Postulated and Actual Operational Cool-Down Transients:
A Status Report**

B. R. Bass, T. L. Dickson, P. T. Williams, H. B. Klasky, and R. H. Dodds Jr.

ABSTRACT

Note: The work documented herein is part of an on-going effort that is sponsored by the NRC at ORNL and does not describe a final product or a regulatory position. This effort aims to better understand and quantify the risk of crack initiation and reactor vessel fracture posed by normal operating loads (that is: heat up, cool down, and leak tests). These results have been generated using the best models and technical understanding available at this time consistent with the funded scope and timeframes of the project. Nevertheless, readers should recognize that certain aspects of the models that have been implemented in the PFM computer code FAVOR used to produce the results reported herein remain the topic of continued study and refinement. These concern mostly the model of the RPV cladding and flaws that may lie in or near the cladding; see Chapter 5 for details. Future improvements to these models may alter the results presented herein. Such changes, if they occur, will be communicated by (a) revisions of this report, and (b) the issuance of other related reports.

Reactor pressure vessel (RPV) geometries subjected to postulated transients that follow normal cool-down limit curves were analyzed using the probabilistic fracture mechanics (PFM) code FAVOR. The objective of this investigation was to determine trends for conditional probability of crack initiation (*CPI*) and of vessel failure (*CPF*) as a function of inner diameter (ID) surface-breaking flaw depth. The analyses showed that shallow, circumferential, ID surface-breaking flaws dominate the RPV failure probability, and exhibit *CPI* and *CPF* values that exceed those for the $\frac{1}{4} t$ flaw referenced in the ASME Code, Section XI, Appendix G. Those results were observed not only for a majority of cases where cool-down transients were defined using the ASME code procedure for establishing pressure-temperature (P-T) limits for normal cool-downs as specified by Section XI of the ASME Code, but also using the EPRI-MRP-250 risk-informed methodology, which was incorporated into the 2011 Addenda of the ASME Code [American Society of Mechanical Engineers (ASME) Boiler & Pressure Vessel Code, Section XI, Rules for In-service Inspection of Nuclear Power Plant Components, Nonmandatory Appendix G, “Fracture Toughness Criteria for Protection Against Failure,” 2011 Addenda to the 2010 Edition].

These analyses demonstrated trends in *CPI* and *CPF* for ID surface-breaking flaws that vary non-monotonically with flaw depth, reaching a global maximum for very shallow flaws just penetrating through the stainless steel cladding and into the ferritic RPV steel wall. This outcome is caused by the additional crack driving force generated for shallow flaws due to the mismatch in coefficient of thermal expansion (*CTE*) between cladding and base material, which elevates the thermally-induced stresses. The *CTE* contribution diminishes rapidly as flaw depth increases.

To better understand these findings, further study was undertaken to evaluate the accuracy and adequacy of the ID surface-breaking flaw model implemented in the FAVOR computer code. A

literature survey was conducted to identify information concerning the physical attributes and the incidences of shallow flaws found in the stainless-steel cladding of RPVs. This assessment confirmed that the FAVOR model incorporates the features necessary for modeling observed shallow surface flaws subjected to service loading conditions; those features include adequate and accurate representations of vessel geometry/stress loading, and physical attributes and incidences of the observed flaws. Specifically, the FAVOR flaw model provides realistic simulation of vessel geometry and stress fields in the beltline region of a RPV, and uses flaw modeling characteristics and flaw input files derived from multiple sources that include destructive and non-destructive examinations of RPV materials, flaw simulation studies using the PRODIGAL code, and NRC expert elicitation results for vessel flaws.

Detailed analyses were conducted to assess the impact of various loading conditions on shallow ID surface-breaking flaws: normal cool-downs following the maximum allowable pressure curve (including ASME code procedure and EPRI-MRP-250 risk-informed approach), normal cool-downs following operating nuclear power plant (NPP) pressure and temperature (P-T) curves, and postulated accident cool-downs (i.e., pressurized-thermal-shock events). Results for P-T transients that follow operating NPP pressure curves are shown to be consistent with many cool-down transients that follow the maximum allowed pressure (for both ASME code and EPRI risk-informed), i.e., shallow surface-breaking flaws have the highest probability of brittle fracture. For PTS transients that exhibit a sustained cool-down versus time to relatively lower temperatures, fracture probability for shallow surface-breaking flaws was higher than for embedded flaws, consistent with the results for normal cool-downs. However, the majority of PTS transients do not exhibit such sustained cool-down, with the result that embedded flaws, rather than surface breaking flaws, are the risk drivers for the most rapid cool-down loadings.

It is shown herein that a shallow surface flaw just penetrating the cladding exhibits a *CPI* value exceeding the ASME/Appendix G $\frac{1}{4} t$ flaw value by several orders of magnitude. While the probability is extremely low that $\frac{1}{4} t$ flaws exist in service, it can be argued that use of the $\frac{1}{4} t$ flaw has been regarded as a conservatism that compensates for omissions/uncertainties in the calculation of P-T limits. One factor omitted in the ASME methodology is the existence of cladding on the inner surface of the RPV. The principal result of this report makes clear that the enhanced size of the $\frac{1}{4} t$ flaw does not compensate for ignoring the added driving force to fracture produced by the layer of cladding that acts on the shallow surface flaw.

Finally, several specific issues concerning the FAVOR flaw methodology have been identified by stakeholders external to ORNL as warranting further study to determine whether refinement of those features of the model could have a material effect on the major conclusions of this report. The primary issues are briefly summarized herein for consideration by the NRC as future research topics.

This page is intentionally left blank.

CONTENTS

	Page
ABSTRACT	v
LIST OF TABLES.....	x
LIST OF FIGURES.....	xi
ACRONYMS	xv
ACKNOWLEDGMENTS.....	xvii
1. Introduction	1
1.1 Background and Motivation	1
1.2 Example of the Observed Effect of Surface-Breaking Flaw Depth on RPV Failure Probability	1
1.3 Influence of the Base/Clad Bi-material Interface.....	8
1.4 Deep-flaw versus Shallow-Flaw Behavior.....	11
1.5 Objectives	12
1.6 Scope	12
2. Adequacy and Accuracy of the FAVOR Surface-Breaking Flaw Model	15
2.1 Shallow Flaws in Stainless-Steel Cladding: Flaws Found in RPV Cladding Compared to the FAVOR Model	15
2.1.1 Description of the Flaws Found in RPV Cladding.....	15
2.1.2 Description of the FAVOR Inner Surface-Breaking Flaw Model.....	22
2.1.3 Assessment of the FAVOR Model applied to Shallow Flaws in Cladding.....	31
2.2 Finite Element Assessment: FAVOR Compared to ABAQUS.....	31
2.2.1 Three-Dimensional Model Analyses.....	34
2.3 Advanced Fracture Mechanics Considerations: Loss of Constraint (T-stress)	37
2.4 Conclusions Regarding Adequacy/Accuracy of the FAVOR Surface-Breaking Flaw Model	39
3. Assessment of Shallow Flaws for Different Loading Conditions	43
3.1 Normal Cool-downs That Follow Actual Plant Pressure and Temperature Records.....	45
3.2 Postulated Accident Cool-downs (PTS Events)	45
3.3 Summary	50
4. Summary and Conclusions	53
5. Potential Future Research	56
6. References	58
APPENDIX A: PROCEDURE FOR COMPUTATION OF CONDITIONAL PROBABILITY OF INITIATION FOR SURFACE FLAWS SUBJECTED TO POSTULATED COOL-DOWN TRANSIENTS.....	61
APPENDIX B: 2-D AXISYMMETRIC MODEL ANALYSES	70

APPENDIX C: SENSITIVITY STUDIES FOR OCCURRENCE OF LATE-PEAKING OF MAXIMUM APPLIED K_I	78
APPENDIX D: SOME RELEVANT EXPERIMENTAL STUDIES OF RPV CLADDING	94
APPENDIX E: KEY ASPECTS OF THE CLAD/BASE MODEL IN FAVOR	98

LIST OF TABLES

Table	Page
2-1 Assessment of the FAVOR Model Applied to Shallow Flaws Observed in Stainless Steel Cladding of RPVs (a) Shallow Flaws	32
2-1 Assessment of the FAVOR Model Applied to Shallow Flaws Observed in Stainless Steel Cladding of RPVs (b) Cladding/Base Metal	33
2-2 Geometry Parameters of the Flawed RPV Models	35
3- 1 Comparison of Conditional Probabilities of Initiation (<i>CPI</i>) for Shallow Surface and Embedded Flaws when Subjected to Two Groups of PTS Transients.....	52
A-1 Distribution of surface flaw aspect ratios used in analyses	62
A-2 Flaw number 1: $a/t = 0.03t$ flaw, aspect ratio of 6:1, located in weld material,	68
A-3 Flaw number 2: $a/t = 0.03t$ flaw, aspect ratio of 6:1, located in plate material,	68
A-4 Allocation of <i>CPI</i> to region and aspect ratio for model that includes through-wall weld residual stress	69
A-5 Results of PFM analyses with and without inclusion of through-wall weld residual stress.....	69
C-1 Tabulation of various K_I parameters computed for range of normalized flaw depths at time $t = 554\text{min}$ of P-T versus time limit curves used for analyses of Fig. C-1.	79
C-2 RPV / flaw geometry for three plants used in sensitivity study	83
C-3 Summary sensitivity study on the joint influence of the three parameters [RPV geometry, embrittlement (i.e., EFPY), and cool down rate] on whether the 1 st peak or the 2 nd peak in the total applied K_I is higher.....	86
C-4: Nomenclature for Tables C-5, C-6, and C-7	89
C-5 Results generated in sensitivity study for Plant A assuming a circumferential, inner surface-breaking flaw with depth $a = 0.03t$ and 6:1 aspect ratio (including weld residual stress).....	90
C-6 Results generated in sensitivity study for Plant B assuming a circumferential, inner surface-breaking flaw with depth $a = 0.03t$ and 6:1 aspect ratio (including weld residual stress).....	91
C-7 Results generated in sensitivity study for Plant C assuming a circumferential, inner surface-breaking flaw with depth $a = 0.02t$ and 6:1 aspect ratio (including weld residual stress).....	92
E-1 Strains* Measured when Cladding was Released from the Base Material of a RPV Shell Segment	103
E-2 Stress Components Computed from Strains Measured in Cladding taken from a RPV Shell Segment; stresses are calculated at room temperature (70 °F)	103

LIST OF FIGURES

Figure	Page
1-1 Prescribed pressure-temperature limits for normal cool-down transients determined using standard ASME code procedures. Results are shown for <i>Vessel A</i> at 60 EFPY with a cool-down rate of 50 °F/hr.....	3
1-2 Schematic of three inner-surface breaking flaws of interest with varying depth and constant aspect ratio of flaw length to depth (figure not to scale).....	4
1-3 <i>CPI</i> for circumferentially-oriented, inner-surface flaws exhibiting non-monotonic behavior with flaw depth for <i>Vessel A</i> subject to the pressure and temperature limits determined from the standard ASME code procedure and shown in Fig. 1-1; the latter is based on 60 EFPY and cool-down rate of 50 °F/hr.	5
1-4 Illustration of the possible variations of applied $K_I (=K_{APPLIED})$ with time during a cool-down.	6
1-5 K_I versus time profiles partitioned to show the effect of the thermal stresses imparted by the cladding during the thermal transient for <i>Vessel A</i> at 60 EFPY at 50 °F/hr.....	7
1-6 K_I versus time curves for Flaw 1a ($a/t = 0.03$ with base material properties) and Flaw 1 ($a/t = 0.03$ with bi-material properties) subjected to postulated cool-down transient derived from the ASME code procedure and shown in Fig. 1-1.....	10
1-7 K_I versus time curves for shallow flaw ($a/t = 0.03$) and for deep flaw ($a/t = 0.25$) subjected to postulated cool-down transient derived from the ASME code procedure (see Fig. 1-1); applied K_I are compared with fracture toughness curves from FAVOR and from ASME code.	12
2-1 Optical micrograph of cracks extending through cladding into base metal (extracted from ref. [11]).	18
2-2 Corrosion of base metal at the end of clad crack (extracted from ref. [11]) showing the defect extending as “ditches” in the base metal along the tip of the crack.	19
2-3 Surface-breaking crack found in JPDR (extracted from ref. [11]), showing a complex topography of the interface in the base metal resulting from a “pitting-type corrosion” in the narrow crevice.	20
2-4 Examples of flaws in cladding of PVRUF vessel (extracted from ref. [12]).....	21
2-5 FAVOR model realistically simulates the geometry and stress fields experienced in RPV beltline subjected to thermal-hydraulic transients.	23
2-6 Comparison of FAVOR 1-D and ABAQUS 3-D model predictions: (a) axial stress and (b) hoop stress analysis for a RPV subjected to a thermal-hydraulic transient.....	24
2-7 Transient heat conduction and thermo-elastic stress analyses performed using one-dimensional axisymmetric finite element model of un-cracked RPV wall.	25
2-8 Circumferential surface-breaking flaws postulated in FAVOR [1] (not to scale) showing four aspect ratios (length/depth): 2:1, 6:1, 10:1 and uniform depth (infinite)	29
2-9 Cladding model implemented in FAVOR.....	30
2-10. Finite-element model for PWR with an ID circumferential surface flaw ($a/t = 0.05$)...	35
2-11 Comparison of K_I versus time curves for shallow flaw $a/t = 0.03$. <i>Vessel A</i> subjected to P-T limits determined from EPRI risk-informed method based on 60 EFPY and cool-down rate of 50 °F/hr.....	36

2-12 Comparison of K_I versus time curves for shallow flaw $a/t = 0.05$. Vessel A subjected to P-T limits determined from EPRI risk-informed method based on 60 EFPY and cool-down rate of 50 °F/hr.....	36
2-13 Comparison of LEFM and EPFM K_I versus time curves for shallow flaw $a/t = 0.03$. Vessel A subjected to P-T limits determined from EPRI risk-informed method based on 60 EFPY and cool-down rate of 50 °F/hr.....	37
2-14 Schematic view of crack-tip stress fields.....	38
2-15 (a) T -stress history for Flaw 1 $a/t = 0.03$; (b) Comparison of LEFM and EPFM K_I versus time curves for Flaw 1 $a/t = 0.03$. Vessel A subjected to P-T limits determined from EPRI risk-informed method based on 60 EFPY and cool-down rate of 50 °F/hr. .	40
3-1 CPI values for Vessel A after 60 EFPY for cool-downs at 100 °F/hour along the maximum-allowable pressure curves calculated using both ASME code procedure and EPRI risk-informed alternative P-T limit equations	44
3-2 Illustration of pressure (P) and temperature (T) versus time curves for four actual cool-down transients, identified herein as RT-1, RT-2, RT-3 and RT-4.....	46
3-3 Comparison of CPI values versus normalized crack depth for four actual transients with those computed for the maximum-allowable pressure transient (ASME code procedure) applied to Vessel A at 60 EFPY and 100 °F /hr cool-down rate. Values plotted at 10^{-10} represent $CPI=0$	47
3-4 Comparison of CPF values versus normalized crack depth for four actual transients with those computed for the maximum-allowable pressure transient (ASME code procedure) applied to Vessel A at 60 EFPY and 100 °F /hr cool-down rate.....	48
3-5 Two groups of PTS cool-down transients that exhibit different characteristics regarding cool-down rates: (a) Group I - transients have a relatively steady initial cool-down rate that is sustained over a period of time; (b) Group II - transients that have very fast cool-down rates over a short period of time.	51
3-6 Plot of the data from Table 3- 1 illustrating the effect of cooling rate on the population of flaws that dominate the PFM results	52
A-1 CPI for circumferentially-oriented inner surface flaws exhibiting non-monotonic behavior with flaw depth for Vessel A subject to the pressure and temperature limits determined from ASME code procedure and shown in Fig. A-2; the P-T limits are based on 60 EFPY and a cool-down rate of 50 °F/hr.....	61
A-2 Prescribed pressure-temperature limits for normal cool-down transients determined using standard ASME code procedure. Pressure-temperature limits are shown for Vessel A at 60 EFPY with a cool-down rate of 50 °F/hr.	62
A-3 Example of the distribution of RT_{NDT} at crack tip of shallow flaw in PFM analyses	64
A-4 Results of PFM analyses with and without inclusion of through-wall weld residual stress	67
A-5 Interaction of K_I versus time for shallow flaws of different aspect ratios with $K_{IcWeibull-a}$ versus time for crack tip $RT_{NDT} = 338.35$ °F	67
B-1 Pressure-temperature limits for normal cool-down transients determined using (1) standard ASME code procedures and (2) the recently proposed EPRI-MRP-250 risk-informed procedures. Results are shown for Vessel A at 60 EFPY for cool-down rate of 50 °F/hr.	70
B-2 2-D axisymmetric finite element model with 360° shallow circumferential surface flaw ($a/t=0.03$).	72

B-3 Comparison of FAVOR and ABAQUS finite-element (linear elastic) results of axial through-wall stresses for uncracked RPV. <i>Vessel A</i> geometry at 60 EFY subjected to the EPRI-MRP-250 risk-informed derived pressure limits [B3], with a 50 °F/hr cool-down transient.....	73
B-4 Deformed FE Models with different shallow flaw depths subjected to thermal loading. (100x amplification factor used for visualization of deformation). <i>Vessel A</i> geometry subjected to thermal-only loading from a 50 °F/hr cool-down transient.	74
B-5 Crack opening displacement (COD) for shallow flaws with different flaw depths subjected to thermal-only loading.	75
B-6 Comparison of K_I time history for the 2-D axisymmetric models ($a/t = 0.03$ and 0.05) subjected to 50° F/hr cool-down thermal-only transient.	75
B-7 von Mises stress at the crack-tip for the 2-D axisymmetric model ($a/t = 0.03$) at time of 554 minutes.....	76
C-1 $K_{I,clad}$ versus transient time for values of normalized flaw depth (a/t) ranging from 0.03 to 0.25; P-T limits for postulated normal cool-down transient determined using ASME code procedures; <i>Vessel A</i> at 60 EFY with a cool-down rate of 50 °F/hr.	78
C-2 FAVOR analyses for different values of clad stress-free temperature exhibit same trends of maximum K_I occurring at second peak late in transient; results shown for a = 0.03t flaw depth. Loading/vessel parameters are the same as those used for analyses depicted in Fig. C-1.	79
C-3 Minor variations in stress free temperature do not change the shallow flaw behavior ..	80
C-4 Illustration of three different pressure transients – each with distinct value of $\Delta t_{initial}$ – the time at which pressure is reduced below steady state pressure. The thermal transient is same for all three transients.....	81
C-5 – Illustration that the magnitude of the 1 st peak of K_I corresponds to $\Delta t_{initial}$; therefore, the smaller $\Delta t_{initial}$, the greater the likelihood that the magnitude of K_I at the 2 nd peak will exceed the magnitude of K_I at the 1 st peak.	82
C-6 Illustration of the possible variations of applied K_I ($=K_{APPLIED}$) with time during a postulated cool-down.	85
C-7 For P-T curves derived from the EPRI risk-informed method and cool-down rate of 50 °F/hr, the maximum K_I for shallow internal surface breaking flaw occurred at the 2nd peak late in the postulated transient for 35 out of 36 cases examined; three cases are shown here for illustration.	87
C-8 For P-T curves derived from the ASME code procedure and cool-down rate of 50 °F/hr., the maximum K_I for shallow internal surface-breaking flaw occurred at the 2 nd peak, late in the postulated transient for 20 out of 36 cases examined; three cases are shown here for illustration.	88
D-1 Stretch zone and UT indications for flaw #3 extension by cleavage propagation beneath clad layer in TSE-8 (Fig. 8 in Ref. D1).	96
D-2 Stretch zone in cladding above extended flaw #3; center of stretch zone marked with pen; note bifurcation of flaw in foreground (Fig. 9 in Ref. D1).	97
E-1 Cladding model implemented in FAVOR.	99
E-2 Stress-free temperature was determined through combined experimental measurements and finite element analysis.	101

E-3 Inspection targets applied to clad inner surface prior to machining away the base material.	102
E-4 Through-wall profile of residual stresses and K_I used in the FAVOR code.	105

ACRONYMS

ASME	American Society of Mechanical Engineers
BWR	boiling water reactor
COD	crack opening displacement
CP	ASME standard code procedure (2010) in determination of maximum allowable pressure
<i>CPF</i>	conditional probability of vessel failure. The probability is termed <i>conditional</i> because it assumes that the analyzed transient has occurred. To transform <i>CPF</i> into a risk metric it must be multiplied by the probability of the transient occurring. An extensive discussion of the protocols used to calculate <i>CPF</i> in FAVOR can be found in ref. [1] and in Appendix A to this report.
<i>CPI</i>	conditional probability of crack initiation. The probability is termed <i>conditional</i> because it assumes that the analyzed transient has occurred. To transform <i>CPI</i> into a risk metric it must be multiplied by the probability of the transient occurring. An extensive discussion of the protocols used to calculate <i>CPI</i> in FAVOR can be found in ref. [1] and in Appendix A to this report.
<i>CTE</i>	coefficient of thermal expansion
EFPY	effective full-power years
EPFM	elastic-plastic fracture mechanics
EPRI	Electric Power Research Institute
FAVOR	Fracture Analysis of Vessels – Oak Ridge
FEM	finite-element method
ID	inner diameter
IGSCC	inter-granular stress corrosion cracking
JPDR	Japan Power Demonstration Reactor
LEFM	linear-elastic fracture mechanics
NPP	nuclear power plants
NRC	United States Nuclear Regulatory Commission
NRO	New Reactor Office - NRC
NRR	Nuclear Reactor Regulation - NRC
ORNL	Oak Ridge National Laboratory
PFM	Probabilistic Fracture Mechanics
PNNL	Pacific Northwest National Laboratory
ProSaMM	Probabilistic Structural and Material Modeling Program
PTS	pressurized thermal shock
PVRUF	Pressure Vessel Research Users Facility
PWR	pressurized water reactor
RES	Nuclear Regulatory Research - NRC
RI	EPRI risked-informed method for determination of maximum allowable pressure
RPV	reactor pressure vessel
SIFIC	stress-intensity factor influence coefficients

TWCF through-wall cracking frequency; which is calculated as a product of the *CPF* and a matrix defining the sequence (or event) frequency of the loading transients (see FAVOR theory manual [1] for additional details). Calculating a mean *TWCF* for RPVs subjected to pressure and temperature curves (regardless of their origin) requires a statistical representation of the possible transients and their frequencies of occurrence. Compilation of such frequency data for normal operational startup and shutdown transients was not within the work scope of this study; thus, no values of *TWCF* are reported herein.

WRS weld residual stress

ACKNOWLEDGMENTS

Completion of the revised version (REV-01) of this report is the result of extensive collaborations between ORNL and staff at the NRC. Foremost in that group is the NRC/RES technical manager for the ORNL RPV programs, Dr. Mark T. Kirk, who provided critical leadership in defining the objectives of the report and in presenting the content with clarity. Also, the authors want to acknowledge the many helpful comments and recommendations on the draft report provided by staff within NRC/NRR and NRC/NRO; due consideration was given to all of their input in preparation of this revised report. Finally, the authors acknowledge the helpful discourse, comments and recommendations provided by Dr. Randy K Nanstad in the Materials Science and Technology Division of ORNL.

1. Introduction

1.1 Background and Motivation

Oak Ridge National Laboratory (ORNL) analyzed a range of reactor pressure vessel (RPV) geometries subjected to postulated transients that follow normal cool-down limit curves¹ using the probabilistic fracture mechanics (PFM) code called FAVOR, which stands for **F**racture **A**nalysis of **V**essels, **O**ak **R**idge [1]. The objective of those studies was to determine trends for conditional probability of initiation (*CPI*) and the conditional probability of vessel failure (*CPF*) as a function of initial flaw depth for postulated circumferential, surface-breaking flaws on the inner surface of the RPV. Those cool-down transients were developed using standard Code procedures that define pressure-temperature (P-T) limits as specified by the American Society of Mechanical Engineers (ASME) Boiler and Pressure Vessel Code, Section XI, Nonmandatory Appendix G (ASME Sect. XI App. G) [2]. These analyses produced two results:

Result 1. Very shallow surface-breaking flaws² dominate the RPV failure probability. This result was unanticipated because, in previous analyses of pressurized thermal shock (PTS) transients [3], shallow surface-breaking flaws were observed to be small contributors to the total estimated probability of vessel failure.

Result 2. Very shallow surface-breaking flaws exhibit *CPI* and *CPF* values that exceed by orders of magnitude those for the $\frac{1}{4} t$ flaw referenced in the ASME Code, Section XI, Appendix G. This result was unanticipated because the much deeper flaw is expected to pose a greater risk to the integrity of the vessel when evaluated in terms of the *CPI/CPF* metrics.

This report provides a quantitative assessment of shallow, ID, through-clad flaws in a RPV, performed with the FAVOR code; those analyses were undertaken in an attempt to both rationalize and understand the unanticipated results.

1.2 Example of the Observed Effect of Surface-Breaking Flaw Depth on RPV Failure Probability

Fig. 1-1 depicts the P-T versus time limit curves computed according to the ASME code procedure [2] for a pressurized water reactor RPV (designated herein as *Vessel A*³) at 60

¹ In this study, the term “cool-down transient” refers generally to a postulated cool-down transient that follows pressure-temperature limit curves generated using the ASME Boiler & Pressure Vessel Code Section XI Appendix G [2]. Exceptions to the latter are specifically noted in the report.

² Herein, shallow surface breaking flaws are assumed to exist in the cladding, without consideration of the cladding process. The effect of the number of cladding layers on the incidence of these flaws is described in detail in [12, 14 and 15] and is summarized briefly in Section 2.1.2 of this report.

³ Throughout this report, analyses are performed for a nuclear RPV referred to as “Vessel A.” The input parameters defining Vessel A, including vessel geometry, material properties, embrittlement, and loading conditions, are provided in Appendix B of the report.

effective-full-power-years (EFPY) at a cool-down rate of 50 °F/hr. The temperature versus time curve is an input to the analysis; the pressure versus time curve is then determined through the ASME code procedures given in [2]. These P-T versus time curves were used as input to PFM analyses performed with the FAVOR code to determine the mean *CPI* as a function of normalized flaw depth for circumferentially-oriented, inner-surface flaws. Three flaws shown in Fig. 1-2 (Flaw 1: $a/t = 0.03$, Flaw 2: $a/t = 0.05$, Flaw 3: $a/t = 0.25$) are of particular interest in the latter analyses. Throughout this report, the normalized flaw depth, a/t , is defined as the initial flaw depth, a , normalized by the vessel's total (cladding plus base) wall thickness, t .

As shown in Fig. 1-3, the predicted mean *CPI* trends from FAVOR for these flaws vary non-monotonically with initial flaw depth. The initial flaw depth corresponds to the depth of the assumed pre-existing, surface-breaking, semi-elliptic flaw before the initiation of any subsequent flaw growth that could occur due to thermal-mechanical loading. More specifically, the mean *CPI* exhibits a global minimum for very shallow flaws over an interval of normalized flaw depths from 0.03 to 0.06 and a global maximum as the flaw depth approaches the clad/base interface. The mean *CPI* for Flaw 1 with $a/t = 0.03$ in Fig. 1-3, subjected to the postulated cool-down transient of Fig. 1-1, is estimated to be 3.57×10^{-5} , compared to the global minimum mean *CPI* value of 6.58×10^{-11} observed for the slightly deeper Flaw 2 at $a/t = 0.05$. The *CPI* value for the shallowest flaw (Flaw 1) shown in Fig. 1-3 significantly exceeds that computed for the ASME $\frac{1}{4} t$ flaw, designated as Flaw 3. A detailed description of the procedure used to perform the calculations for a given flaw depth referenced in Fig. 1-3 is provided in Appendix A of this report.

The results illustrated in Fig. 1-3 are for the ASME code procedure of deriving the P-T curves (shown in Fig. 1-1) assuming that the cool-down follows the P-T limits allowed by the ASME Code. Many additional analyses [4] were performed over a range of vessel geometries, levels of embrittlement, and cool-down rates, using different methods of deriving the P-T curves, such as the industry-proposed EPRI-MRP-250 method [5] (herein referred to as the EPRI risk-informed method). The great majority of those analyses produced results similar to Fig. 1-3, i.e., a global maximum of *CPI* at very shallow, through-clad flaws just penetrating into the base material.

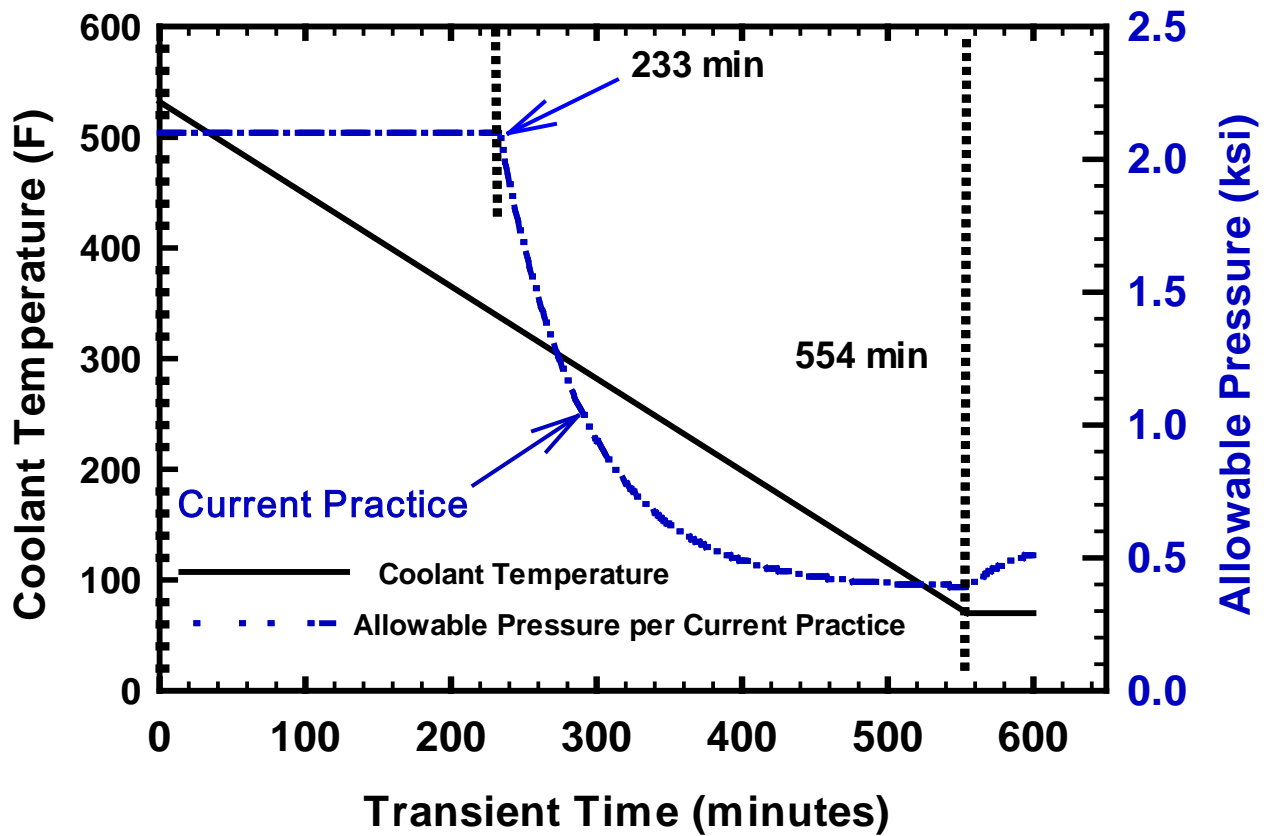


Fig. 1-1 Prescribed pressure-temperature limits for normal cool-down transients determined using standard ASME code procedures. Results are shown for *Vessel A* at 60 EFPY with a cool-down rate of 50 °F/hr.

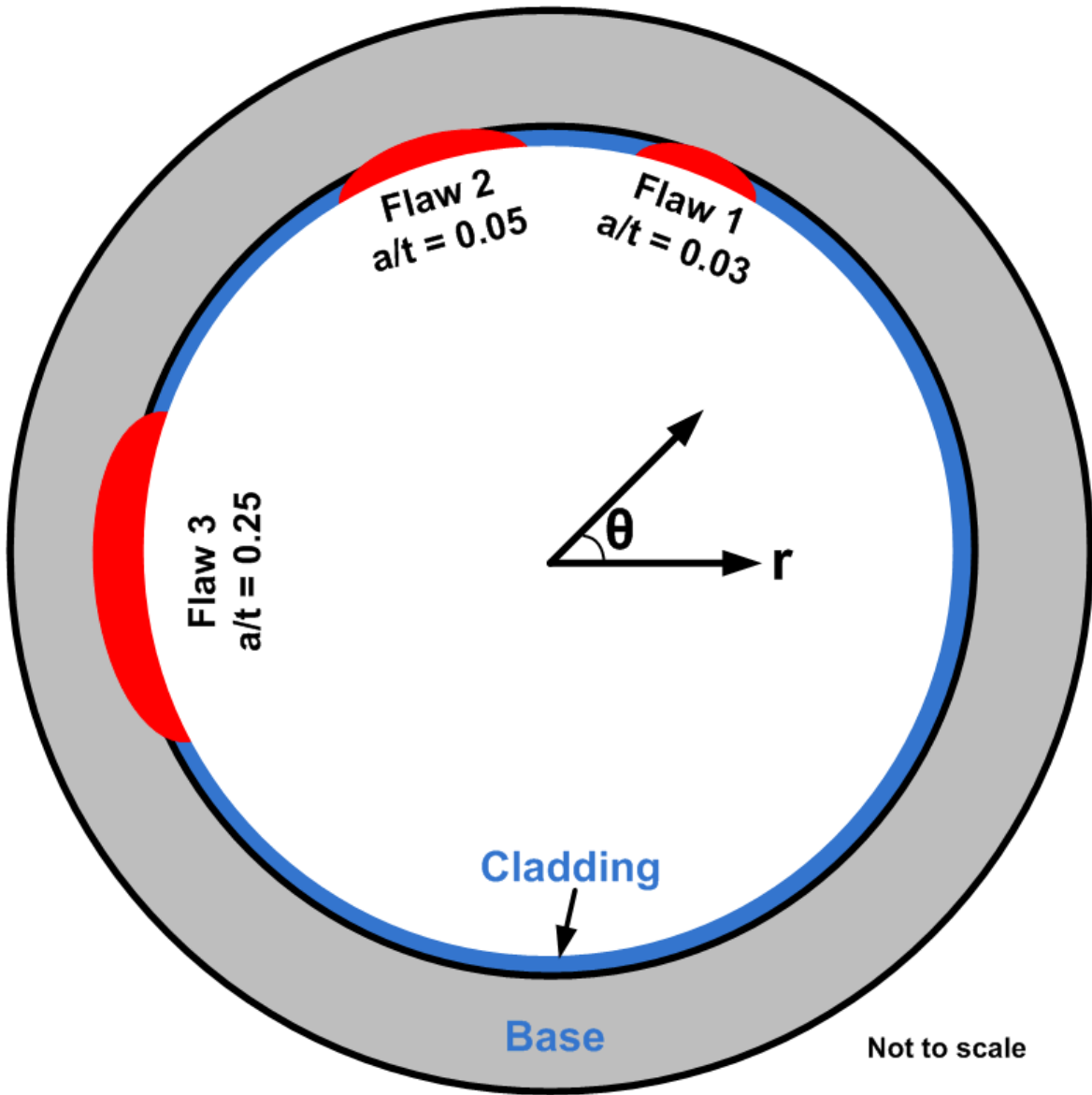


Fig. 1-2 Schematic of three inner-surface breaking flaws of interest with varying depth and constant aspect ratio of flaw length to depth (figure not to scale).

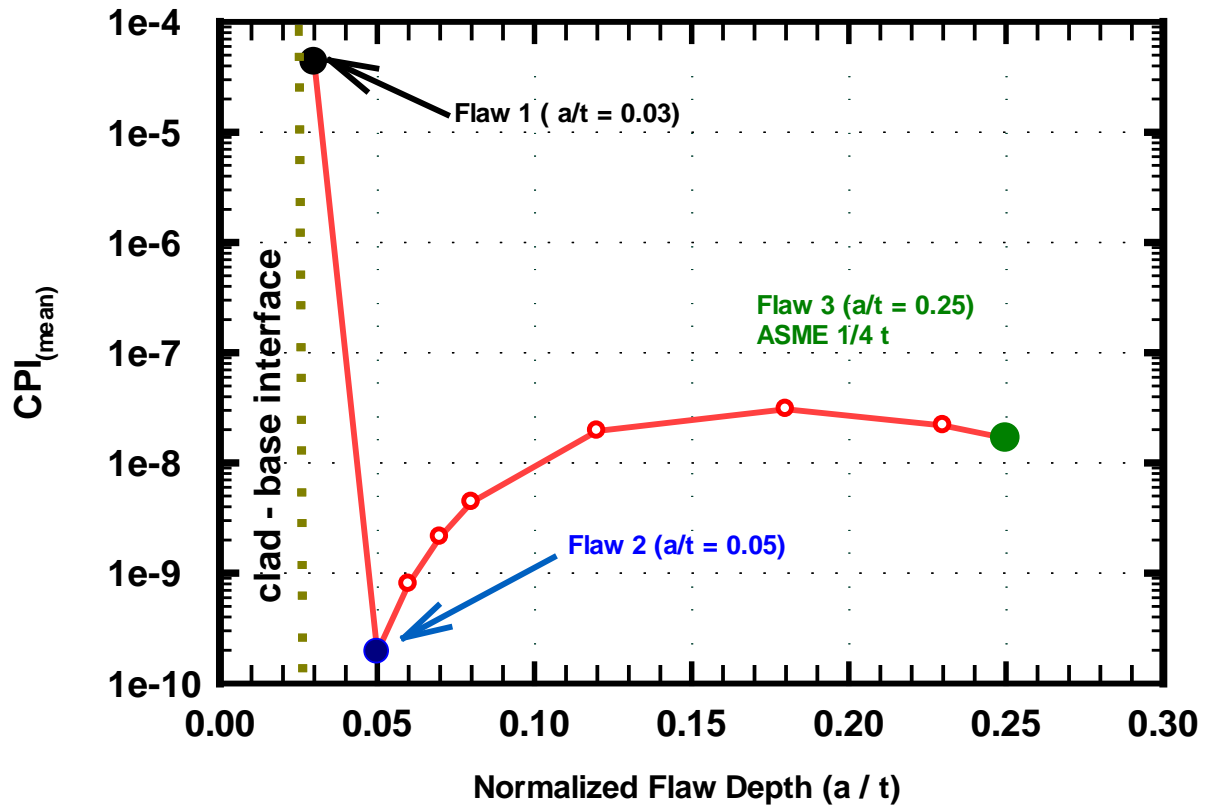


Fig. 1-3 *CPI* for circumferentially-oriented, inner-surface flaws⁴ exhibiting non-monotonic behavior with flaw depth for Vessel A subject to the pressure and temperature limits determined from the standard ASME code procedure and shown in Fig. 1-1; the latter is based on 60 EFPY and cool-down rate of 50 °F/hr.

The results illustrated in Fig. 1-3 can be understood with reference to Fig. 1-4. Beginning at the top of the figure, a cooling rate is selected, which is used together with either the standard ASME code procedure [2] or the EPRI-MRP-250 risk-informed [5] method to determine a variation of maximum allowable pressure with time. The resulting variation of temperature and pressure with time is input to FAVOR, which estimates the variation of the LEFM driving force (applied K_I) and material fracture toughness (K_{Ic}) with time for specified values of flaw depth and RT_{NDT} . The variation of applied K_I with time exhibits two local maxima. The first peak occurs at the end of the initial constant pressure hold, and results from the subsequent reduction of the pressure contribution to applied K_I . However, even though pressure stresses are reduced after this initial

⁴ For every flaw depth shown in this figure a surface flaw density of 3.7×10^{-3} flaws per square foot of clad area on the vessel ID was used. This density was recommended by PNNL as being appropriate for the shallowest flaws (0.03t in this figure, see [12] for details). This density is assumed herein to apply to surface breaking flaws of all depths.

peak, thermal stresses continue to increase until the end of the cool-down, after which time thermal stresses are reduced, producing a second peak.

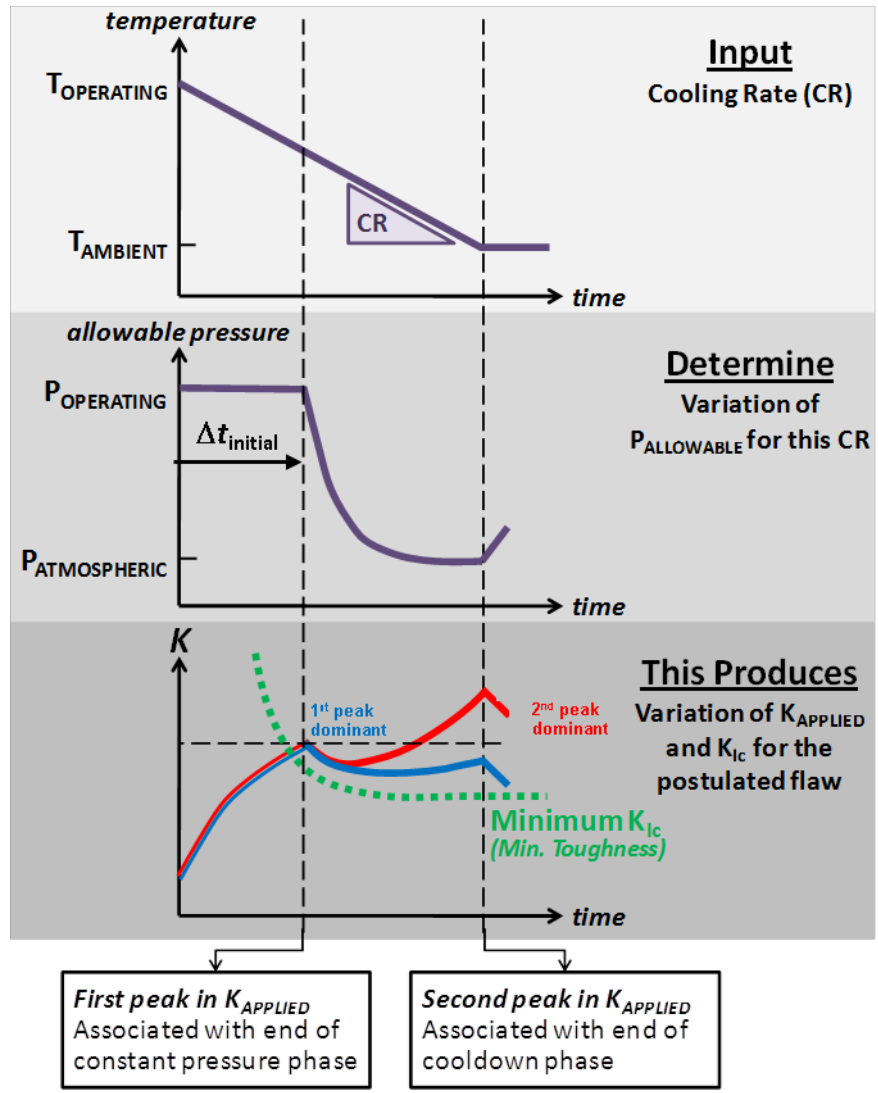


Fig. 1-4 Illustration of the possible variations of applied $K_I (=K_{APPLIED})$ with time during a cool-down.

The non-monotonic variation of CPI with flaw depth (illustrated in Fig. 1-3) occurs because, depending upon the conditions being modeled, either the first or the second peak in applied K_I may control the value of CPI ⁵, as follows:

⁵ For purposes of illustration, Fig. 1-4 shows that the value of the applied K_I at both the first and second peaks exceeds the minimum fracture toughness, $K_{Ic(min)}$, which can lead to a non-zero CPI value. If the material's $K_{Ic(min)}$ exceeds the applied K_I , then the CPI is zero, and the temporal variation of the applied K_I is not important.

- 1st Peak Dominant (first peak controls CPI): This case will occur if the magnitude of applied K_I at the second peak remains below the value of applied K_I at the first peak. The CPI of the first peak will dominate even though the value of applied K_I at the second peak may, and often does, exceed the minimum of the fracture toughness distribution adopted by FAVOR.
- 2nd Peak Dominant (second peak controls CPI): This case will occur if the magnitude of the applied K_I at the second peak exceeds the value of the applied K_I at the first peak.

When the conditions being modeled lead to a 2nd Peak Dominant variation of applied K_I , the values of CPI are much higher than for 1st Peak Dominant conditions, even if the value of applied K_I at the two peaks differs by only a small amount. This increase in CPI occurs because the value of CPI scales roughly with the ratio of applied K_I to the minimum fracture toughness, $K_{Ic(\min)}$. This ratio is always larger for 2nd Peak Dominant variation because the temperature (and, therefore, the toughness) is lower at the end of the cool-down than it is earlier in the transient.

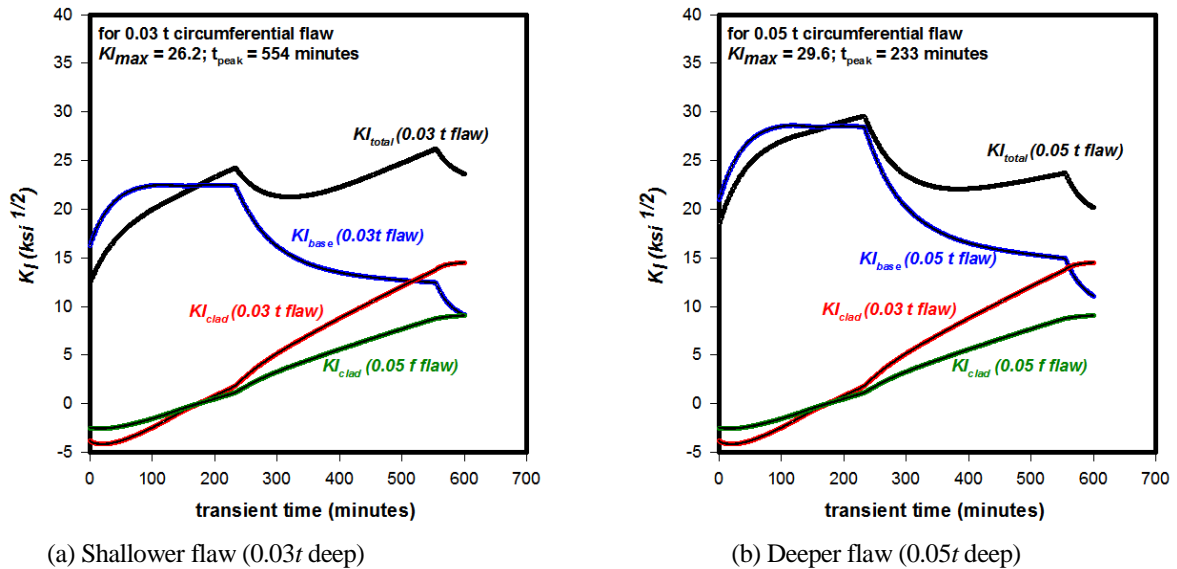


Fig. 1-5 K_I versus time profiles partitioned to show the effect of the thermal stresses imparted by the cladding during the thermal transient for Vessel A at 60 EFY at 50 °F/hr.

For both the ASME code procedure [2] and the EPRI-MRP-250 risk-informed [5] method, shallower flaws are more likely to exhibit 2nd Peak Dominant behavior than deeper flaws because of the additional fracture driving force generated by the mismatch in the coefficient of thermal expansion (CTE) between the stainless steel cladding and the underlying ferritic RPV base material. As illustrated in Fig. 1-5, the contribution of the cladding to the total K_I diminishes rapidly as the distance from the crack tip to the clad/base metal interface increases, such that a 0.03t flaw can exhibit 2nd Peak

Dominant behavior, while the deeper $0.05t$ flaw will exhibit *1st Peak Dominant* behavior⁶. Such a transition is responsible for the abrupt drop (orders of magnitude) in *CPI vs. a/t* shown by most of the FAVOR-generated results.

In Appendix C, sensitivity studies are described that examine the influence of various model parameters (including clad thickness, stress-free temperature, cool-down rate, etc.) on the occurrence of late-peaking for analyses of a normal cool-down transient.

1.3 Influence of the Base/Clad Bi-material Interface

In Fig. 1-3, the source of the abrupt change in the estimated mean *CPI* is due to the effects of differences in physical properties [primarily the coefficient of thermal expansion, *CTE*] of the stainless steel cladding and the underlying ferritic base metal on very shallow surface flaws just penetrating through the cladding into the base metal. To better understand this effect, it is instructive to consider the applied K_I versus time curves computed in the cool-down analysis for Flaw 1 with two different material models:

- bi-material model (different material properties are assigned to the cladding and the base metal)
- base metal-only model (in this case the cladding is assigned the properties of the base metal)

Analysis of Bi-material Model

Fig. 1-6 shows that the total applied K_I for Flaw 1 peaks first at 233 minutes into the cool-down transient derived from the ASME code procedure. In Fig. 1-6, the total applied K_I for Flaw 1 reaches the second peak at 554 minutes into the transient, which is higher than the first peak. The model for cleavage crack initiation used by FAVOR [1] states that a flaw initiates in brittle fracture only when the applied K_I satisfies two criteria:

- 1) applied K_I exceeds values experienced by the flaw for all previous times in the transient and
- 2) applied K_I exceeds the current temperature-dependent minimum fracture toughness, $K_{Ic(\min)}$.

⁶ In Appendix C, the contribution of the cladding to the total K_I is shown to diminish rapidly over the range of normalized flaw depths spanning the *a/t* range from 0.03 to 0.25.

This model reflects the well-accepted concept of “Warm Pre-Stress” [6]. As illustrated in Fig. 1-6, the CPI depends on the time history of the applied $K_{I_{max}}$ and $K_{Ic(min)}$ of the material⁷ in the transient:

- If $K_{I_{max}} > K_{Ic(min)}$, then $CPI > 0$;
- If $K_{I_{max}} < K_{Ic(min)}$, then $CPI = 0$.

For the very shallow Flaw 1, the applied $K_{I_{max}}$ occurs at 554 minutes [see Fig. 1-6], and its value is above the value of $K_{Ic(min)}$; therefore, $CPI > 0$, and a finite probability of crack initiation is predicted by FAVOR.

Analysis of Base Metal-Only Model

The analysis of Flaw 1 was repeated using the thermal and mechanical properties of the base metal to also represent the cladding (designated as Flaw 1a). The P-T versus time limit curves were unchanged. Fig. 1-6 compares the K_I values from the model with different base/clad properties (i.e., Flaw 1) and the model with base-only properties (i.e., Flaw 1a). For the base-material only model, Flaw 1a experiences a peak K_I value when the steady pressure begins to decrease (same as the first peak of the previous case with base/clad model). The K_I value decreases thereafter. *The higher “second peak” of K_I value never occurs in the model with only base-metal properties. This comparison demonstrates the significant role of mismatch in CTE properties of the clad and base metal on generating the high second-peak behavior for flaws of depth slightly greater than the cladding thickness.* The details of the FAVOR surface-breaking flaw model are discussed in Sect. 2 of this report.

⁷ The temperature-dependent material property, $K_{Ic(min)}$, is linked to the elapsed time of the transient through the time dependence of the crack-tip temperature.

**Bimaterial Material Properties Used for Flaw 1
Only Base Material Properties Used for Flaw 1a**

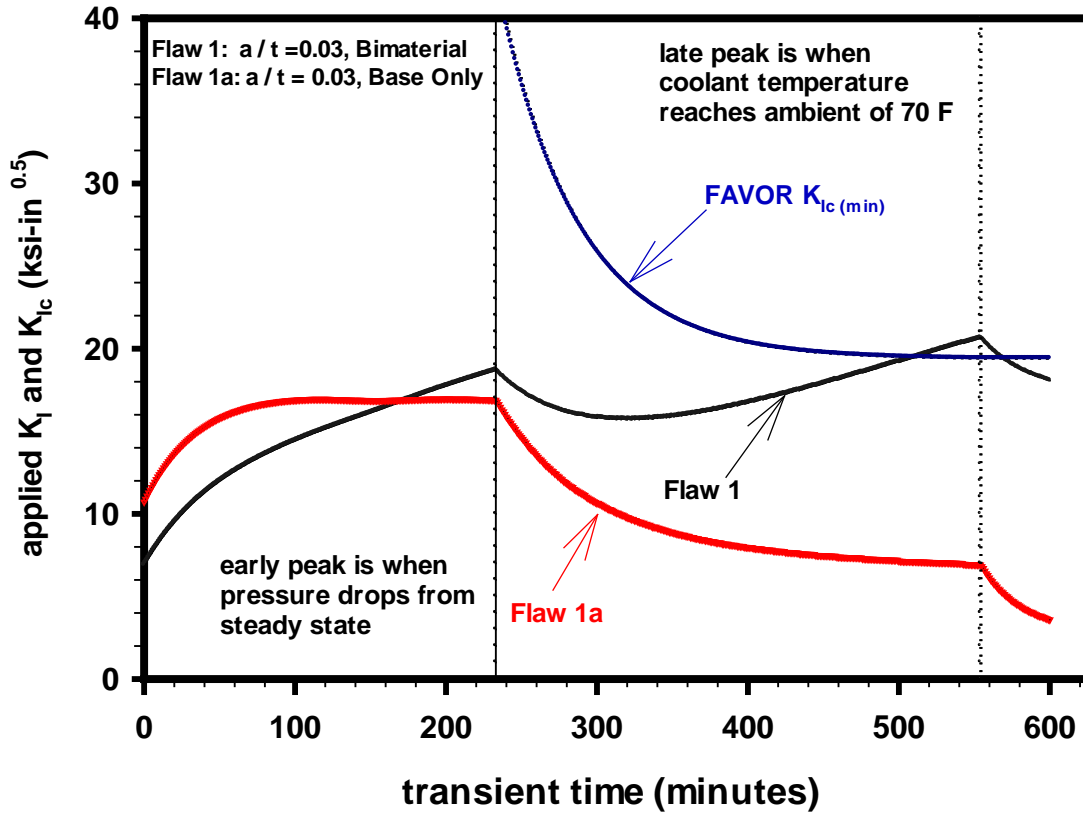


Fig. 1-6 K_I versus time curves for Flaw 1a ($a/t = 0.03$ with base material properties) and Flaw 1 ($a/t = 0.03$ with bi-material properties) subjected to postulated cool-down transient derived from the ASME code procedure and shown in Fig. 1-1.

1.4 Deep-flaw versus Shallow-Flaw Behavior

In Fig. 1-3, a very shallow surface-breaking flaw ($a/t = 0.03$) exhibits a CPI value that exceeds by orders of magnitude the value computed for the $1/4 t$ flaw referenced in the ASME Code, Section XI, Appendix G. A comparison of deterministic analysis results for those two flaws, combined with observations highlighted in discussions of Fig. 1-4 through Fig. 1-6, provide additional insights into that unexpected analysis result for computed CPI . Figure 1-7 depicts K_I versus time curves for the shallow flaw ($a/t = 0.03$) and for the deep flaw ($a/t = 0.25$) subjected to the postulated cool-down transient (Fig. 1-1) derived from the ASME code procedure. The applied K_I curves are compared with corresponding minimum-value fracture toughness curves from FAVOR; the ASME K_{Ic} curve for the $1/4 t$ flaw is also included for reference. Relevant observations concerning the comparative results of Fig. 1-7 include the following:

- The deep flaw exhibits *1st Peak Dominant* behavior (see Fig. 1-4). The first peak controls CPI and, because the peak applied K_I value is below the FAVOR $K_{Ic(min)}$ fracture toughness curve, then $CPI = 0$. The deep crack tip is influenced primarily by the pressure transient loading; the flaw tip is far removed from the clad layer and from effects of associated thermal loading (see Fig. 1-5).
- The shallow flaw exhibits *2nd Peak Dominant* behavior (see Fig. 1-4). The second peak controls CPI and, because the peak applied K_I value is above the FAVOR $K_{Ic(min)}$ fracture toughness curve, then $CPI > 0$; as noted earlier, values of CPI are much higher than for *1st Peak Dominant* conditions, even if applied K_I at the two peaks differs by only a small amount. The very shallow crack tip is influenced strongly by the proximity of the clad layer and the associated thermal loading that continues to ramp up throughout the transient (see Fig. 1-5).
- Late in the transient, the applied K_I curve for the 0.03t shallow flaw exceeds that of the deeper $1/4 t$ flaw. Because of warm-prestressing, the 0.03t flaw is critical for initiation, while the $1/4 t$ flaw is not.
- For the deep flaw, the applied K_I curve remains well below the associated ASME K_{Ic} curve for the entire transient. Thus, an ASME code assessment of the $1/4 t$ flaw would treat it as non-critical.

While the analysis results depicted in Fig. 1-7 represent a single deterministic assessment, the characteristics highlighted above can be generalized sufficiently to explain the ordering of CPI values presented in Fig. 1-3.

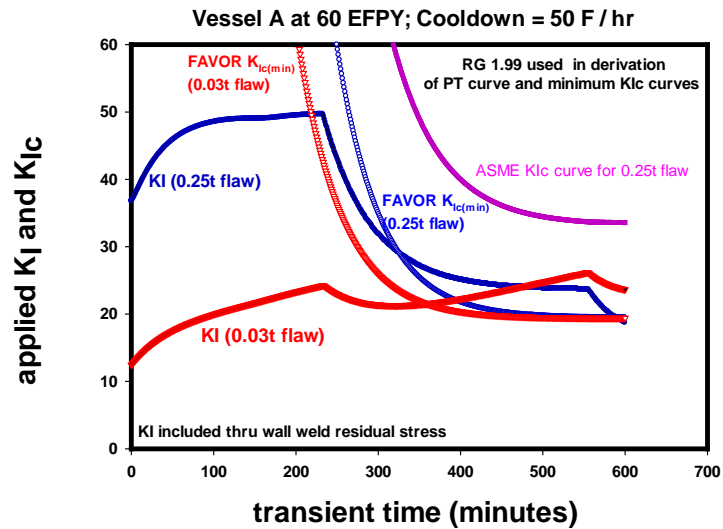


Fig. 1-7 K_I versus time curves for shallow flaw ($a/t = 0.03$) and for deep flaw ($a/t = 0.25$) subjected to postulated cool-down transient derived from the ASME code procedure (see Fig. 1-1); applied K_I are compared with fracture toughness curves from FAVOR and from ASME code.

1.5 Objectives

The previously-described analyses of postulated normal cool-downs for RPVs produced unanticipated results regarding the impact of very shallow, circumferential, ID surface-breaking flaws on the estimated probability of vessel failure as quantified by the *CPI* metric. As a consequence of those findings, ORNL performed the work reported in Sect. 2 to assess the accuracy and adequacy of the shallow-flaw cladding model implemented in the FAVOR computer code. Also, analyses were performed using FAVOR to assess the impact of various loading conditions (both normal operational cool-down and postulated accident) on shallow, surface-breaking flaws in RPVs (see Sect. 3). The outcome of these analyses permitted conclusions to be drawn (see Sect. 4) regarding the adequacy of the currently-configured FAVOR code to analyze shallow-flaws in clad RPVs, as well as any potential need to modify the FAVOR code to accurately perform such analyses.

1.6 Scope

The study described in this report to assess accuracy and adequacy of the inner-surface-breaking flaw model implemented in FAVOR and its application for different loading conditions is structured according to the outline given below.

In Sect. 2, *Adequacy / Accuracy of FAVOR Model*, the report is subdivided into the following sub-sections:

- Survey the literature for information concerning the physical attributes and the incidence of shallow flaws that have been found in stainless steel cladding of RPVs, i.e., “as-found” flaws.
- Provide a summary of the shallow-flaw/clad model implemented in the FAVOR code, identifying relevant assumptions embodied in that model.
- Assess whether the FAVOR code incorporates the features critical to modeling the behavior of observed shallow surface-breaking flaws under service loading conditions; those features include adequate and accurate representation of (1) vessel geometry/stress loading and (2) physical attributes and incidence of those flaws. Identify differences and discuss their expected impact on FAVOR analysis results.
- Perform finite element assessments that compare analysis results from the FAVOR inner surface-breaking flaw model with those obtained from the general-purpose finite-element code ABAQUS [7]; those assessments include both LEFM and elastic-plastic fracture mechanics (EPFM) results from ABAQUS.
- Assess the adequacy of the FAVOR inner surface-breaking flaw model (which is based on linear-elastic fracture mechanics (LEFM) methodology) in the context of more advanced fracture mechanics considerations, specifically, corrections for constraint loss [8].
- Provide conclusions regarding adequacy/accuracy of the FAVOR inner surface-breaking flaw model.

While the FAVOR model represents the unique physical and mechanical properties of the stainless steel cladding and the underlying ferritic RPV steel, FAVOR does not model the properties of the narrow heat-affected zone, or HAZ, between these two regions. Such a bi-material model that ignores the HAZ is consistent with common practice for RPV structural integrity assessment. The appropriateness of this approach is the subject of on-going investigations.

In Sect. 3, *Assessment of Shallow Flaws for Different Loading Conditions*, the report examines the following:

- Normal operational cool-downs following the maximum allowable pressure curve, including the ASME code procedure and risk-informed alternative approaches.
- Normal operational cool-downs following actual plant pressure, $P(t)$, and temperature, $T(t)$, records.

- Postulated accident cool-downs, i.e., PTS events.

In Sect. 4, *Potential Future Research*, several specific issues concerning the FAVOR shallow flow methodology are identified that may warrant further study to determine whether refinement of those features of the model could have a material effect on the major conclusions of this report. Those issues are briefly summarized for consideration by the NRC as future research topics.

Finally, Sect. 5, *Summary and Conclusions*, provides a summary of the objective and results of the study, as well as the major conclusions regarding adequacy and accuracy of the FAVOR inner surface-breaking flow model applied to actual RPV conditions.

2. Adequacy and Accuracy of the FAVOR Surface-Breaking Flaw Model

In this section, the adequacy and accuracy of the FAVOR inner surface-breaking flaw model is examined from several perspectives. First, the technical literature is surveyed to identify studies that provide information concerning the physical attributes and the incidence of shallow flaws that have been found in the stainless-steel cladding of RPVs. The FAVOR inner surface-breaking flaw model is summarized and then discussed in the context of whether that model captures the essential aspects of actual flaws subjected to operational loading conditions in a real RPV. The next step was to perform finite-element assessments that compare analysis results from the FAVOR inner surface-breaking flaw model with those obtained from the general-purpose finite-element code ABAQUS [7]. Also, the FAVOR inner surface-breaking flaw model (which is based on linear elastic fracture mechanics methodology) is examined in the context of more advanced fracture mechanics considerations: specifically, corrections for constraint loss [8]. Finally, some conclusions based on the study are noted regarding the adequacy/accuracy of the FAVOR inner surface-breaking flaw model.

2.1 Shallow Flaws in Stainless-Steel Cladding: Flaws Found in RPV Cladding Compared to the FAVOR Model

2.1.1 Description of the Flaws Found in RPV Cladding

In a previous study, Dickson et al [9] conducted a literature review concerning surface-breaking flaws that have been found in RPVs, as well as surface-breaking flaws that have been only postulated to exist. That study identifies several references that relate to the physical existence and to the morphology of shallow inner-surface-breaking flaws, including the following:

- (1) Inter-granular stress corrosion cracking (IGSCC) in the Quad Cities Unit 2 head [10],
- (2) IGSCC Cracks in the Japan Power Demonstration Reactor (JPDR) [11],
- (3) Clad fabrication defects in U. S. pressurized-water reactor vessels that were constructed according to commercial practice, but never put into service [12 - 13].

As noted by Dickson et al. [9], the defect data reported in refs. [10-11] provide evidence that inner surface-breaking defects can result from cladding defects related to fabrication processes, and then extend into the underlying ferritic layer by an inter-granular stress-corrosion cracking mechanism. In ref. [10], the through-clad defects documented for the Quad Cities Unit 2 head were reported to have a range of flaw depths that extend approximately ¼ in. into the ferritic base

material of the RPV⁸. Other than flaw depth, no data are provided regarding the morphology of those flaws, i.e., length, aspect ratios, whether a sharp crack or a volumetric defect, etc.

In an earlier study, the description by Kando et al [11] of the cladding failure in the JPDR pressure vessel provided optical micrographs of the found defects. Samples containing 8 mm-thick weld overlay cladding and 6 mm of the base metal were extracted from the ID of the BWR top head after 13,000 net hours of operation. The sample contained significant IGSCC. It was speculated that surface-breaking cracks had formed during the reactor operation period, although it was difficult to estimate the exact time of occurrence; ref. [11] notes that cracks were not observed during the pre-service examination with dye penetrant tests. Fig. 2-1 depicts typical cracks found in the clad layer. According to ref. [11], these morphological features suggest that the cracks formed first at the cladding surface, and they then propagated toward the base metal while branching in that process; the branches can be characterized as roughly planar, crack-like defects. Those branches of the clad cracks shown in Fig. 2-1 are seen in Fig. 2-2 and Fig. 2-3 to have extended across the fusion line into the base material as localized corrosion penetrations. Reference [11] describes the defect in Fig. 2-2 extending as “ditches” in the base metal along the tip of the crack. Fig. 2-3 depicts a complex topography of the interface in the base metal resulting from “pitting-type corrosion” in the narrow crevice. Reference [11] speculates that direct contact of the base metal with hot water that ingressed via the clad cracks was responsible for relatively rapid corrosion. Thus, the morphologies depicted in Fig. 2-1 through Fig. 2-3 show crack-like defects that branch in the clad layer and terminate in the base metal as local corrosion penetrations, the latter having the common characteristic of appearing as volumetric (blunted) defects.

References [12, 13, 14, and 15] describe research performed by Pacific Northwest National Laboratory (PNNL) to document the occurrence rates of fabrication flaws in RPV materials. Those studies (for example, ref. [12]) describe experimental work that involved application of nondestructive and destructive techniques to vessel material to generate a database on fabrication flaws in the RPV. Material sources were from vessels fabricated for nuclear power plants that were cancelled before going into service. That work covered vessel fabrication from the late

⁸ From ref. [10], p. 127:

“In 1990, Quad Cites Unit 2 visually detected defects (stain patches) at various points on the RPV head cladding. Dye penetrant and UT examinations were performed to determine the extent of the defects. The defects (cracks) had a maximum depth of approximately 6 mm in the base material. The cracking was attributed to IGSCC and possibly hot cracking. Subsequent examinations in 1990, 1992, and 1995, using ultrasonic through-wall sizing and VT-1 and VT-3 methods, have indicated no change (no evidence of growth, increased severity, or decrease in component integrity).”

1960s through the early 1980s, when most vessels currently in commercial operation were constructed. Vessels studied by PNNL include PVRUF, Shoreham, and Hope Creek II (see ref. [15]). The fabrication flaw data were developed to quantify the following factors:

- flaw densities
- flaw locations
- flaw sizes (through-wall depth dimensions and lengths)

Regions of the RPV included in these studies were main seam welds, repair welds, base metal, and cladding on the inner surface of the vessel.

Estimates of the expected number and size distribution of fabrication flaws in the beltline cladding of a RPV were a major focus of the PNNL studies. Attention was directed to the following:

- (1) surface-breaking flaws that penetrate the full thickness of the clad and extend to the underlying weld or base metal, and
- (2) larger buried flaws in the cladding that extend up to the clad/base metal interface but do not entirely penetrate the thickness of the clad.

Major sources of clad flaw data were those observations made during destructive and nondestructive examinations of the PVRUF vessel (see refs. [12, 13, 14, and 15]). The clad in PVRUF consisted of submerged-arc strip clad, as well as manual metal-arc clad, and multi-wire clad. Most of the inspected cladding was deposited as strip clad to the PVRUF vessel in a single pass using a welding machine that produced a cladding thickness of 3/16 in. Manual cladding was used over circumferential welds, over areas that were difficult to weld with the cladding machine, and for repairs to the clad surface. The volume of clad material examined in the PVRUF study was 0.95 ft³ [12], which represents approximately 46 ft² of the clad area lining the RPV.⁹ Results from destructive and nondestructive evaluations were summarized as follows:

- A large number of flaws were detected in the PVRUF cladding, but none of those flaws was surface-breaking.

⁹ The beltline region of a representative RPV (pressurized water reactor) is estimated to have a clad inner surface area of approximately 630 ft². Thus, the surface area examined in the PNNL studies is estimated to be approximately seven percent of the beltline region in a single RPV.

- Buried flaws were found in the vessel. An example of such buried clad flaws is shown in Fig. 2-4, which depicts a cross section of clad from the PVRUF vessel with two buried flaws in close proximity at the clad/base interface. It was speculated that such flaws occur due to (1) lack of inner-run fusion and (2) defects at the start/stop position of the cladding beads. Most of these flaws are very small.
- The morphology for buried flaws found at the clad/base metal interface exhibited many of the characteristics of volumetric defects, as opposed to crack-like flaws; again, see Fig. 2-4 for two examples of clad defects.

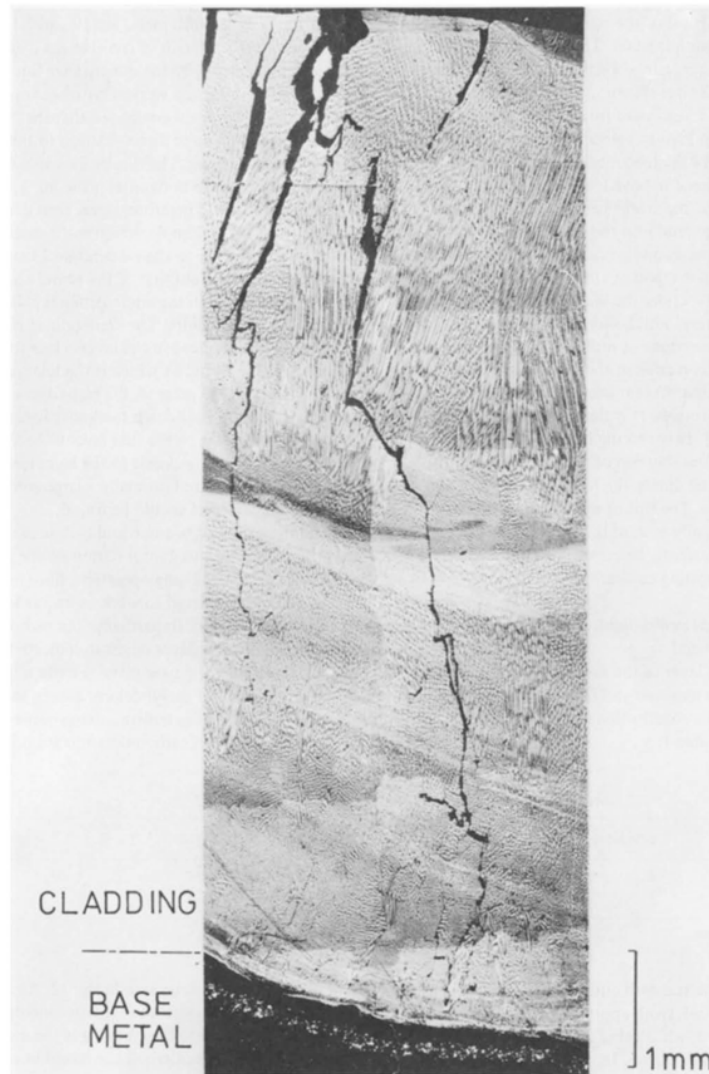


Fig. 2-1 Optical micrograph of cracks extending through cladding into base metal (extracted from ref. [11]).

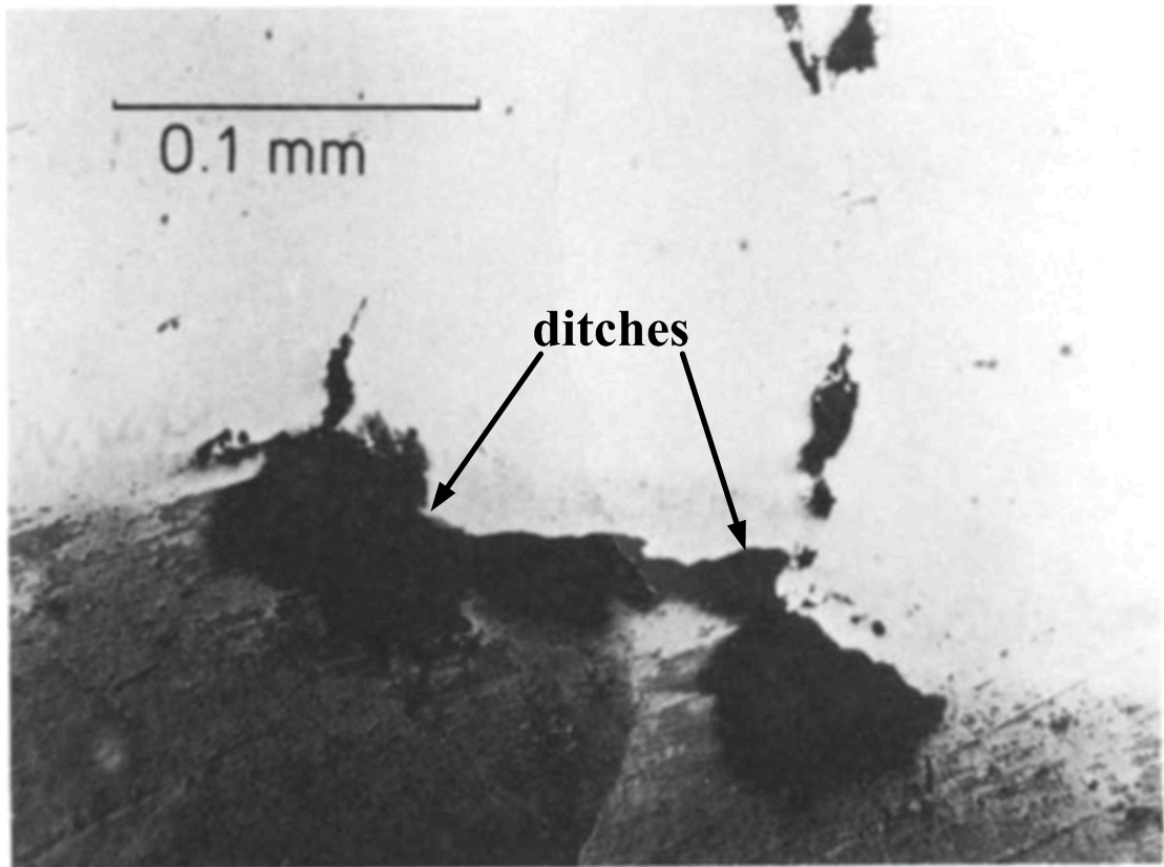


Fig. 2-2 Corrosion of base metal at the end of clad crack (extracted from ref. [11]) showing the defect extending as “ditches” in the base metal along the tip of the crack.

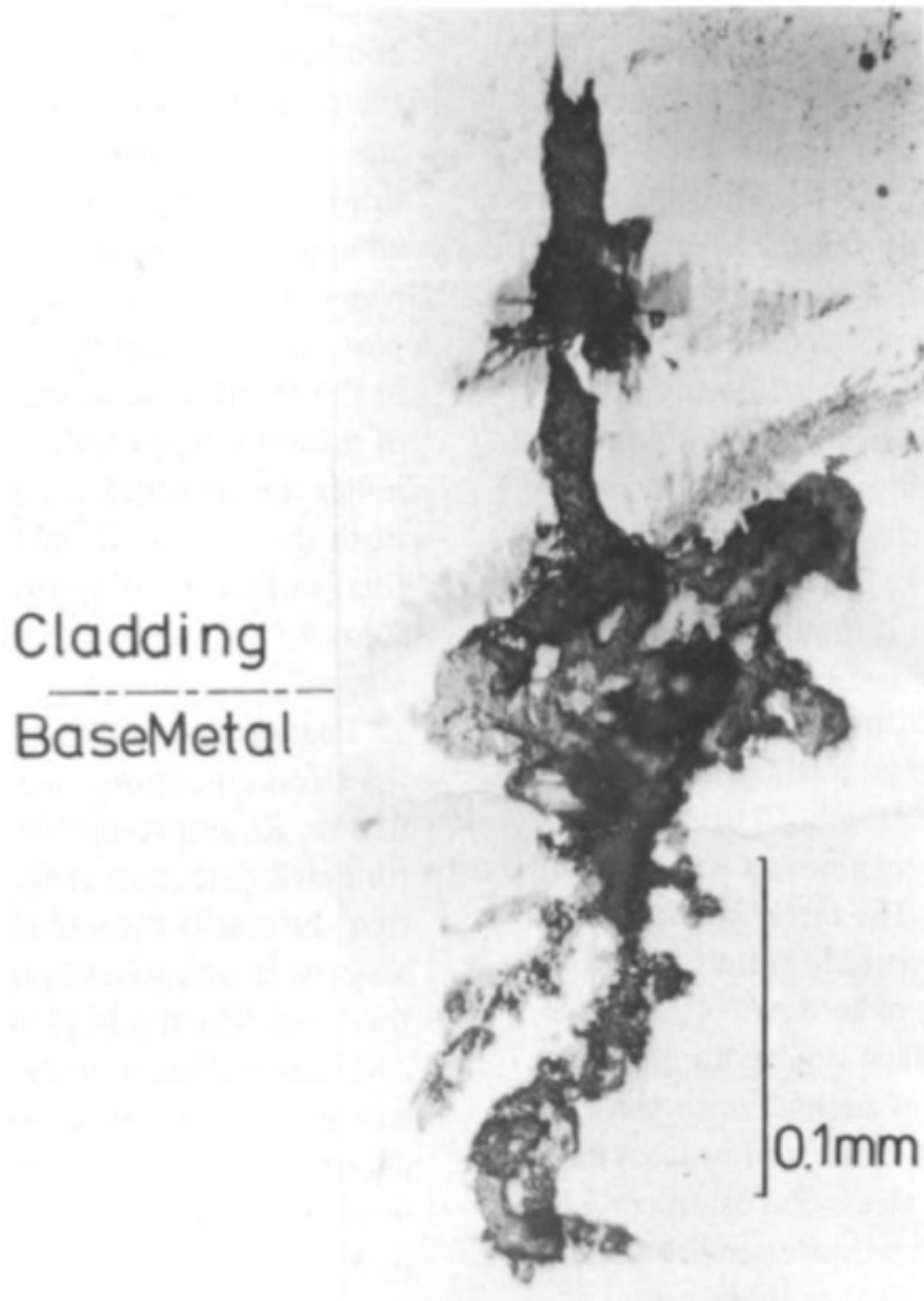


Fig. 2-3 Surface-breaking crack found in JPDR (extracted from ref. [11]), showing a complex topography of the interface in the base metal resulting from a “pitting-type corrosion” in the narrow crevice.

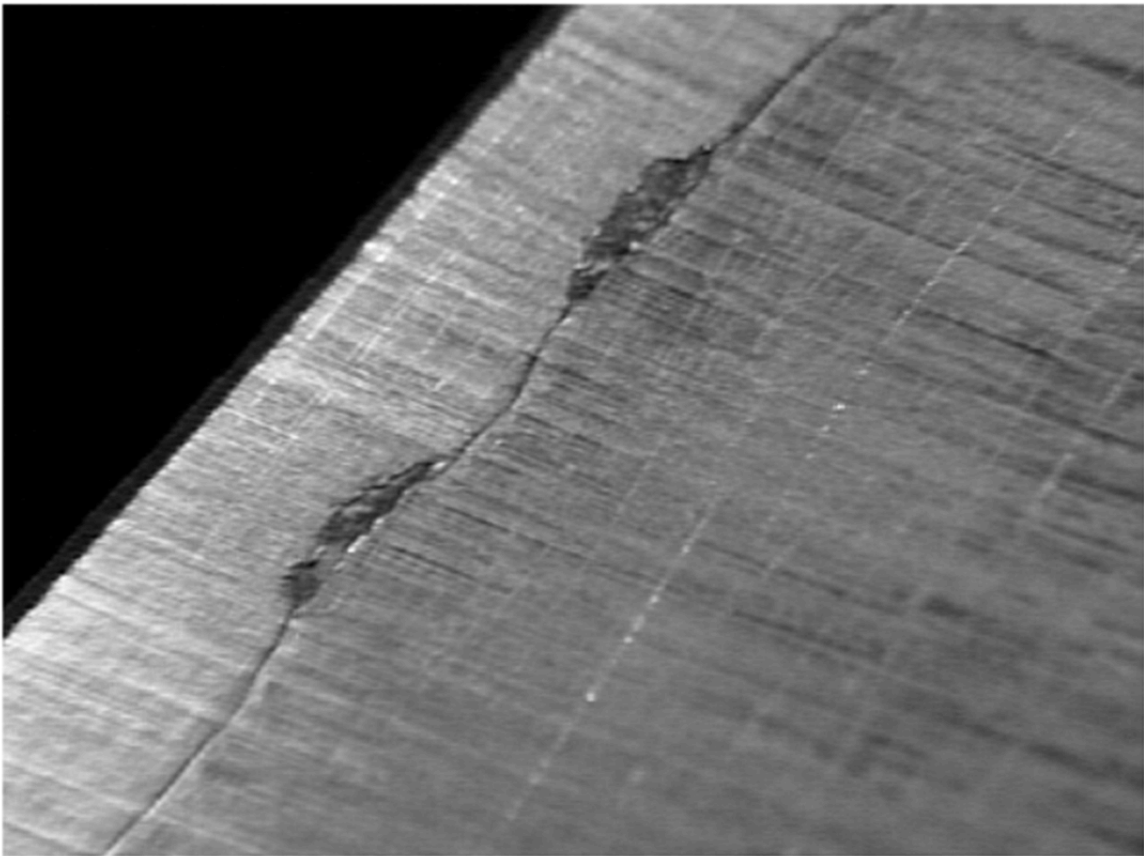
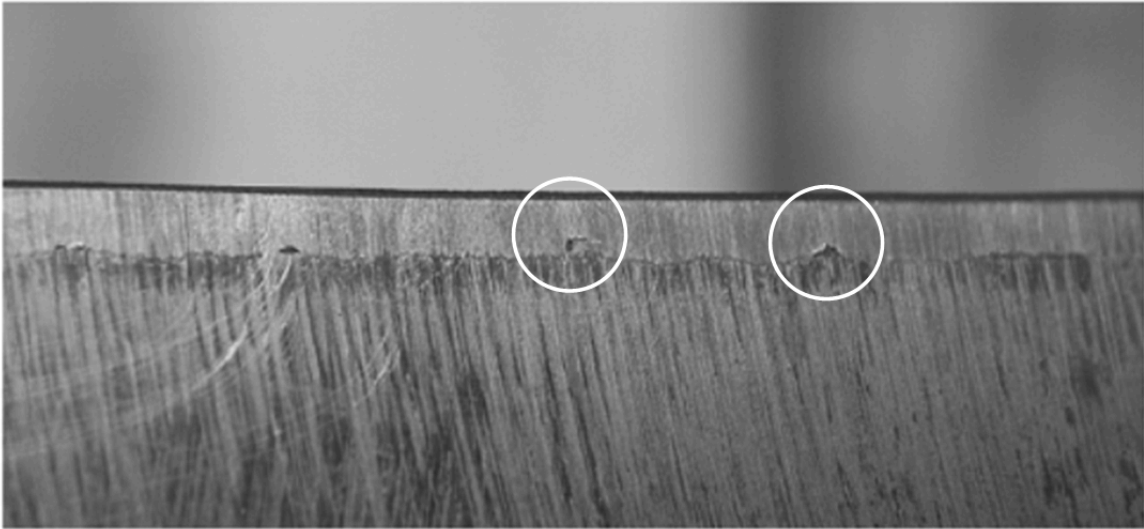


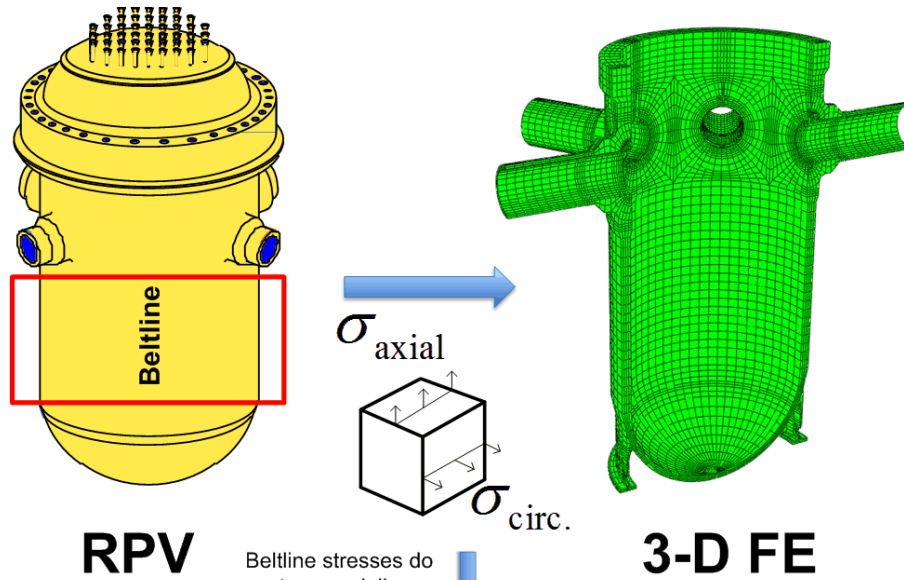
Fig. 2-4 Examples of flaws in cladding of PVRUF vessel (extracted from ref. [12])

2.1.2 Description of the FAVOR Inner Surface-Breaking Flaw Model

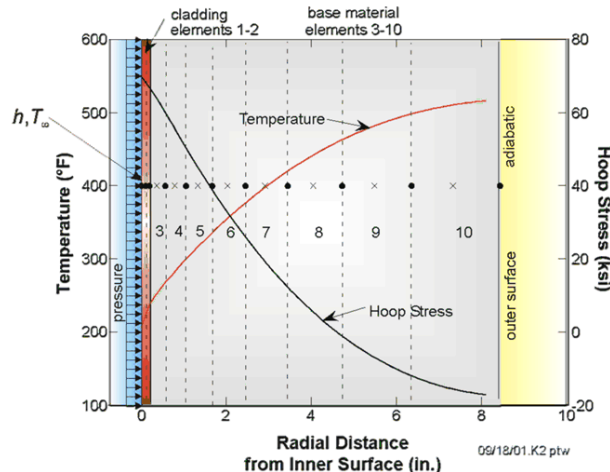
The essential features of the FAVOR model [1] used to assess flaw behavior and structural integrity in a RPV subjected to normal and postulated accident loading conditions are summarized in this section. Full details can be found in the FAVOR theory manual [1].

FAVOR Geometry/Stress Model

The FAVOR [1] code uses heat conduction and thermo-elastic stress solutions, as well as superposition techniques, to calculate applied K_I factors for postulated surface-breaking flaws in a RPV cylinder. The focus is on analyses of the beltline region of the RPV [1] subjected to thermal-hydraulic transients, including both cool-down and heat-up events. In the FAVOR model, the beltline region of the RPV wall extends from approximately one foot above to one foot below the active reactor core (see Fig. 2-5). Characteristics of the internal structure and thermal/fluid mixing in the RPV produce temperature and pressure boundary conditions that are essentially uniform over the beltline region during a thermal-hydraulic transient (Ref. [16]). Thus, the temperature and stress within the beltline region of the RPV are dependent on the radial coordinate direction, but (approximately) independent of the axial and circumferential coordinates. The FAVOR code takes advantage of the latter conditions by modeling a long cylinder with free ends and no axial or circumferential variations in temperature or material properties. Specifically, a one-dimensional (radial) axisymmetric model of the vessel wall is employed to perform a displacement-based finite-element analysis of the vessel, as illustrated in Fig. 2-5. Numerous studies [17, 18] have been performed to validate FAVOR's one-dimensional (1-D) model of temperature and stresses in the RPV beltline region versus predictions from detailed three-dimensional (3-D) finite-element models; an example 3-D finite-element model is also shown in Fig. 2-5. In Fig. 2-6, axial and hoop stresses from FAVOR 1-D model are shown to be in good agreement with those obtained from an ABAQUS analysis of the 3-D model at a specific location in the beltline; such agreement is typical over the beltline region of the 3-D model. Thus, the FAVOR 1-D axisymmetric model realistically simulates the geometry and stress fields in the beltline region of a RPV subjected to thermal-hydraulic transients.



Beltline stresses do not vary axially or circumferentially.



FAVOR1-D FE

Not to Scale

Fig. 2-5 FAVOR model realistically simulates the geometry and stress fields experienced in RPV beltline subjected to thermal-hydraulic transients.

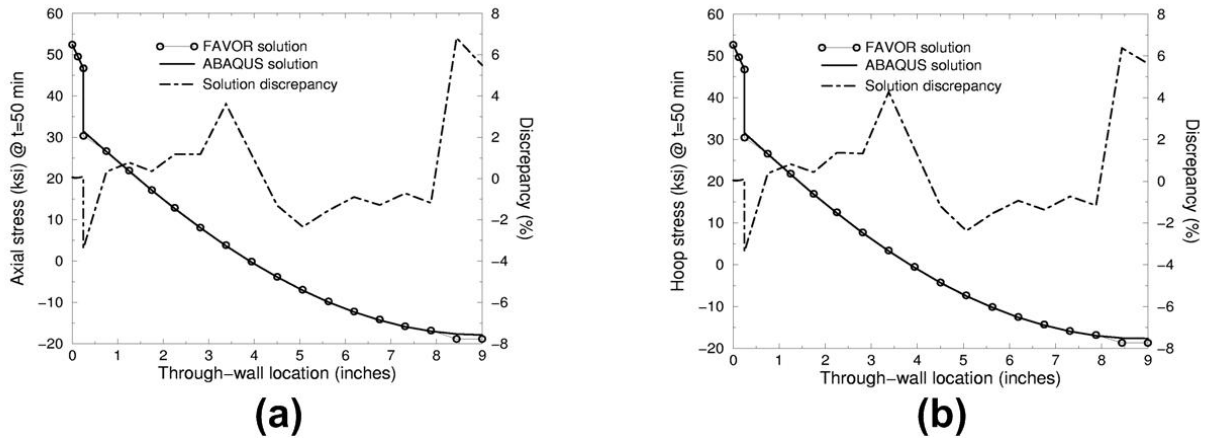


Fig. 2-6 Comparison of FAVOR 1-D and ABAQUS 3-D model predictions: (a) axial stress and (b) hoop stress analysis for a RPV subjected to a thermal-hydraulic transient.

Temperature and Stress FE Models

The FAVOR code carries out finite-element analyses of a one-dimensional axisymmetric model of the RPV wall to estimate through-wall gradients of temperature and stress; a graded finite element mesh (see Fig. 2-7) is generated through the wall thickness using ten three-node quadratic isoparametric axisymmetric elements (21 nodes). The thermal and stress models use the same quadratic elements and graded-mesh discretization. In the thermal analysis, the transient heat conduction equation with temperature-dependent properties is solved for the combined cladding and base materials to produce time-varying temperature profiles through the wall. Next, the finite-element stress analysis calculates radial displacements and then strain-displacement and linear-elastic stress-strain relationships; time varying axial and hoop stress profiles are also calculated. These stresses include the effects of thermal and mechanical loading (internal pressure applied to the inner vessel surface and exposed crack face), along with the option of superimposed weld residual stress¹⁰ profiles [19]. Effects of differences in the thermal expansion capabilities between the cladding and base materials are included by specifying a stress-free temperature and differences in temperature-dependent material properties. The time-dependent temperature and stress distributions through the wall constitute the thermal and mechanical loading that is applied to postulated flaws in the wall of the RPV.

¹⁰ The applied K_I values calculated for flaws positioned in weld material include effects of weld residual stresses, whereas flaws positioned in plate material are not subjected to those stresses. Discussion of the criteria for application of weld residual stresses in this study is included in Appendix A.

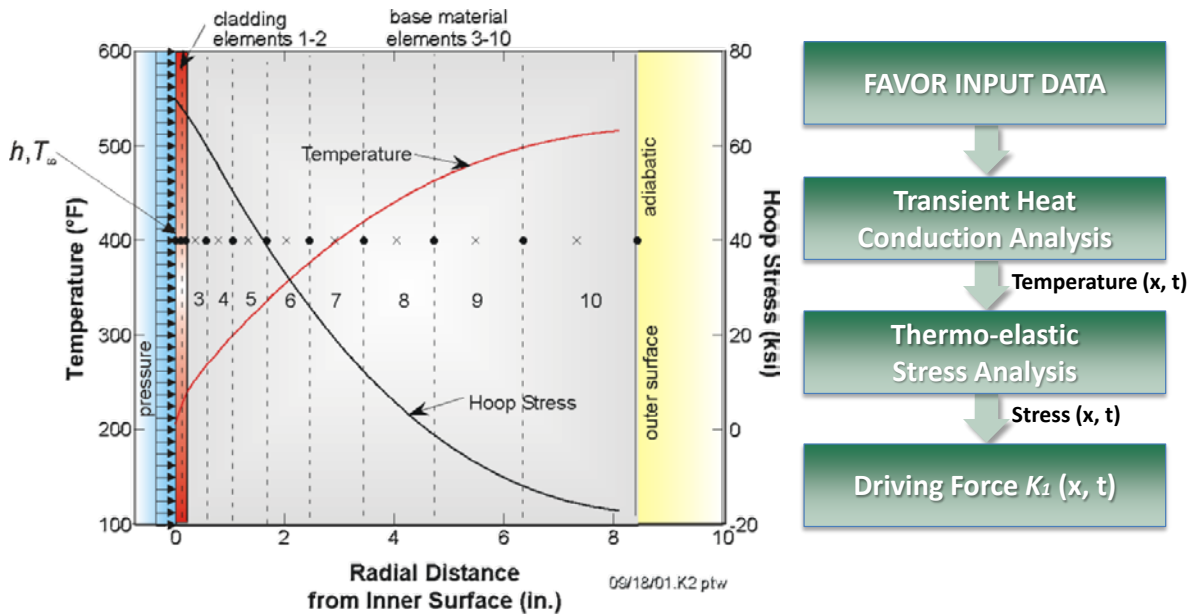


Fig. 2-7 Transient heat conduction and thermo-elastic stress analyses performed using one-dimensional axisymmetric finite element model of un-cracked RPV wall.

FAVOR Model Flaw Inputs

In ref. [12], Simonen et al. (PNNL) document how flaw-related inputs were generated for FAVOR¹¹. Estimates for flaw data input to FAVOR were based on the following sources of information:

- (1) data on observed flaws obtained from destructive and nondestructive examinations of the PVRUF and Shoreham vessels [13, 20, and 21];
- (2) simulations of flaws with the PRODIGAL computer code [[22];
- (3) NRC expert judgment elicitation on vessel flaws [23].

The experimental work [12] involved application of nondestructive and destructive techniques to vessel materials to generate a database on fabrication flaws in welds, base metal, and cladding in RPVs; that work was described in Sect. 2.1.1. To supplement the limited data from these measurements, the PNNL study [12] incorporated additional tasks:

- calculations were performed with the PRODIGAL code [22] to estimate flaw sizes and densities in all of the RPV beltline materials, including the inner-surface cladding.

¹¹ Reference [12] also played an important role in formulating the technical bases for development of 10CFR50.61a; that role included generation of flaw-related input data for PTS analyses performed using the FAVOR code.

Reference [12] noted that development of a clad model was a significant part of building the PRODIGAL code.

- discussions were conducted with a panel of U.S. experts on welding and vessel fabrication to establish values for parameters used to quantify the frequencies for flaws in vessel materials.

Using these inputs, PNNL developed statistical distribution functions [12] to characterize the number and sizes of flaws in the various regions of a RPV. Calculations were performed using those flaw distribution functions and procedures that were implemented into a computer algorithm¹² [12]. That algorithm performs Monte Carlo calculations that sample from the uncertainty distributions for the parameters of the flaw distribution functions. Each application of the flaw distribution algorithm generates a data file for use as input to the FAVOR code. The flaw distribution algorithm provides three input files for the FAVOR code; one of these files describes surface-breaking flaws in the clad region of the vessel.

FAVOR Surface-Breaking Flaw Model

The surface-breaking flaw model incorporates the following key features:

- All inner-surface flaws are oriented circumferentially because in the examinations of the PVRUF vessel all of the observed flaws in the cladding were circumferentially oriented. This observation was consistent with expectations, because weld-deposited cladding is applied to vessel inner surfaces as a series of circumferential weld passes. In the FAVOR model, all inner surface-breaking flaws are associated only with the vessel cladding process. A recommendation of ref. [12] is that no surface-breaking flaws be postulated in multiple layer cladding.
- Regarding crack morphology, all flaws are assumed to be planar, not volumetric. While the actual morphology of some of the flaws observed in these studies was somewhat blunted relative to idealized cracks (for example, see Fig. 2-4), this assumption is consistent with the generally planar nature of the flaws observed in the examinations as well as with standard fracture mechanics practice.
- Regarding flaw proximity considerations, the model of surface flaw density and size should be considered as already accounting for random occurrences of small flaws that are sufficiently close to each other to be treated as a single larger flaw for the purpose of fracture mechanics calculations.

¹² The computer algorithm is explained in ref. [12].

- All internal, surface-breaking, semi-elliptical flaws that initiate in cleavage fracture¹³ are assumed to become infinite length (or uniform depth) internal surface-breaking flaws (both semi-elliptical and uniform depth flaws are depicted in Fig. 2-8). The phenomenon, that an ID flaw initiating in cleavage during a cooling transient will (initially) extend much more in length than it does in depth, was empirically demonstrated in large-scale, heavy-section, thermal-shock experiments [24] that involved testing of short flaws in both unclad and clad thick cylinders. Further discussion of this assumption is provided in Appendix D.

Additional details concerning the treatment of clad flaws are documented in ref. [12], as are the available flaw data and other sources of information that support the flaw model.

Applied K_I Calculations for Through-Clad Flaws

Calculation of applied K_I for postulated flaws is based on the principles of LEFM. The flaws are assumed to experience only Mode I loading, where the principal load is applied normal to the crack plane, thus tending to open the crack. FAVOR uses the method of superposition to calculate the applied K_I for a range of infinite-length and finite-length (semi-elliptical) ID surface-breaking flaw geometries. The superposition technique combines results from stress analysis of an uncracked vessel with stress intensity factor influence coefficients (SIFICs) determined for a range of flaw geometries. This technique produces accurate values of applied K_I for those flaw geometries subjected to complex time-history loading conditions. Considerable computational efficiency is achieved with this approach because 3-D models are required only once to calculate the SIFICs. FAVOR includes a comprehensive database of SIFICs for internal and external surface breaking flaw depths, in both axial and circumferential orientations, that are applicable to pressurized water reactor (PWR) and boiling water reactor (BWR) geometries. Fig. 2-8 depicts circumferentially-oriented, internal surface-breaking flaws for four discrete aspect ratios, i.e., 2:1, 6:1, 10:1, and uniform depth (or infinite), that are built into the SIFIC database of the FAVOR code. Appendix E of this document and the FAVOR theory manual [1] provide further details of the method of superposition and SIFICs.

¹³ The flaw analyses described in the report are focused strictly on brittle (cleavage) fracture of a flaw tip that is postulated to reside in the base (ferritic) steel wall of the RPV; for very shallow flaws (eg., $a/t = 0.03$), the tip is located in the base metal just beyond the clad/base interface. The ductile tearing mechanism relevant to the clad is not considered a factor in brittle fracture initiation in the base material.

Fig. 2-9 illustrates the model implemented in FAVOR for calculation of applied K_I for through-clad flaws. The thin layer of stainless steel cladding on the inner surface of the RPV can have a significant effect on the K_I values for ID surface-breaking flaws. The higher CTE of the cladding, compared to the underlying base metal, leads to an elevation of thermal stresses in the cladding during a thermal transient, shown in Fig. 2-9. Thus, the difference in CTEs is responsible for a steep thermal stress gradient present in a small zone around the clad/base metal interface. In the FAVOR LEFM model, that small zone is idealized as having zero thickness.

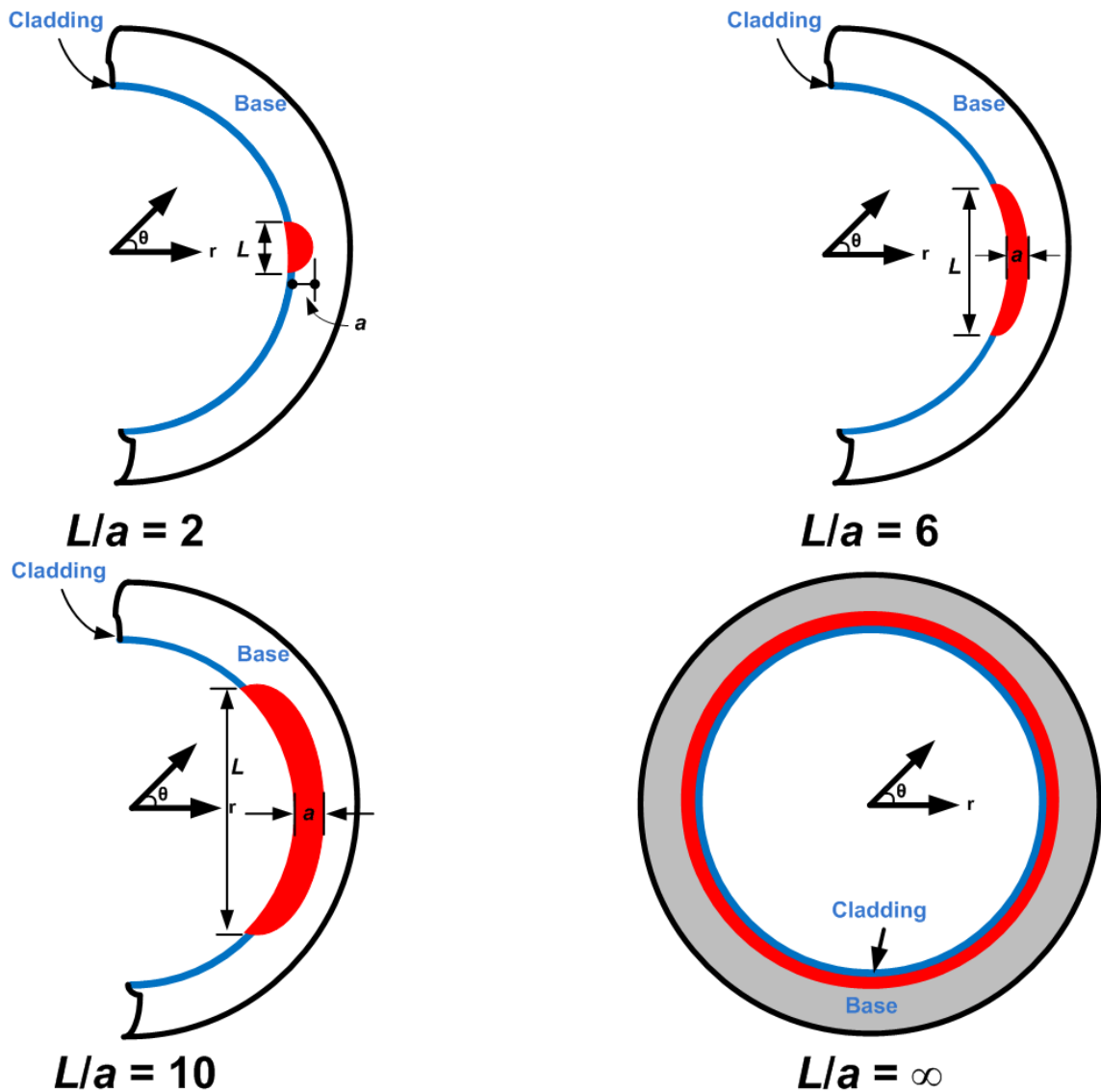


Fig. 2-8 Circumferential surface-breaking flaws postulated in FAVOR [1] (not to scale) showing four aspect ratios (length/depth): 2:1, 6:1, 10:1 and uniform depth (infinite)

The superposition technique and the FAVOR database of SIFICs are used to account for differences in clad and base metal material properties when calculating K_I for surface breaking flaws (see Fig. 2-9 for reference), as follows:

1. At a specific transient time, the crack-opening stress profile through the wall is generated from the thermo-elastic stress analysis of the un-cracked RPV.

2. The total stress (σ_{total}) in the base metal is linearly extrapolated into the cladding material, and the difference of the total stress in the cladding ($\sigma_{total-clad}$) and the extrapolated σ_{base} is defined as σ_{clad} .
3. For a surface crack of depth "a", the computed stresses σ_{base} and σ_{clad} are used with the database of SIFICs to calculate individual base (K_{Ibase}) and clad (K_{Iclad}) contributions to a total crack driving force (K_{Itotal}). Thus,

$$K_{Itotal} = K_{Ibase} + K_{Iclad} \quad (2.1)$$

Appendix E of this document and the FAVOR theory manual [1] provide further details of the FAVOR clad model. Also, Appendix E provides details pertaining to the treatment in FAVOR of the following:

- Superposition techniques to calculate applied K from database of SIFICs
- Determination of clad stress-free temperature
- Inclusion of weld residual stresses

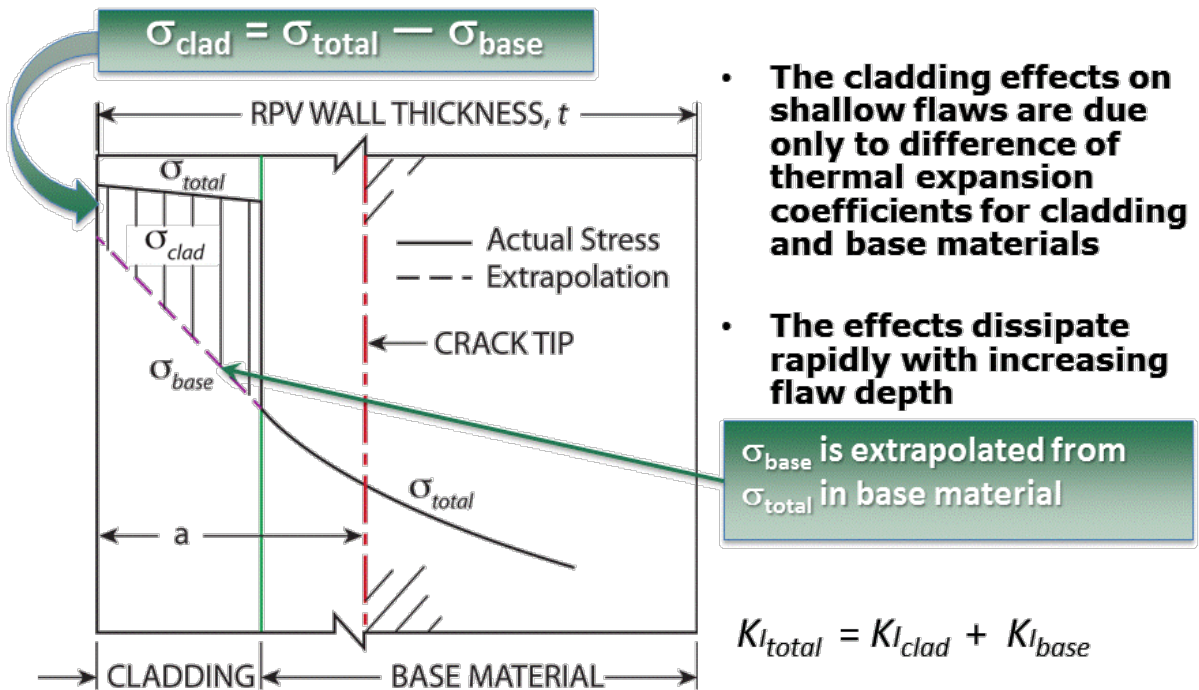


Fig. 2-9 Cladding model implemented in FAVOR

2.1.3 Assessment of the FAVOR Model applied to Shallow Flaws in Cladding

In this section, the FAVOR code presented in Sect. 2.1.2 is evaluated in the context of whether it incorporates the features necessary for modeling essential characteristics of actual flaws found in clad RPVs and described in Sect. 2.1.1. Table 2-1 provides a summary of factors relevant to assessing adequacy of the FAVOR code applied to shallow flaws observed in RPV cladding; characteristics of shallow flaws are addressed in Table 2-1(a) and clad/base metal in Table 2-1(b). The summary draws from discussions presented in Sects. 2.1.1, 2.1.2, and Appendix D. Specifically, the following factors are considered:

1. characteristics of shallow flaws and cladding/base metal region
2. physical evidence related to item 1
3. features of FAVOR that address the relevant characteristics
4. assessment of the adequacy and accuracy of FAVOR.

Based on the assessment that appears in the right-most column of Table 2-1, the model implemented in the FAVOR code is judged to incorporate the features necessary to represent actual flaws found in stainless steel cladding of RPVs.

2.2 Finite Element Assessment: FAVOR Compared to ABAQUS

In this section, the adequacy and accuracy of the shallow-flaw model implemented in the FAVOR code is evaluated by comparing analysis results from FAVOR with those obtained from the general-purpose finite-element code ABAQUS [7]¹⁴. Three-dimensional finite element models with finite-length, circumferential, shallow surface cracks are analyzed with ABAQUS to further evaluate the FAVOR solutions. EPFM analyses of the same ABAQUS models are used to assess the relative importance of non-linear modeling effects not included in the FAVOR LEFM model.

¹⁴ In Appendix B, simple two-dimensional (2-D) axisymmetric finite element models of shallow surface flaws are analyzed with ABAQUS. The ABAQUS results are compared with results from FAVOR. Those analyses also provide mechanistic insights into the applicability of LEFM methodology.

Table 2-1 Assessment of the FAVOR Model Applied to Shallow Flaws Observed in Stainless Steel Cladding of RPVs (a) Shallow Flaws

Characteristics of Shallow Flaws or Cladding/Base Metal	Physical Evidence	FAVOR Model	Assessment of FAVOR
SHALLOW FLAWS			
Depth	1/ Quad Cities – through-clad flaw, 6 mm into base metal 2/ JPDR – through-clad flaw, <1 mm into base metal, see Fig. 2-1 through Fig. 2-3 3/ PVRUF – sub-clad, ~1 mm at clad-base interface, see Fig. 2-4	For PFM analysis, surface flaw depths are specified in discrete multiple increments of 0.01t (t = wall thickness)	Able to accurately represent this physical evidence
Length	1/ Quad Cities – unknown 2/ JPDR – unknown 3/ PVRUF – sub-clad, ~5 mm, see Fig. 2-4	Length is determined by specification of depth and discrete aspect ratio of 2:1, 6:1, 10:1, or 360 degree continuous	Able to accurately represent this physical evidence
Aspect ratio	PVRUF – 5:1 (estimated), see Fig. 2-4	Four aspect ratios are prescribed: 2:1, 6:1, 10:1, 360 degree continuous	Able to accurately represent this physical evidence
Density	1/ Quad Cities and JPDR - Low incidence of found through-clad flaws 2/ PVRUF - no found through-clad flaws	FAVOR accepts any user-specified value; PNNL model used by FAVOR prescribes 3.7×10^{-3} flaws per square foot of clad area	Model judged adequate, based on model inputs from PNNL (i.e., observed data, simulations, and expert judgment) and on the use and acceptance of these inputs in the development of the Alternate PTS Rule (10 CFR 50.61a).
Orientation	Circumferential because the clad layers were deposited circumferentially	Circumferential inner flaws	Able to accurately represent this physical evidence
Notch Acuity	1/ Quad Cities – assumed blunted, due to IGSCC 2/ JPDR – blunted (or volumetric), see Fig. 2-1 through Fig. 2-3 2/ PVRUF - no found through-clad flaws; sub-clad flaws tend to be blunted	Planar (sharp)	Model somewhat conservative, but not overly so because (a) the presence of planar aspects at the tips of volumetric cracks cannot be ruled out and (b) the limited empirical evidence cannot establish that all flaws in service will be blunted.
Connected to ID?	1/ Quad Cities – yes 2/ JPDR – yes 3/ PVRUF – no found surface flaws	Yes	Able to accurately represent this physical evidence

Table 2-1 Assessment of the FAVOR Model Applied to Shallow Flaws Observed in Stainless Steel Cladding of RPVs (b) Cladding/Base Metal

Characteristics of Shallow Flaws or Cladding/Base Metal	Physical Evidence	FAVOR Model	Assessment of FAVOR
CLADDING / BASE METAL			
CTE of cladding	In Ref. 19, experimental data combined with analytical models allow quantification of differential thermal expansion effects; also, see Appendix E	ASME Code, Sect. II, Part D, Material Group D, Table TE-1 (includes SS304)	Adequate
CTE of base metal	In Ref. 20, experimental data combined with analytical models allow quantification of differential thermal expansion effects; also, see Appendix E	ASME Code, Sect. II, Part D, Material Group D, Table TE-1 (includes A533B)	Adequate
Cladding thickness	PVRUF (example) – ~5 mm (~0.2 in), see Fig. 2-4	FAVOR permits modeling of 4 mm (0.156 in.) and 6.4 mm (0.25 in.) thick cladding; linear interpolations used for intermediate clad thicknesses; extrapolation used for values below 4mm; values exceeding higher option are capped at 6.4 mm.	Model judged adequate, based on typical cladding thicknesses in vessels and comparative analyses using detailed 3-D models
Cladding HAZ	Has HAZ	No HAZ	Model judged adequate despite absence of HAZ (see Ref. 9)
Clad stress-free temperature (SFT)	ORNL experimental measurements and analyses, see description Appendix E	Model uses value of SFT = 488 °F	Model judged adequate, based on RPV experimental data and analytical studies (see Appendix E)

2.2.1 Three-Dimensional Model Analyses

Three-dimensional finite element models were constructed for a 180-degree segment of a RPV shell wall containing circumferential, finite-length, ID surface breaking flaws. The finite element model consists of 20-node isoparametric brick elements for the main structure, as shown in an example in Fig. 2-10 ($a/t = 0.05$). Collapsed prism elements were employed at the crack tip to produce an appropriate singularity for LEFM analyses. Two flaw models were constructed for the ABAQUS analyses (see Table 2-). Only $\frac{1}{4}$ of the RPV cylindrical wall is represented in the FE model, which has two symmetry planes. The height of the finite-element RPV model is set to be sufficiently large to not influence the analysis results, and boundary conditions are applied to simulate the plane-strain condition as used in the FAVOR code. Additional details concerning vessel geometry, material properties, and loading conditions are given in Appendix B.

The 3-D finite element models are subjected to a transient derived using the risk-informed method with a 50° F/hr cool-down rate (see Fig. 1-4). Fig. 2-11 gives the ABAQUS and FAVOR K_I versus time curves for $a/t = 0.03$ surface flaw geometry. The FAVOR K_I curve agrees well with the ABAQUS solution. Both K_I predictions exhibit a local maximum at 216 minutes and then reach the maximum applied K_I at 554 minutes. The FAVOR code uses only 10 axisymmetric elements, while there are 13,488 twenty-node brick elements used in the ABAQUS 3-D finite element model.

Fig. 2-12 displays the ABAQUS and FAVOR K_I versus time curves for $a/t = 0.05$ surface flaw model. The FAVOR solution matches well with 3-D finite element results. Both K_I curves reach the maximum applied K_I at 216 minutes, followed by a lower peak at 554 minutes. There is better agreement between the $a/t = 0.05$ results (FAVOR vs. ABAQUS) than for the $a/t = 0.03$ results. This is because FAVOR has influence coefficients for the $a/t = 0.05$ flaw but not for the $a/t = 0.03$ flaw. Cubic spline curve fitting is used to interpolate results for the $a/t = 0.03$ flaw [1]. Apparently, application of SIFICs computed for the actual flaw depth in question provides improved accuracy compared with interpolation within the tabulated SIFIC data. Even with these small differences, the interpolation scheme is deemed adequate.

An EPFM analysis is conducted for the RPV model with the finite-length, shallow, circumferentially oriented inner-surface breaking flaw ($a/t = 0.03$) subjected to the same vessel geometry and loading conditions as the LEFM analyses. Elastic-plastic material properties [25] are used; additional details are given in Appendix B. Fig. 2-13 compares the LEFM and EPFM K_I curves generated from ABAQUS analyses. Early in the transient, linear-elastic conditions prevail

and the two analyses agree. Both K_I curves reach the maximum applied K_I at 554 minutes. The ABAQUS analysis of the 3-D EPFM model reduces the maximum applied K_I by approximately 11% because plastic deformation of the cladding reduces the stress imposed on the crack tip region, see Fig. 2-13. The plastic deformation of the cladding and the crack tip reduces the peak K_I values from the EPFM analysis, but the second peak K_I value still exceeds the first peak K_I value. Therefore, the late peaking effect on K_I that is responsible for the high CPI and CPF values is also present in the more realistic 3-D EPFM analysis.

Table 2-2 Geometry Parameters of the Flawed RPV Models

Case Number	Flaw Information			
	Flaw Type	Flaw Orientation	Dimensions	
			Depth (in)	Aspect Ratio (L/a)
1	Inner-surface	Circumferential	0.2625	6:1
2	Inner-surface	Circumferential	0.4375	6:1

- **Finite-element model for PWR with a inner circ. surface flaw, 6:1 aspect ratio:**

- **Inside radius of 86 inches**
- **Wall thickness, t , of 8.75 inches**
- **Clad thickness, t_{clad} , of 0.25 inches**
- **20-node quadratic brick elements**

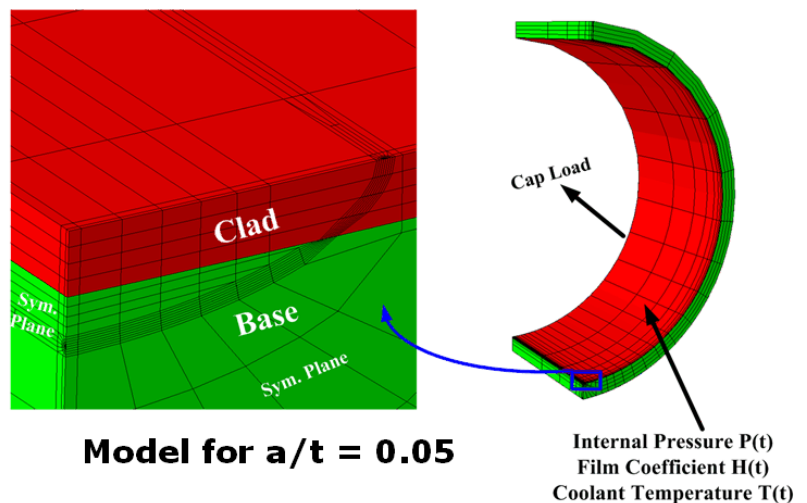


Fig. 2-10. Finite-element model for PWR with an ID circumferential surface flaw ($a/t = 0.05$)

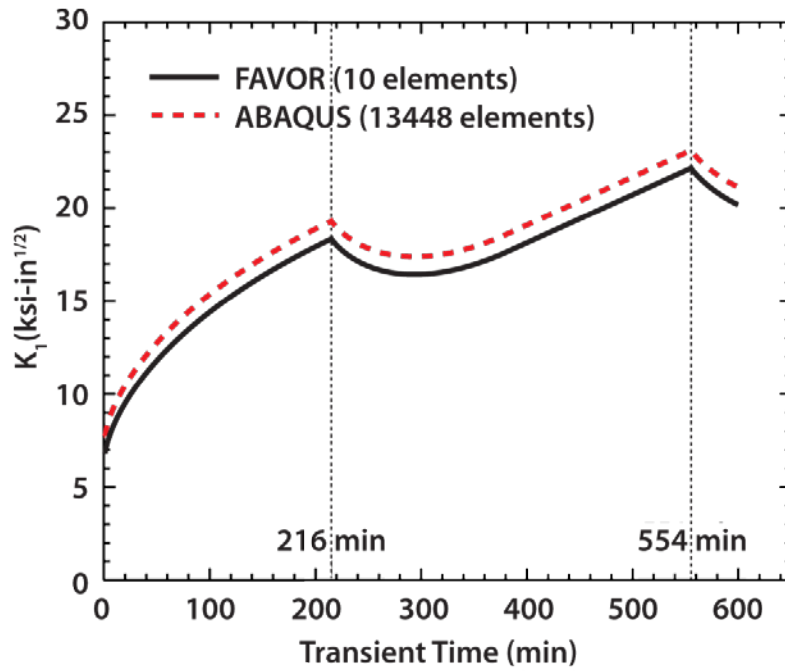


Fig. 2-11 Comparison of K_I versus time curves for shallow flaw $a/t = 0.03$. Vessel A subjected to P-T limits determined from EPRI risk-informed method based on 60 EFPY and cool-down rate of 50 °F/hr.

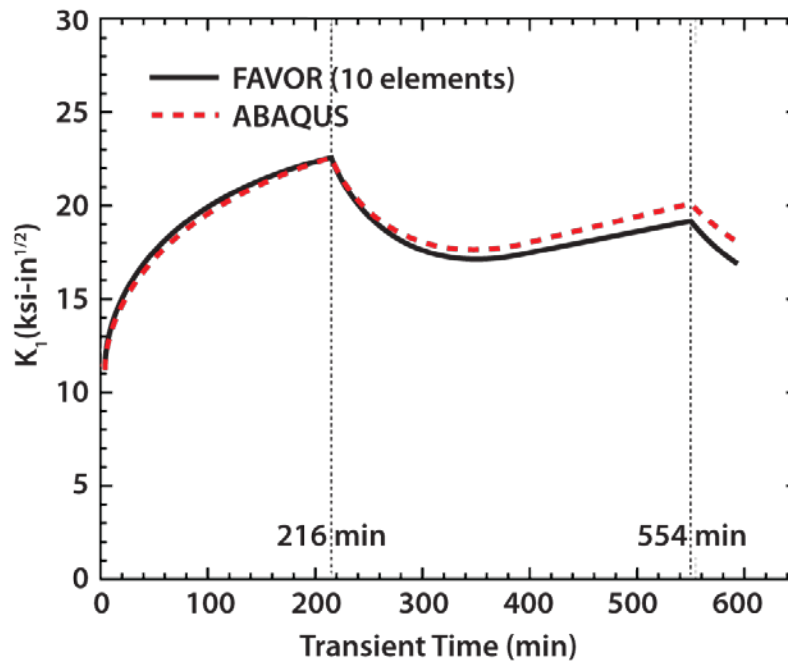


Fig. 2-12 Comparison of K_I versus time curves for shallow flaw $a/t = 0.05$. Vessel A subjected to P-T limits determined from EPRI risk-informed method based on 60 EFPY and cool-down rate of 50 °F/hr.

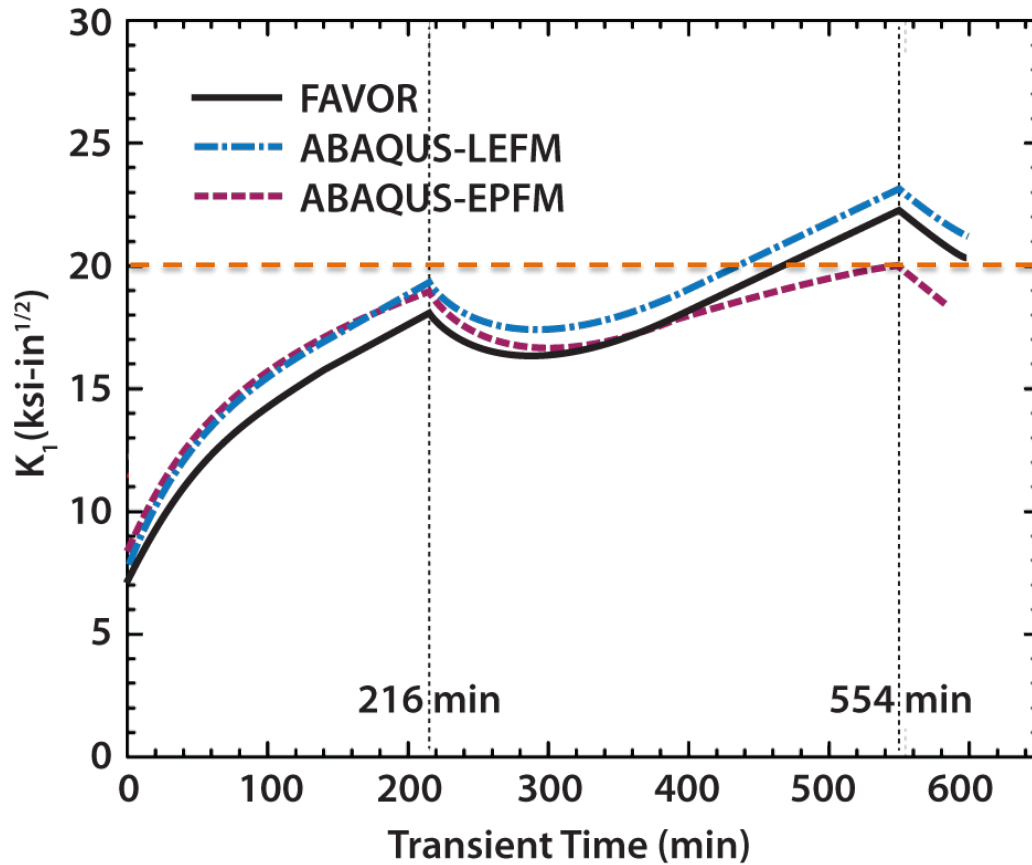


Fig. 2-13 Comparison of LEFM and EPFM K_I versus time curves for shallow flaw $a/t = 0.03$. Vessel A subjected to P-T limits determined from EPRI risk-informed method based on 60 EFPY and cool-down rate of 50 °F/hr.

2.3 Advanced Fracture Mechanics Considerations: Loss of Constraint (T-stress)

The adequacy and accuracy of the LEFM-based FAVOR shallow-flaw model were evaluated in the context of more advanced fracture mechanics considerations that focus specifically on corrections for constraint loss [8]. In cleavage fracture, loss of crack-tip constraint leads to an elevation of effective fracture toughness of the engineering structure relative to that measured with standard laboratory specimens. Pronounced loss of constraint necessitates much larger applied K_I values to generate stresses sufficient to trigger cleavage fracture in the structure, thus causing LEFM predictions of failure to be overly pessimistic. Analyses are described below that assess constraint conditions for shallow ID surface flaws.

Williams [26] showed that the crack-tip stress fields in an isotropic elastic material can be characterized with a series of asymptotic solutions:

$$\begin{aligned}
\sigma_{xx}(r,\theta) &= \frac{K_I}{\sqrt{2\pi r}} f_{xx}(\theta) + T + O(r,\theta) \\
\sigma_{yy}(r,\theta) &= \frac{K_I}{\sqrt{2\pi r}} f_{yy}(\theta) + T + O(r,\theta) \\
\tau_{xy}(r,\theta) &= \frac{K_I}{\sqrt{2\pi r}} f_{xy}(\theta) + T + O(r,\theta)
\end{aligned}
\tag{2.2}$$

where the crack-tip stress fields are schematically illustrated in Fig. 2-14.

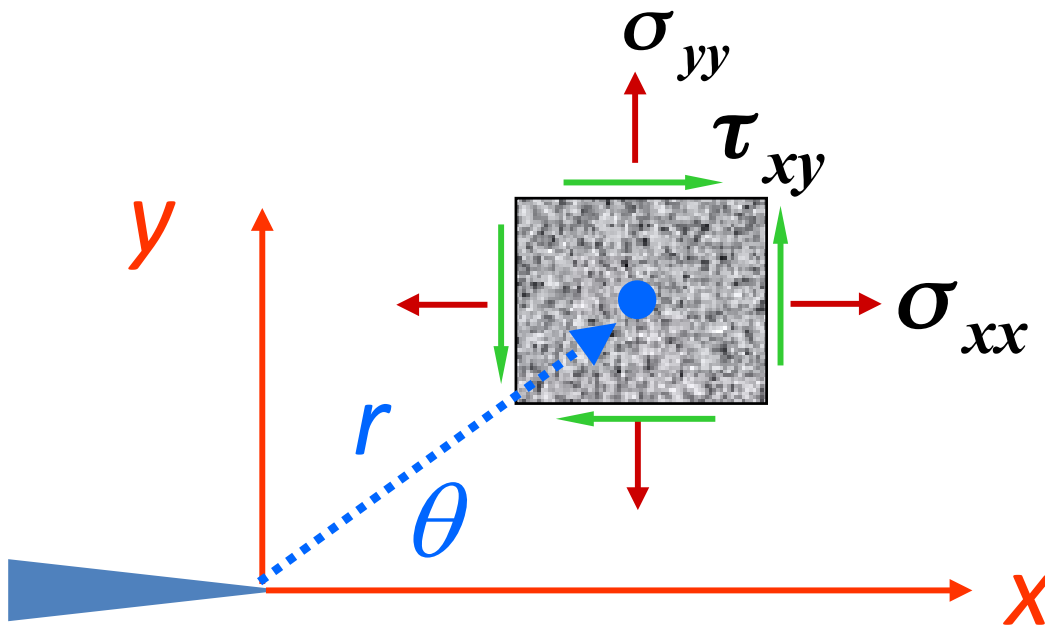


Fig. 2-14 Schematic view of crack-tip stress fields.

In the crack-plane direction (x direction as shown in Fig. 2-14), the second term (T) is a uniform stress. This “ T -stress” provides the first-order parameter to quantify the constraint effects produced by different geometries and/or loading types on measured values of fracture toughness [8], as follows:

- T -stress < 0 implies low constraint, which can significantly increase measured toughness;
- T -stress > 0 implies high constraint, which has a minor effect on measured toughness.

Wallin [8] experimentally developed and verified a relation between the T -stress and the Master Curve transition temperature T_0 . His analysis also indicates that positive T -stress has an insignificant effect on fracture toughness, whereas for negative values of T -stress, the Master Curve indexing temperature T_0 reduces linearly with T -stress as described in Eq. (2.3):

$$T_0 \approx T_{0deep} + \frac{T_{stress}}{10 \text{ MPa}/^\circ\text{C}} \text{ for } T_{stress} < 0 \quad (2.3)$$

Combined with the Master Curve methodology [8], the linear relationship in Eq. (2.3) between T -stress and T_0 can provide an approximate constraint correction for the effect of constraint loss on fracture toughness:

$$K_{JC} \approx 20 \text{ MPa}\sqrt{\text{m}} + \left(K_{Jc deep} - 20 \text{ MPa}\sqrt{\text{m}} \right) \exp \left[0.019 \left(\frac{-T_{stress}}{10 \text{ MPa}} \right) \right] \text{ for } T_{stress} < 0 \quad (2.4)$$

With the assumption of LEFM, T -stress was calculated from the 3-D finite element model ($a/t = 0.03$) subjected to a transient with 50° F/hr cool-down rate, as shown in Fig. 2-15(a). T -stress solution from ABAQUS 3-D FEM for cool-down transient shows positive values at time of maximum applied K_I (second peak at 554 minutes), as shown in Fig. 2-15(b); thus, no increase in effective fracture toughness is predicted by Wallin model as described in Eqs. (2.3) and (2.4). Consequently, loss of constraint is not considered an issue for these shallow flaws, demonstrating the appropriateness of the LEFM-methodology used by the FAVOR code.

2.4 Conclusions Regarding Adequacy/Accuracy of the FAVOR Surface-Breaking Flaw Model

Results of this study confirm that the FAVOR model includes the necessary features for adequate and accurate representation of shallow, ID surface-breaking flaws subjected to service loading conditions in a RPV¹⁵. That conclusion is supported by the following summary of the evidence presented in this section that focuses on three key features of the FAVOR code:

Representation of shallow flaws in RPVs: FAVOR was shown to model the critical aspects of shallow flaws in RPVs that have either been found in service or that cannot be conclusively ruled out in the context of a probabilistic / risk-informed assessment of vessel integrity. Specifically,

¹⁵ Previous verification studies of the FAVOR code include the independent NRC-funded assessment performed by Southwest Research Institute, which is described in the ref. [27].

shallow ID surface-breaking flaws have been found in service in some cases (i.e., Quad Cities and JPDR), those arising due to IGSCC. Also, examination of fabrication defects in the PVRUF vessel material revealed the possibility of lack-of-fusion defects between adjacent cladding strips.

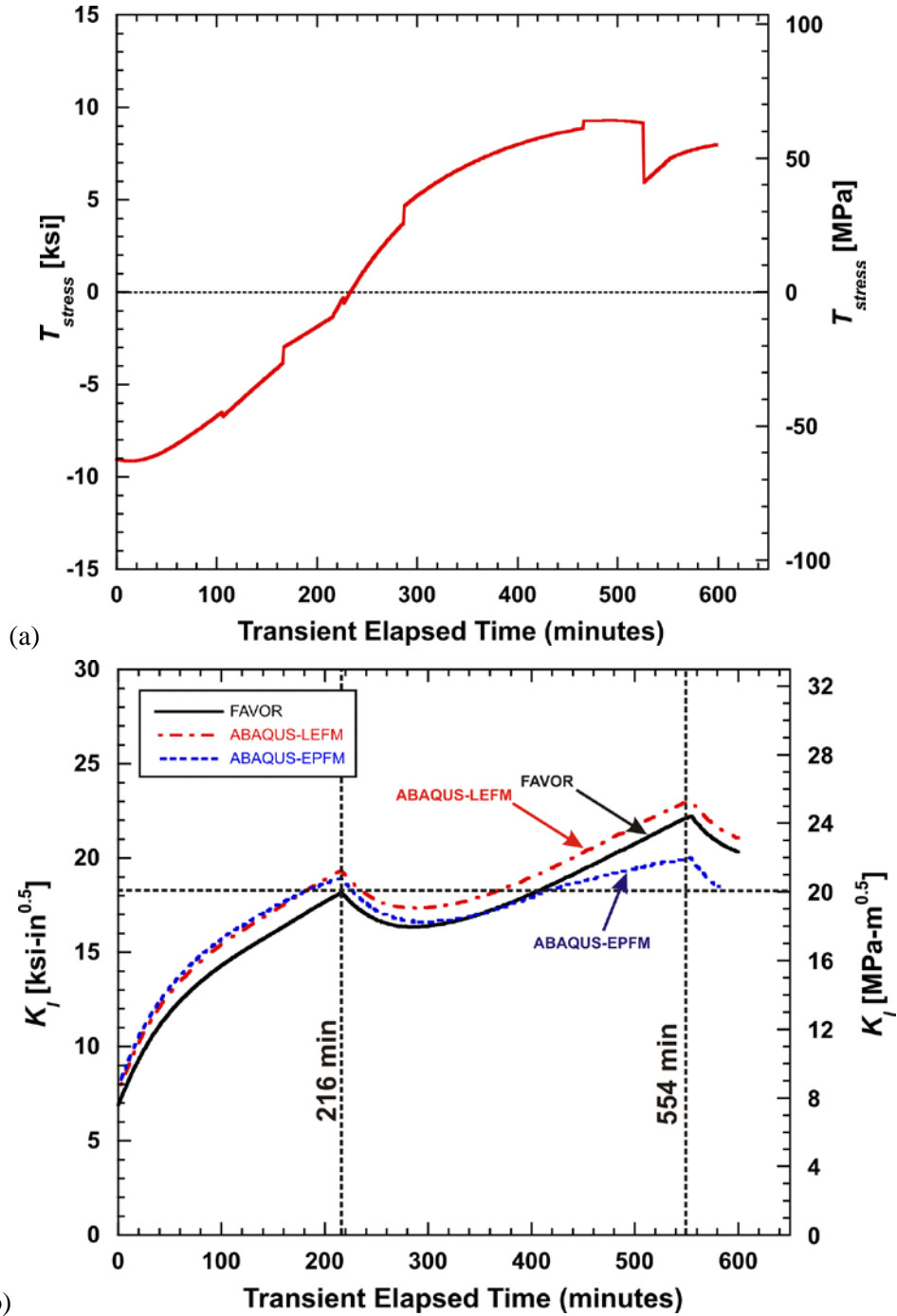


Fig. 2-15 (a) T -stress history for Flaw 1 $a/t = 0.03$; (b) Comparison of LEFM and EPFM K_I versus time curves for Flaw 1 $a/t = 0.03$. Vessel A subjected to P-T limits determined from EPRI risk-informed method based on 60 EFPY and cool-down rate of 50 °F/hr.

While these defects were not surface breaking, a panel of experts convened by the NRC judged the amount of material examined inadequate to justify *a priori* elimination of surface breaking defects from RPV integrity analyses [23]. Based on available information, the FAVOR model that incorporates 0.0037 circumferentially oriented surface-breaking flaws per square foot of clad area was judged to be appropriate in [12]; this value was adopted in the development of 10 CFR 50.61a. Those flaws exist in close proximity to a high-stress gradient that is generated by the CTE mismatch between the austenitic cladding and the ferritic base material. As this stress gradient depends on differences in physical, rather than mechanical, properties for its existence, it is judged to be appropriate and to have greater certainty than aspects of the model that depend on mechanical properties. The FAVOR model does not represent the HAZ between the cladding and the base metal. However, this treatment is consistent with current worldwide analytical practice and, in any event, reasonably accurate in view of the limited grain refinement associated with single or dual clad layers. Also, the FAVOR model treats all flaws as being ideally sharp at the crack tip. While some evidence presented in this section suggests a volumetric nature to the crack-tips of interest, sharp features in service cannot be ruled out. As a result, the FAVOR shallow-flaw model is judged to be adequate based on the information available.

Application of LEFM methodology: As it does for all flaws, FAVOR evaluates the effect of shallow ID flaws on vessel integrity using LEFM equations and LEFM-based failure models. Evaluations performed in this section demonstrate that a more accurate EPFM representation of flaw driving force and failure is not significantly different for those flaws subject to the loadings and geometric conditions of interest.

Moreover, an assessment of the potential for increased toughness caused by constraint loss (a feature that is not part of the FAVOR model) revealed that, for those flaws subject to the loadings and geometric conditions of interest, there is no constraint loss. These shallow surface-breaking flaws exist in a state of high crack-tip constraint, making use of the LEFM-based fracture models adopted by FAVOR completely appropriate.

Further validation of the FAVOR LEFM-based fracture models is provided by a demonstration that FAVOR can be used to successfully predict the results of large-scale fracture experiments. Reference [29] documents FAVOR analyses of the first large-scale pressurized-thermal-shock experiment performed at ORNL, i.e., PTSE-1 [30]. Results of deterministic and probabilistic fracture analyses performed with FAVOR accurately predicted cleavage fracture initiation of long, surface-breaking flaws in a large-scale thick-walled pressure vessel for two separate transients (PTSE-1B and -1C) that were applied to the vessel.

Simulation of RPV geometry/stress fields: The FAVOR code uses heat conduction and thermo-elastic stress solutions to model loading of the beltline region of the RPV subjected to thermal-hydraulic transients. It is well documented that temperature and pressure boundary conditions are essentially uniform over the beltline region during a thermal-hydraulic transient, rendering the temperature and stress within that region dependent only on the radial coordinate direction (Ref. [16]). The FAVOR code takes advantage of the latter conditions by employing a 1-D (radial) axisymmetric model of the vessel wall to analyze the beltline. This FAVOR 1-D model has been validated through numerous comparisons with detailed 3-D finite-element models, demonstrating excellent agreement with the 3-D model calculations for stress components and for shallow-flaw stress-intensity factors. Thus, the FAVOR 1-D axisymmetric model realistically simulates the geometry and stress fields in the beltline region of a RPV subjected to thermal-hydraulic transients.

3. Assessment of Shallow Flaws for Different Loading Conditions

In this section, an assessment of shallow flaws using the FAVOR inner surface-breaking flaw model is discussed for the following loading conditions:

- normal cool-downs following the maximum allowable pressure curves derived from the ASME code procedure [2] and the EPRI-MRP-250 risk-informed [5] method,
- normal cool-downs following pressure, $P(\tau)$, and temperature, $T(\tau)$, curves recorded during a shutdown operation of a nuclear RPV, and
- postulated accident cool-downs following pressure and temperature versus time curves associated with PTS events.

The effects of these different loading conditions on vessel integrity are quantified using the *CPI* and *CPF* metrics used in Sections 1 and 2.

3.1 Postulated Normal Cool-downs That Follow the Maximum-Allowed Pressure

Sections 1 and 2 of this report presented analysis results from the FAVOR code that illustrate the challenge presented by shallow, inner surface-breaking flaws to the structural integrity of RPVs. Those analyses used the maximum allowable pressure curve based on the ASME code procedure [2]. The trend of non-monotonic variation of *CPI* with initial flaw depth was shown previously for one case in Fig. 1-3. As a further example, Fig. 3-1 shows that the method used to determine the maximum allowable pressure curve, whether ASME code procedure or risk-informed approach [5], does not fundamentally change how the *CPI* values change with flaw depth. For those two methods of determining postulated cool-down curves that follow maximum pressure, the computed *CPI* for very shallow flaws ($a = 0.03t$) exhibits a maximum above that associated with a $\frac{1}{4} t$ flaw. A detailed discussion of results from application of the maximum allowable pressure curve was provided in Section 1.2.

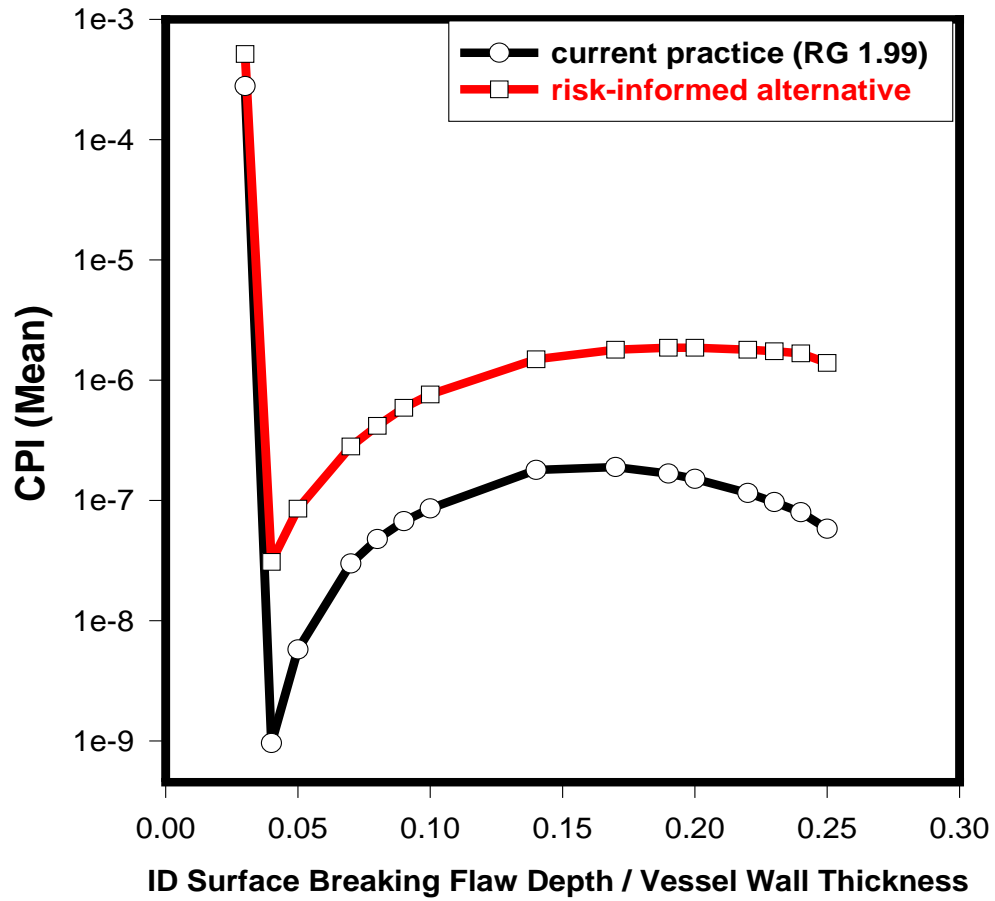


Fig. 3-1 *CPI* values for Vessel A after 60 EFPY for cool-downs at 100 °F/hour along the maximum-allowable pressure curves calculated using both ASME code procedure and EPRI risk-informed alternative P-T limit equations

3.1 Normal Cool-downs That Follow Actual Plant Pressure and Temperature Records

Coolant pressure and temperature versus time curves for four normal cool-down transients, recorded at operating nuclear power plants, are shown in Fig. 3-2. Those transients are analyzed so that *CPI* and *CPF* values (versus normalized flaw depth) for actual transients can be compared with those determined for a postulated transient that follows the maximum allowed pressure; all transients were applied to Vessel A at 60 EFPY. Comparisons shown in Fig. 3-3 demonstrate that *CPI* values for shallow flaws having depths just slightly greater than the cladding thickness are again much greater than those for deeper surface-breaking flaws in general, and the $\frac{1}{4} t$ flaw in particular. Also, Fig. 3-3 shows that the *CPI* for shallow surface flaws is reduced substantially (by two or more orders of magnitude) when the actual transients are followed. Additional results presented in Fig. 3-4 indicate that *CPF* values for the shallowest flaws are reduced by at least four orders of magnitude for the same actual transients.

3.2 Postulated Accident Cool-downs (PTS Events)

In the foregoing sections, PFM analyses performed for postulated normal cool-down transients demonstrate that inclusion of shallow, ID surface-breaking flaws significantly increases the propensity for brittle fracture, when compared with predictions for deeper flaws. These trends were observed over a range of cool-down rates and EFPYs, and lead to the following question:

Why does the inclusion of surface-breaking flaws have a significant impact on the results of PFM analyses performed for postulated normal operational transients, whereas such flaws did not have a significant impact on results for PTS assessments [29, 32 and 33]?

The PTS re-evaluation studies [28, 31 and 32] differed from those discussed herein in two important aspects. First, shallow surface-breaking flaws were modeled in only one of the three plants included in those studies, i.e., Oconee Unit 1. Second, in the PTS studies, analysis results were expressed in terms of TWCF, which is *CPF* (one metric used in these studies) weighted by the frequency of occurrence of each PTS transient. Nevertheless, those differences are not sufficient to explain the relative unimportance of shallow surface-breaking flaws for PTS versus their importance for postulated normal cool-downs.

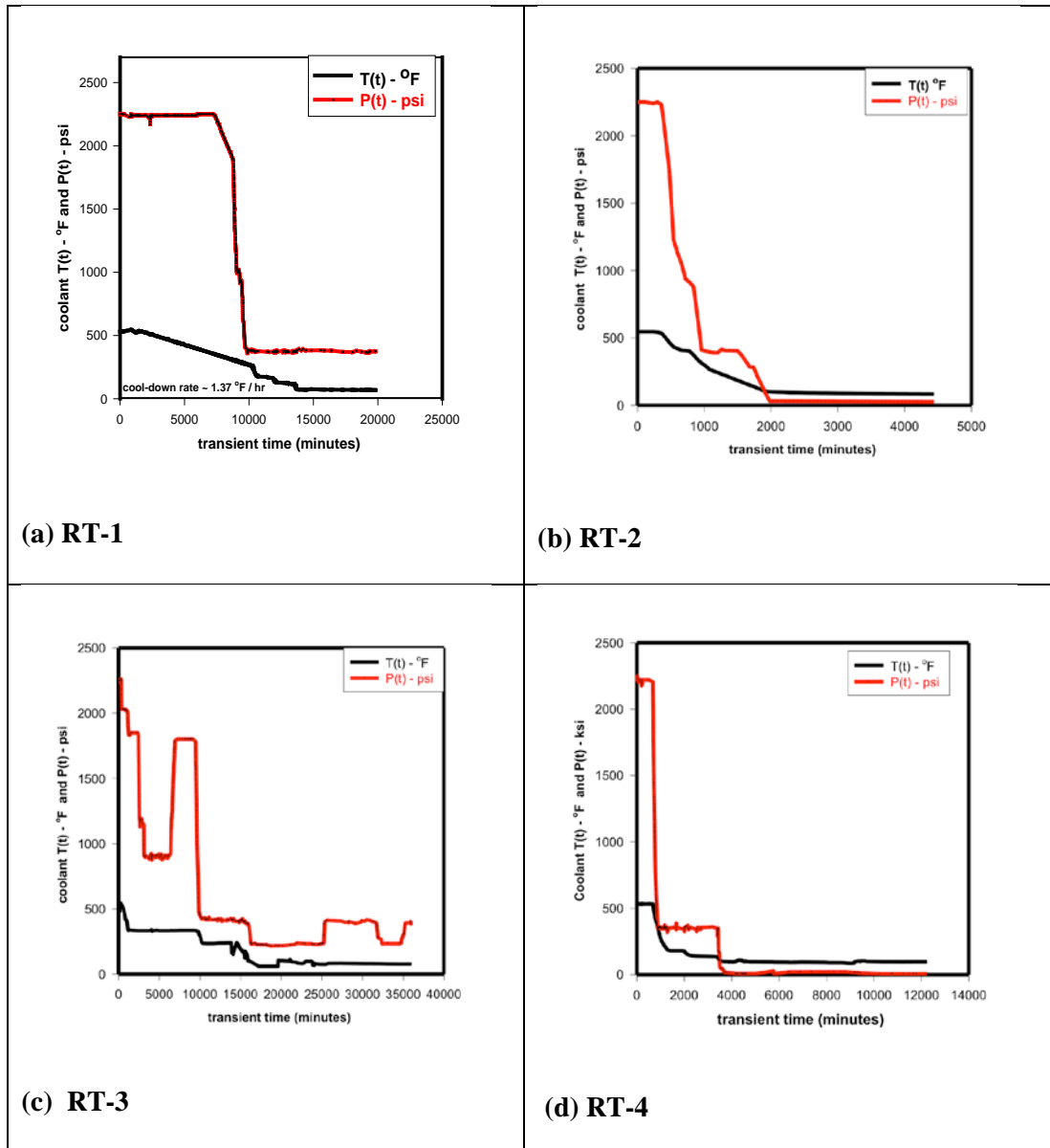


Fig. 3-2 Illustration of pressure (P) and temperature (T) versus time curves for four actual cool-down transients, identified herein as RT-1, RT-2, RT-3 and RT-4.

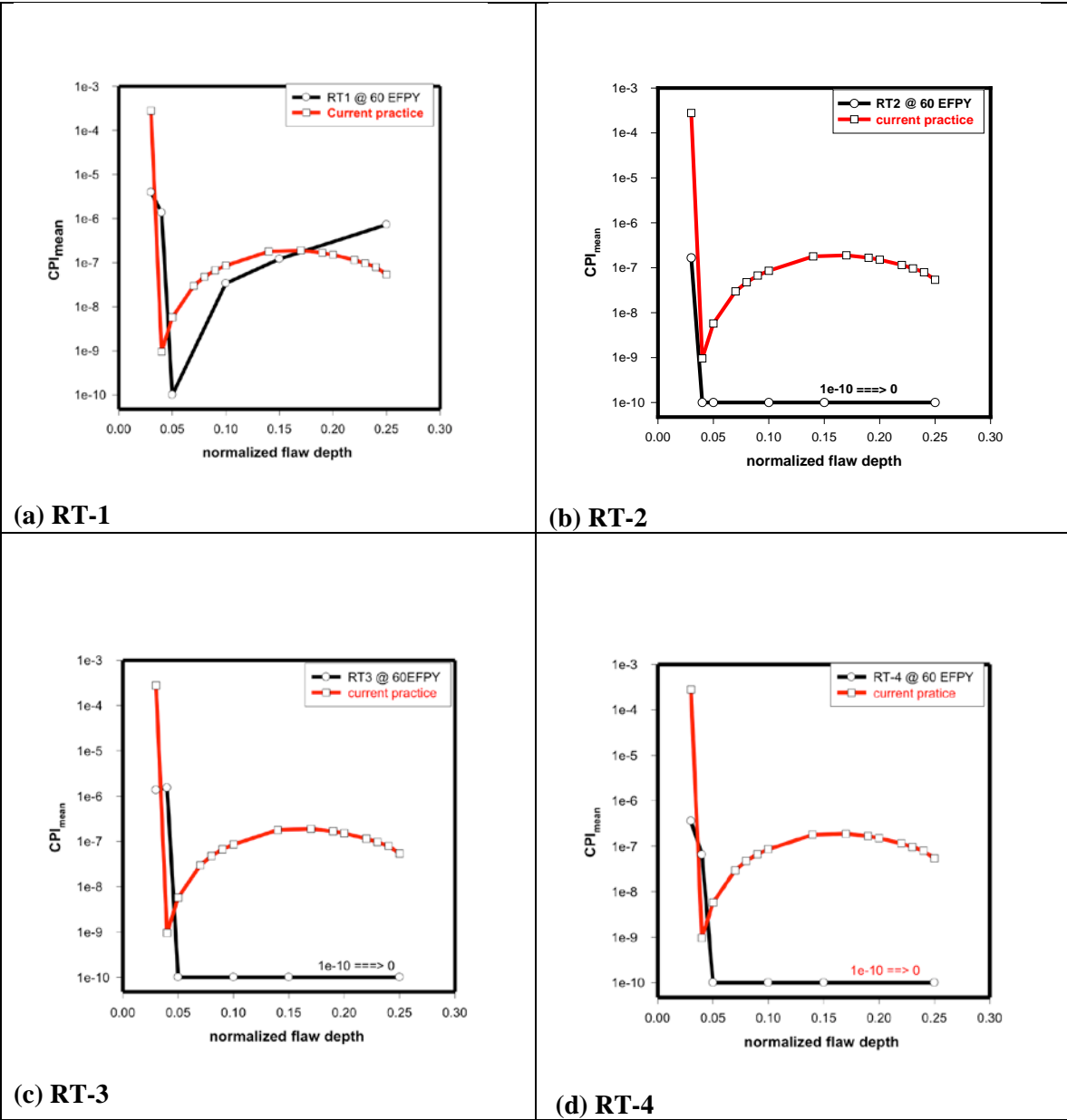


Fig. 3-3 Comparison of CPI values versus normalized crack depth for four actual transients with those computed for the maximum-allowable pressure transient (ASME code procedure) applied to Vessel A at 60 EFPY and 100 °F /hr cool-down rate. Values plotted at 10^{-10} represent $CPI=0$.

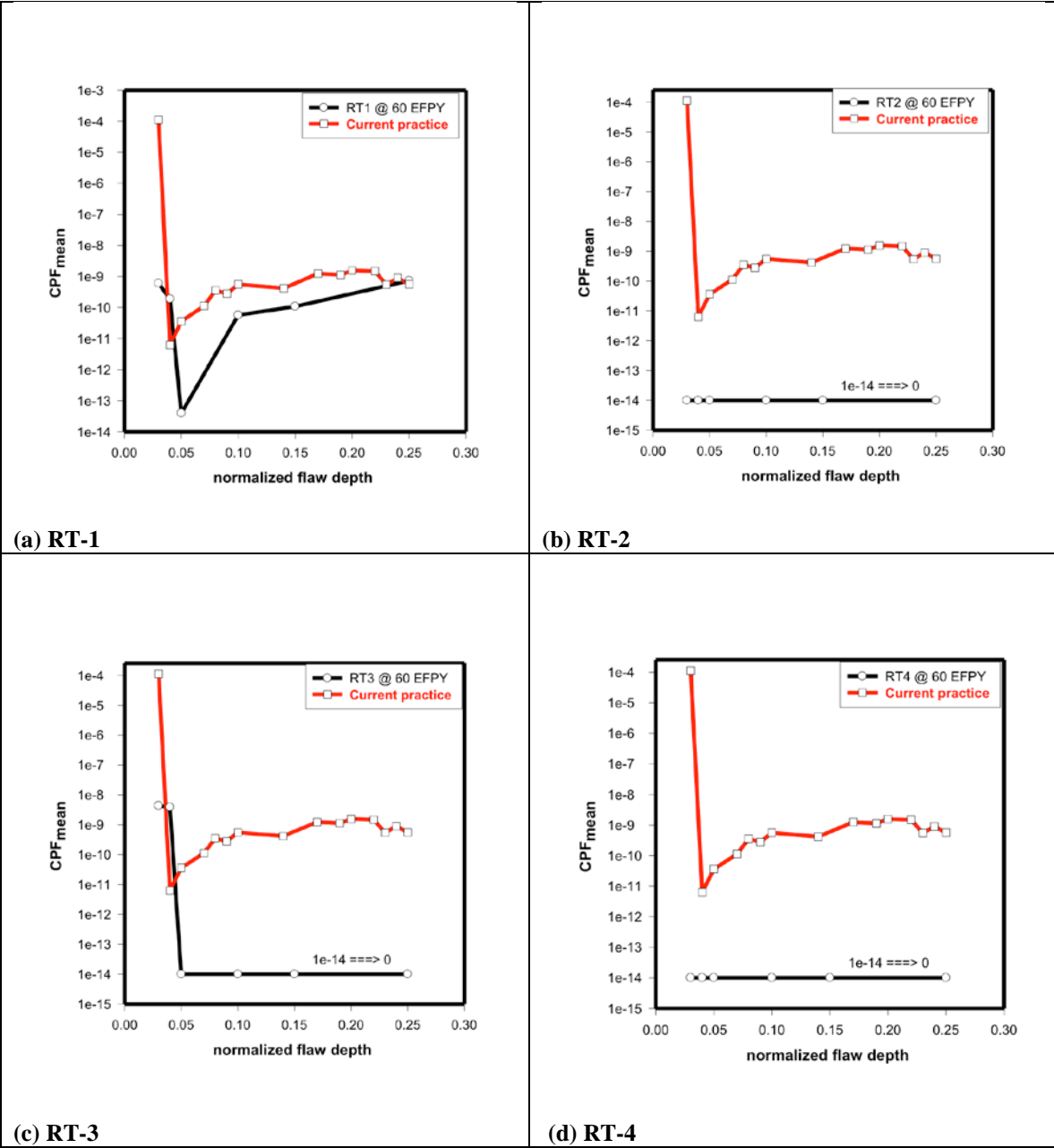


Fig. 3-4 Comparison of *CPF* values versus normalized crack depth for four actual transients with those computed for the maximum-allowable pressure transient (ASME code procedure) applied to Vessel A at 60 EFPY and 100 °F /hr cool-down rate.

To better understand this difference, a study was performed to identify features of PTS transients that influence the probability of initiation for shallow surface-breaking flaws. That study used

- *Vessel A* geometry/properties (see Appendix B),
- selected transients from the nuclear plant incorporating *Vessel A* [4] and
- flaw distributions from ref. [4].

Two groupings of transients, selected from the 30 *Vessel A* transients used in previous PTS studies, were analyzed with the FAVOR code to compare *CPIs* computed for a shallow, surface-breaking flaw ($a = 0.03t$) with those computed for embedded flaws. Those comparisons serve to highlight certain characteristics exhibited by the bulk of PTS transients that tend to de-emphasize the contribution of shallow surface flaws to the computed *CPIs* when compared to embedded flaws. The two groups of transients are identified as follows:

- Group I (*Vessel A* transients 5, 10, 23, and 25) – Fig. 3-5(a) depicts temperature versus time plots of these selected PTS transients that share some characteristics with normal cool-down transients, i.e., they have a relatively slow, steady cool-down rate to lower temperatures.
- Group II (*Vessel A* transients 6, 12, 13, and 18) – Temperature versus time plots of these PTS transients (see Fig. 3-5(b)) do not resemble normal cool-down transients, i.e., they have very fast cool-down rates over a short period of time.

Table 3- 1 presents analysis results that compare *CPIs* for the shallow, ID surface-breaking, circumferential flaw ($a = 0.03t$) with those computed for embedded flaws when subjected to the above two groups of PTS transients. Fig. 3-6 shows the relationship between the cool-down rate for these transients and the ratio of CPI_{embedded} , arising due to embedded flaws, to CPI_{shallow} , arising due to shallow surface breaking flaws. The data in Fig. 3-6 indicate a consistent trend of increasing dominance of surface breaking flaws with reduced cooling rate across these two qualitative groupings. The eight transients depicted in Fig. 3-5 provide a strong indication of the reason why shallow surface breaking flaws have such a significant impact on the PFM results for postulated normal cool-down transients, which have slower cooling rates, and a much more modest impact on the PFM results in previous investigations of PTS, for which the cool-down rates were much faster for the overwhelming majority of the transients studied.

These results demonstrate that peaking of applied K_I factors for shallow surface flaws under transient loading conditions is influenced by the following interactions:

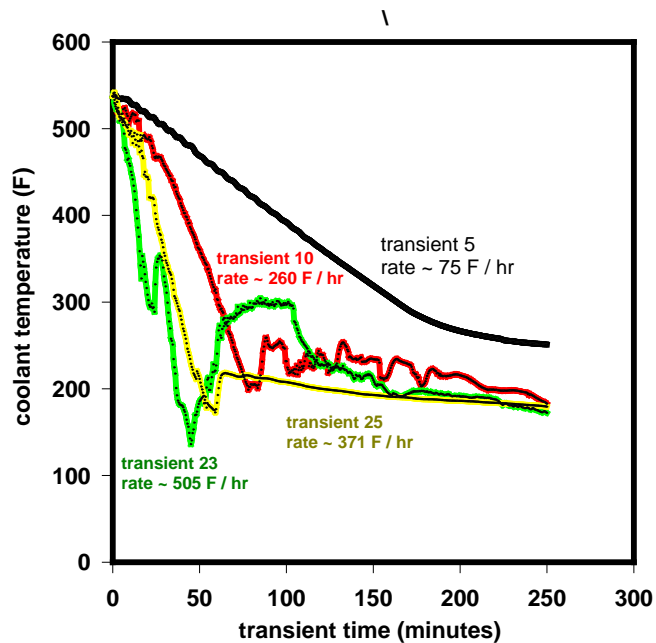
- Slower cool-downs to relatively lower temperatures contribute to thermally controlled transients that exhibit late peaking of the applied K_I . This late peaking (maximum applied K_I) occurs at a transient time when temperature is relatively low and, consequently, fracture toughness is also low at the crack tip. The net effect is to produce a relatively high ratio of applied K_I to fracture toughness at the crack tip, which drives CPI and CPF .
- More rapid cool-downs contribute to pressure-controlled transients that exhibit early peaking of the applied K_I . This early peaking occurs at a transient time when temperature is relatively high and, consequently, fracture toughness is also high at the crack tip. The net effect is to produce a relative lower ratio of applied K_I to fracture toughness at the crack tip, which tends to reduce CPI and CPF .

Generally, the relative value of the ratio of applied K_I to fracture toughness at the crack tip provides a critical influence on CPI and CPF , while the transient cool-down rate is a critical influence on that ratio.

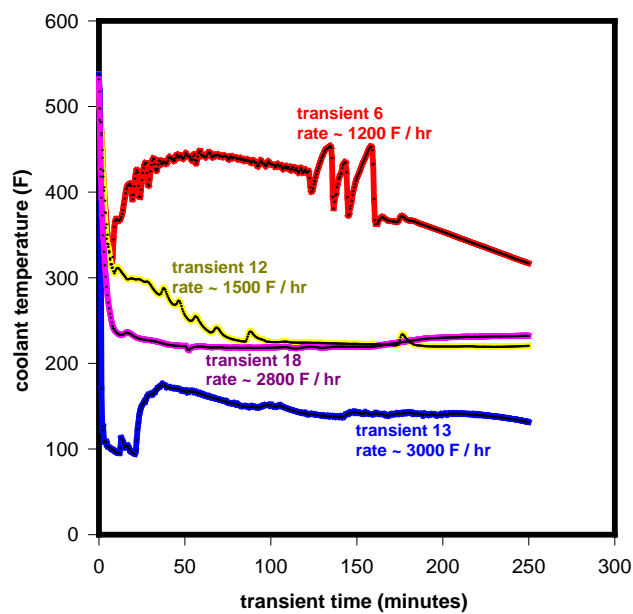
3.3 Summary

Generally, the analysis results presented in this section illustrate the following points:

- in the case of normal operating transients, characteristics of the crack-tip loading generated by the shallow flaw are different from those for the deep flaw such that the shallow flaw can generate a significantly higher probability of brittle fracture, and
- in the case of PTS transients, the *time-rate* of cool-down significantly influences the relative contribution of shallow surface breaking flaws (versus embedded flaws) to the probability of brittle fracture.



(a)



(b)

Fig. 3-5 Two groups of PTS cool-down transients that exhibit different characteristics regarding cool-down rates: (a) Group I - transients have a relatively steady initial cool-down rate that is sustained over a period of time; (b) Group II - transients that have very fast cool-down rates over a short period of time.

Table 3- 1 Comparison of Conditional Probabilities of Initiation (CPI) for Shallow Surface and Embedded Flaws when Subjected to Two Groups of PTS Transients

Transient Number	Average Cooling Rate [°F/hour]	$CPI_{embedded}$ (Embedded Flaws)	$CPI_{shallow}$ (Shallow Surface Flaws)	Ratio: $CPI_{embedded} / CPI_{shallow}$
Group I: PTS transients that resemble normal cool-down transients				
5	75	6.36E-10	2.30E-08	0.028
10	260	2.15E-05	2.29E-05	0.939
23	505	3.47E-04	3.83E-04	0.906
25	371	3.77E-05	7.27E-05	0.519
Group II: PTS transients that do not resemble normal cool-down transients				
6	1200	7.88E-07	4.41E-08	17.9
12	1500	2.60E-06	1.88E-07	13.8
13	3000	5.87E-03	4.32E-04	13.6
18	2800	2.28E-04	6.85E-06	33.3

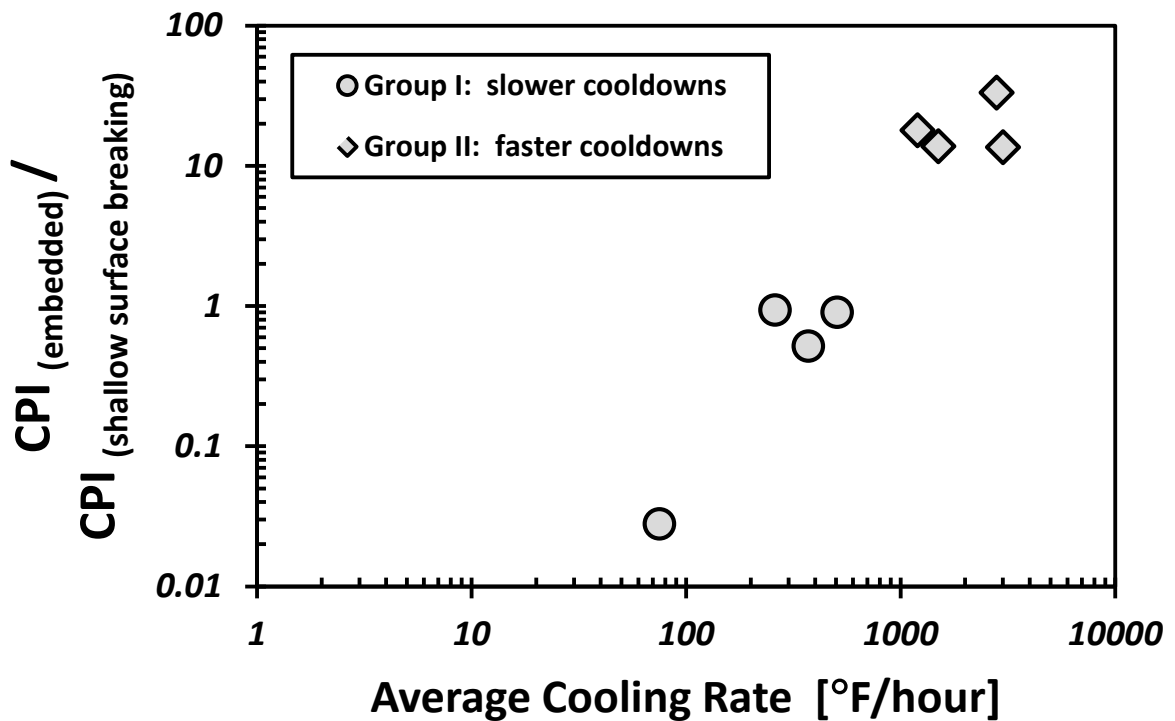


Fig. 3-6 Plot of the data from Table 3- 1 illustrating the effect of cooling rate on the population of flaws that dominate the PFM results

4. Summary and Conclusions

Note: The work documented herein is part of an on-going effort that is sponsored by the NRC at ORNL and does not describe a final product or a regulatory position. This effort aims to better understand and quantify the risk of crack initiation and reactor vessel fracture posed by normal operating loads (that is: heat up, cool down, and leak tests). These results have been generated using the best models and technical understanding available at this time consistent with the funded scope and timeframes of the project. Nevertheless, readers should recognize that certain aspects of the models that have been implemented in the PFM computer code FAVOR used to produce the results reported herein remain the topic of continued study and refinement. These concern mostly the model of the RPV cladding and flaws that may lie in or near the cladding; see Chapter 5 for details. Future improvements to these models may alter the results presented herein. Such changes, if they occur, will be communicated by (a) revisions of this report, and (b) the issuance of other related reports.

Reactor pressure vessel geometries subjected to postulated and actual operational cool-down transients were analyzed using the PFM code FAVOR. The objective of those studies was to determine trends for *CPI* and *CPF* as a function of initial flaw depth for postulated ID surface-breaking flaws. The analyses produced two conclusions regarding probability of vessel failure:

- (1) shallow surface-breaking flaws dominate the RPV failure probability as quantified by the *CPI* and *CPF* probabilistic metrics;
- (2) shallow surface-breaking flaws exhibit *CPI* and *CPF* values that exceed those for the $\frac{1}{4} t$ flaw referenced in the ASME Code, Section XI, Appendix G.

These outcomes were observed for postulated transients that follow the *P-T* curves defined using both the ASME code procedures and the EPRI-MRP-250 risk-informed methodology.

Results from the postulated *P-T* transient analyses demonstrate that *CPI* trends for circumferential, ID surface-breaking flaws vary non-monotonically with flaw depth, reaching a global maximum for very shallow flaws that just penetrate the base material. For postulated *P-T* transients, the variation with time of the applied K_I exhibits two local maxima, the first peak occurring earlier in the postulated transient at the end of pressure hold time, and the second peak at the end of cool-down when the coolant temperature asymptotically approaches ambient conditions. The non-monotonic variation of *CPI* with depth occurs because either the first or second peak in the applied K_I time history may control the *CPI*, depending upon which peak provides the maximum applied K_I . Results for shallower flaws are more likely to be controlled by maximum applied K_I occurring at the late second peak, when temperature and, therefore, fracture toughness are relatively lower. This “shallow-flaw” effect is due entirely to the additional crack

driving force generated for shallower flaws by the CTE mismatch between cladding and base material. This CTE contribution diminishes rapidly as the flaw depth increases.

As a consequence of the above findings, further study was undertaken to check the accuracy and adequacy of the ID surface-breaking flaw model implemented in the FAVOR computer code. A literature survey was conducted to identify information concerning the physical attributes and the incidence of shallow flaws found in the stainless-steel cladding of RPVs. Assessment of the FAVOR shallow-flaw model confirmed that it incorporates features critical to modeling observed shallow surface flaws subjected to service loading conditions; those features include adequate/accurate representations of (1) vessel geometry/stress loading and (2) physical attributes and incidences of observed flaws. Specific characteristics of that model discussed herein include the following:

- realistic simulation of vessel geometry and stress fields in the beltline region of a RPV subjected to thermal-hydraulic transients;
- utilization of stochastically-generated flaw input files that account for uncertainties in parameters of flaw distribution functions; those flaw distribution functions are derived from multiple sources that include destructive and non-destructive RPV materials examinations, flaw simulation studies utilizing the PRODIGAL code and NRC expert judgment elicitation on vessel flaws;
- implementation of a shallow-flaw analysis methodology that, when applied to planar and sharp defects, should provide best-estimate values of *CPI* in PFM analyses; applications to volumetric (i.e., blunted) defects would most likely produce conservative estimates;
- confirmation of validity of the LEFM assumption by application of advanced fracture mechanics techniques, including consideration of EPFM and constraint effects.

Detailed analyses were conducted using the FAVOR code to assess the impact of various loading conditions on shallow surface-breaking flaws in RPVs: (1) postulated normal cool-downs following the maximum allowable pressure curve, including ASME code procedure and EPRI-MRP-250 risk-informed approaches; (2) actual normal cool-downs experienced by several plants; and (3) postulated accident cool-downs such as PTS events. Conclusions drawn from those analyses include the following:

- Results for actual P-T transients have *CPI*/*CPF* values orders of magnitude lower than those calculated for many postulated cool-down transients that follow the maximum allowed pressure (for both ASME Code procedure and EPRI risk-informed method).

Nevertheless, the *CPI/CPF trends* with surface flaw depth for both transient types are consistent; in both cases, shallow surface-breaking flaws have a higher probability of brittle fracture than do deeper flaws.

- For selected PTS transients, analysis results showed that fracture probabilities for shallow surface-breaking flaws are comparable to or greater than those for embedded flaws; the latter result is strongly influenced by those transients exhibiting a cool-down history sustained over a period of time to relatively lower temperatures; however, the bulk of PTS transients do not exhibit such a sustained cool-down history. For four of the PTS transients analyzed herein with a rapid cool down, embedded flaws had *CPIs* that were more than one order of magnitude greater than those for shallow surface-breaking flaws.

More generally, the analysis results provided herein imply that peaking of applied K_I factors for surface flaws under postulated transient loading conditions is influenced by the following interactions:

- Shallow flaws and/or slower cool-downs to relatively lower temperatures contribute to thermally-controlled transients that exhibit late peaking of the applied K_I .
- Deep flaws and/or more rapid cool-downs contribute to pressure-controlled transients that exhibit early peaking of the applied K_I .

A shallow surface flaw just penetrating the cladding is shown herein to exhibit a *CPI* value exceeding the ASME/Appendix G $\frac{1}{4} t$ flaw value by several orders of magnitude. Use of the (highly improbable) $\frac{1}{4} t$ flaw in the ASME Code could arguably be interpreted as a conservatism that compensates for omissions/uncertainties in the calculation of P-T limits; however, one factor omitted in the ASME methodology is the existence of cladding on the inner surface of the RPV. This report makes clear that the enhanced size of the $\frac{1}{4} t$ flaw does not compensate for ignoring the added driving force to fracture produced by the clad layer that acts on the shallow surface flaw.

Finally, the NRC staff has identified several specific issues concerning the FAVOR shallow flaw methodology that may warrant further study to determine whether refinement of those features of the model could have a material effect on the major conclusions of this report. In the following section, those primary issues are briefly summarized for consideration by the NRC as future research topics.

5. Potential Future Research

This report has shown that the shallow ($a/t = 0.03$), circumferential, ID, surface-breaking flaw dominates the RPV failure probability for a majority of postulated normal cool-downs that follow the maximum allowed pressure derived using both ASME Section XI code procedure and the EPRI-MRP-250 risk-informed method. In particular, the shallow flaw exhibits *CPI* values exceeding (by orders of magnitude) those for the $\frac{1}{4} t$ flaw referenced in ASME Section XI. The latter results have motivated further analyses to better understand the range of factors influencing those results. Following review of a draft of this report, the NRC staff identified several specific issues concerning the FAVOR shallow flaw methodology that warrant further study to determine whether refinement of those features of the model could have a material effect on the major conclusions. The main issues, which are reflected in a recent NRR User Need Request, are briefly summarized below for consideration by the NRC as future research topics.

1. The flaw analysis methodology implemented in the FAVOR code assumes a planar and sharp defect that should provide best-estimate values of *CPI* in PFM analyses; applications of that methodology to volumetric (i.e., blunted) defects would most likely produce conservative estimates. Further study of the impact of corrosion mechanisms on shallow cracks, including any changes to morphology, depth, and driving force of those flaws over time, may determine whether accounting for those mechanisms would substantially influence the FAVOR analysis results for shallow flaws and, thus, the major conclusions of this report.
2. A narrow HAZ region exists within the base material at the clad/base interface of the RPV wall as a result of the clad application process. The shallow flaw analyses performed herein using both the FAVOR and ABAQUS codes do not explicitly model that clad HAZ within the base material or the associated mechanical and fracture toughness properties of the HAZ. More detailed research would be needed to clarify whether the dimensions of the clad HAZ and/or differences in mechanical/fracture properties within the HAZ region could alter predictions of crack initiation and arrest processes sufficiently to impact conclusions of this report.
3. An on-going collaborative effort between ORNL and NRC/RES is assessing the impact of applying EPFM-based corrections to LEFM values of applied K_I computed by the

FAVOR code in flaw assessments. Further work is recommended to determine if plasticity-correction of applied K_I values, taken together with other factors identified herein, could have a beneficial impact on the FAVOR predictions described herein for shallow surface flaws.

4. The RPV is subjected to periodic, normal, operational cool-down transients (for example, such as those depicted in Fig. 3-2) that occur throughout its service life. A study that considers the possible influence of *load history effects* that may arise from periodic loading of the vessel could help quantify how the evaluation of periodic, normal cool-down transients should be different from the evaluation of unexpected PTS transients, and how these differences might change the results reported herein.
5. Current and previous versions of FAVOR adopted a clad/base stress-free temperature (SFT) of 488 °F, from which differential thermal expansion (DTE) stresses are calculated for each time step of the loading transient (see Appendix E for a detailed description of that implementation). An alternative approach for incorporating clad residual stresses moves away from the SFT method and allows the user to *prescribe* a clad residual stress field and corresponding temperature for that field. One clad residual stress field that could be used as input to this alternative approach is the one measured in the ORNL PVRUF vessel at room temperature [33].

6. References

1. P.T. Williams, T.L. Dickson, and S. Yin, *Fracture Analysis of Vessels – Oak Ridge FAVOR, v12.1, Computer Code: Theory and Implementation of Algorithms, Methods, and Correlations*, ORNL/TM-2012/567, Oak Ridge National Laboratory, Oak Ridge, TN, November 2012.
2. *ASME Boiler and Pressure Vessel Code, Section XI, Appendix G*, “Fracture Toughness Criteria for Protection Against Failure”, New York, 2004.
3. M.T. EricksonKirk and T.L. Dickson, *Recommended Screening Limits for Pressurized Thermal Shock*, NUREG 1874, U.S. Nuclear Regulatory Commission, <http://www.nrc.gov/reading-rm/doc-collections/nuregs/staff/sr1874/>, March 2010.
4. T.L. Dickson, et al., “Electronic Archive for the Results of Pressurized Thermal Shock Analyses for Beaver Valley, Oconee, and Palisades Reactor Pressure Vessels Generated with the 06.1 Version of FAVOR,” ORNL/NRC/LTR-07/04, Oak Ridge National Laboratory, April 2007.
5. EPRI MRP-250 – RI Appendix G: Risk-Informed Method to Determine ASME Section XI Appendix G Limits for Ferritic Reactor Pressure Vessels - An Optional Approach Proposed for ASME Section XI Appendix G (MRP-250) and (BWRVIP-215NP).
6. M.T. Kirk, “Inclusion of Warm Pre-stressing Effects in Probabilistic Fracture Mechanics Calculations Performed to Assess the Risk of RPV Failure Produced by Pressurized Thermal Shock Events: An Opinion,” presented at the *NATO Advanced Research Workshop – Scientific Fundamentals for the Life Time Extension of Reactor Pressure Vessels*, Kiev, Ukraine, April 22–25, 2002.
7. ABAQUS Finite Element Software, Version 6.11, Dassault Systems Simulia Corp., 2011.
8. K. Wallin, “Quantifying Tstress Controlled Constraint by the Master Curve Transition Temperature T_0 ,” *Engineering Fracture Mechanics*, 68, 2001, pp. 303-328.
9. T. L. Dickson, M. T. Kirk, and E. Focht, “Mechanistic Insights into Risk-informed Revision of ASME Section XI-Appendix G,” Paper number PVP2011-57009, *Proceedings of the 2011 ASME Pressure Vessels and Piping Division Conference*, July 17-21, 2011, Baltimore, Maryland.
10. T.J. Kim and R. Auluck, *Safety Evaluation Report Related to the License Renewal of the Dresden Nuclear Power Station, Units 2 and 3 and Quad Cities Nuclear Power Station, Units 1 and 2*, USNRC, NUREG-1796, 2004.
11. I. Kondo, H. Nakajima, and R. Nagasaki, “Metallographic Investigation of the Cladding Failure in the Pressure Vessel of a BWR,” *Nuclear Engineering and Design*, 16 (1971) 205-202.
12. F.A. Simonen, S.R. Doctor, G.J. Schuster, and P.G. Heasler, *A Generalized Procedure for Generating Flaw Related Inputs for the FAVOR Code*, NUREG/CR-6817, Rev. 1, U.S. Nuclear Regulatory Commission, October 2003, available in ADAMS under Accession #ML051790410.

13. G.J. Schuster, S.R. Doctor, S.L. Crawford, and A.F. Pardini. *Characterization of Flaws in U.S. Reactor Pressure Vessels: Density and Distribution of Flaw Indications in the Shoreham Vessel*, NUREG/CR-6471, Vol. 3, U.S. Nuclear Regulatory Commission, Washington, DC, 1999.
14. F. A. Simonen, S. R. Doctor, G. J. Schuster, D. A. Jackson, and L. Abramson, "Flaws in Vessel Cladding and Their Potential Contributions to Vessel Failure Probabilities," *ASME PVP-Vol. 427, Service Experience, Fabrication, Residual Stresses and Performance*, pp. 21-32, 2001.
15. F. A. Simonen, G. J. Schuster, S. R. Doctor, and T. L. Dickson, "Distributions of Fabrication Flaws in Reactor Pressure Vessels for Structural Integrity Evaluations," *Fatigue, Fracture, and Damage Analysis - 2002*, ASME PVP-Vol. 433-2, pp. 133-143.
16. T. G. Theofanous, S. Angelini, H. Yan, Universal Treatment of Plumes and Stresses for Pressurized Thermal Shock Evaluations, NUREG/CR-5854/R4, University of California Santa Barbara, June 1992.
17. B. R. Bass, T. L. Dickson, P. T. Williams, A. V. Phan, and K. L. Kruse, "Verification and Validation of FAVOR Code – Deterministic Load Variables," ORNL/NRC/LTR-04/11, March, 2004, Oak Ridge National Lab, Oak Ridge, TN.
18. S. Yin, T. L. Dickson, P. T. Williams, and B. R. Bass, "Verification of New Capabilities of Deterministic Load Module of FAVOR 09.1", Paper number PVP2010-25439, *Proceedings of 2010 ASME Pressure Vessels and Piping Division Conference* July 18-22, 2010, Bellevue, Washington.
19. T. L. Dickson, et al., "Evaluations of Margins in the ASME Rules for Defining the P-T Curve for a RPV, *Proceedings of the 1999 ASME Pressure Vessel and Piping Division Conference*, July 1999, Boston, MA.
20. G. J. Schuster, S. R. Doctor, and P. G. Heasler, *Characterization of Flaws in U.S. Reactor Pressure Vessels: Density and Distribution of Flaw Indications in PVRUF*, NUREG/CR-6471, Vol. 1, U.S. Nuclear Regulatory Commission, Washington, DC, 1998.
21. G.J. Schuster, S. R. Doctor, S. L. Crawford, and A. F. Pardini, *Characterization of Flaws in U.S. Reactor Pressure Vessels: Validation of Flaw Density and Distribution in the Weld Metal of the PVRUF Vessel*, NUREG/CR-6471, Vol. 2, U.S. Nuclear Regulatory Commission, Washington, DC, 2000.
22. O. J. V. Chapman and F.A. Simonen, *RR-PRODIGAL - A Model for Estimating the Probabilities of Defects in Reactor Pressure Vessel Welds*, NUREG/CR-5505, U.S. Nuclear Regulatory Commission, Washington, DC, 1998.
23. D.A. Jackson and L. Abramson, *Report on the Preliminary Results of the Expert Judgment Process for the Development of a Methodology for a Generalized Flaw Size and Density Distribution for Domestic Reactor Pressure Vessels*, MEB-00-01, PRAB-00-01, U.S. Nuclear Regulatory Commission, Washington, DC, 2000.
24. R. D. Cheverton, J. W. Bryson, D. J. Alexander, and T. Slot, "Thermal shock experiments with flawed clad cylinders," *Nuclear Engineering and Design* 124 (1990) 109-119
25. M. Wagenhofer, *Modeling the Transition Region Fracture Behavior of Ferritic Steels*, Ph.D. dissertation, University of Maryland, 2002.
26. M.L. Williams, "On the Stress Distribution at the Base of a Stationary Crack," *Journal of Applied Mechanics*, Vol. 24, 1957, pp.109-114.

27. T. Wilt, G. Adams and F. Simonen, "Verification and Validation of the FAVOR Version 09.1 Code," Center for Nuclear Waste Regulatory Analyses, San Antonio, Texas, October 2011.
28. NRC 10 CFR 50.61a *Alternate fracture toughness requirements for protection against pressurized thermal shock events.*
29. Dickson, T. L., and EricksonKirk, M. T., "Assessment of Large-Scale Pressurized Thermal Shock Experiments Using the FAVOR Fracture Mechanics Code," *2004 ASME Pressure Vessel and Piping Conference*, ASME PVP volume 481, RPV Integrity and Fracture Mechanics, pp 31–37, San Diego, CA, July 2004.
30. R. H. Bryan et al., "Pressurized Thermal Shock Test of 6-in.-Thick Pressure Vessels: PTSE-1: Investigation of Warm Prestressing and Upper Shelf Arrest," NUREG/CR-4106 (ORNL-6135), Oak Ridge National Lab., Oak Ridge, TN (April 1985).
31. M. EricksonKirk, et al., *Technical Basis for Revision of the Pressurized Thermal Shock (PTS) Screening Limit in the PTS Rule (10 CFR 50.61) – Summary Report*, NUREG-1806, Vol. 1, U.S. Nuclear Regulatory Commission, August, 2007.
32. M. EricksonKirk, et al., *Technical Basis for Revision of the Pressurized Thermal Shock (PTS) Screening Limit in the PTS Rule (10 CFR 50.61) – Appendices*, NUREG-1806, Vol. 2, U.S. Nuclear Regulatory Commission, August, 2007.
33. Joshua Kusnick et al, *Effect of cladding residual stress modeling technique on shallow flaw stress intensity factor in a reactor pressure vessel*, Proceedings of the ASME 2015 Pressure Vessels and Piping Conference, PVP2015-45086, July 19-23, 2015, Boston, Massachusetts, USA.

APPENDIX A: PROCEDURE FOR COMPUTATION OF CONDITIONAL PROBABILITY OF INITIATION FOR SURFACE FLAWS SUBJECTED TO POSTULATED COOL-DOWN TRANSIENTS.

This Appendix describes procedures used in the FAVOR code [A1] for computation of the conditional probability of initiation (*CPI*) for each surface flaw analyzed. The variation of these *CPI* values with surface flaw depth appears in Fig. A-1. The loading conditions for each surface flaw are depicted in Fig. A-2. For additional details concerning terms and references used in the procedure described herein, the reader is referred to the FAVOR Theory manual [A1].

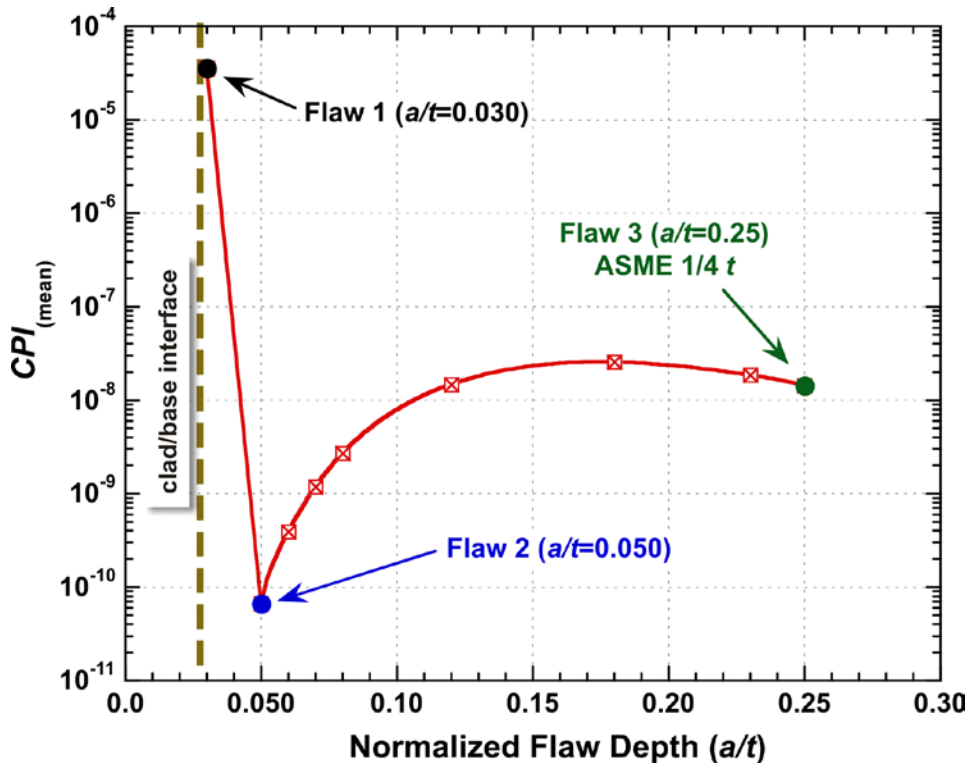


Fig. A-1 *CPI* for circumferentially-oriented inner surface flaws exhibiting non-monotonic behavior with flaw depth for Vessel A¹⁶ subject to the pressure and temperature limits determined from ASME code procedure and shown in Fig. A-2; the P-T limits are based on 60 EFPY and a cool-down rate of 50 °F/hr.

In Fig. A-1, the CPI_{mean} (mean *CPI*) calculated for each flaw depth was the result of a PFM analysis performed for that specific flaw depth. In each PFM analysis,

¹⁶ Vessel A is defined in Appendix B.

1. Each RPV¹⁷ in the Monte Carlo analysis is modeled as having two flaws of the specified depth based on flaw densities provided by VFLAW [A2].
2. The aspect ratio for each flaw was determined by sampling from a distribution (also provided by VFLAW). The distribution for aspect ratios is given in Table A-1.

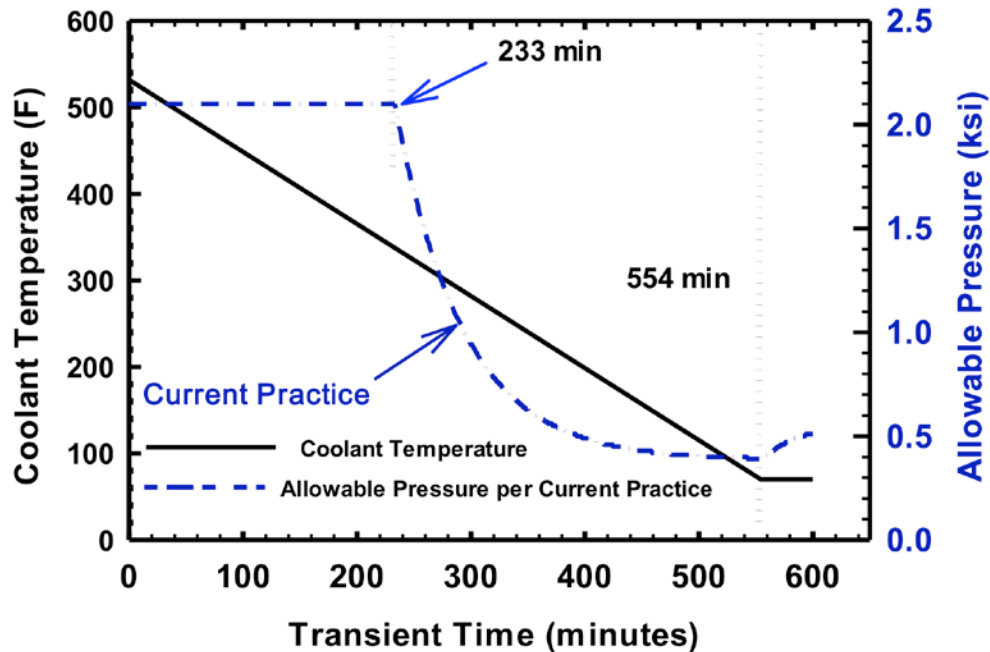


Fig. A-2 Prescribed pressure-temperature limits for normal cool-down transients determined using standard ASME code procedure. Pressure-temperature limits are shown for *Vessel A* at 60 EFPY with a cool-down rate of 50 °F/hr.

Table A-1 Distribution of surface flaw aspect ratios used in analyses

Surface flaw aspect ratio	Distribution (percent)
2:1	67.45
6:1	20.77
10:1	3.96
Infinite	7.82

¹⁷ Analyses of 100,000 RPVs is typical for a PFM application of the FAVOR code.

The aspect ratios in Table A-1 correspond to those discrete values for which the FAVOR code has SIFICs, and thus can calculate values of applied K_I , and are intended to span the range of surface-breaking flaw geometries possibly encountered in reactor service.

3. Each flaw was statistically placed into a particular RPV sub-region based on the fraction of flaws predicted to reside in that sub-region; that sub-region has its own mean value for chemistry, neutron fluence, un-irradiated RT_{NDT} , etc.

It should be noted that 1.7% of the postulated surface breaking flaws are predicted to reside in welded regions. The $K_I(t)$ for these flaws includes the effects of the through-wall weld residual stress, whereas the remaining 98.3% of the postulated surface breaking flaws are predicted to reside in plate regions, for which $K_I(t)$ would not include the through-wall weld residual stress. This allocation of surface-breaking flaws is based on the percentages of inside surface areas that are welded or plate regions.

In general, the level of discretization of the RPV beltline region into sub-regions is determined by the neutron fluence map. For the analyses used to generate the results in Fig. A-1, the RPV was divided into over 60,000 sub-regions. In addition to having its own neutron fluence and chemistry, each of these sub-regions has its own postulated number of flaws, based on the geometry and flaw densities (and, consequently, some fraction of the total postulated number of flaws). It is this fractionalization that is used to place each individual flaw into a particular sub-region such that, at the end of the Monte Carlo analysis, the flaws have been placed into the various sub-regions in the proportions described by VFLAW [A2].

4. The values of chemistry and fluence are sampled and the fluence is attenuated to the crack tip such that a value of $RT_{NDT}(EFPY, x)$ can be calculated at the crack tip. Figure A-3 below illustrates the statistical distribution of crack tip RT_{NDT} from the PFM analysis of the shallow flaw at 60 EFPY (sample size is 100,000 RPVs, each with 2 flaws, for total of 200,000 flaws).

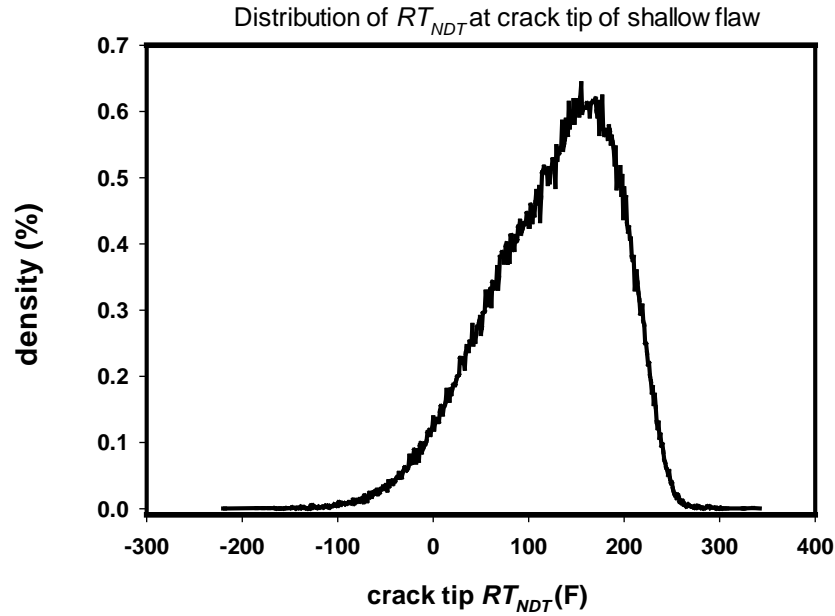


Fig. A-3 Example of the distribution of RT_{NDT} at crack tip of shallow flaw in PFM analyses

5. Next, an evaluation is performed at each discrete transient time step to determine if the applied $K_I(t)$ of the flaw exceeds the minimum value of the FAVOR K_{Ic} model. That minimum value is denoted here as $K_{Ic \text{ Weibull-}a}$ and designated as the Weibull-a curve, where “a” is the location parameter of the three-parameter Weibull statistical distribution used in FAVOR to model K_{Ic} for the base metal. The Weibull-a curve has the following functional dependence:

$$K_{Ic \text{ Weibull-}a} = f\{T(t) - RT_{NDT}(EFPY, x)\}$$

Depending on that placement and on the aspect ratio, there are eight possibilities for $K_I(t)$, i.e., one each for the four possible aspect ratios in weld regions and likewise for the plate regions.

If two criteria are realized, namely,

- $K_I(t)$ exceeds $K_{Ic \text{ Weibull-}a}$ and
- $K_I(t)$ exceeds the value of $K_I(t)$ at all previous times in the transient (as required by warm-prestress model)

then a non-zero value of instantaneous $cpi(t)$ is calculated ($0 < cpi(t) \leq 1.0$) from

$$cpi(t) = 1.0 - \exp \left\{ - \left(\frac{K_I(t) - K_{Ic \text{ Weibull-}a}(t)}{b} \right)^c \right\}$$

where

$$K_{Ic \text{ Weibull-}a}(t) = 19.35 + 8.335 \times \exp(0.02254 \times (T(t,x) - RT_{NDT}(EFPY, x)))$$

$$b \text{ (Weibull "b" parameter)} = 15.61 + 50.132 \times \exp(0.008 \times (T(t, x) - RT_{NDT}(EFPY, x)))$$

$$c \text{ (Weibull "c" parameter)} = 4.0$$

Note that x is the distance of the crack tip measured from the RPV wetted inner surface.

6. *CPI* for that flaw is the maximum value of *cpi*(t) calculated over all time steps
7. If more than one flaw in an RPV has *CPI* > 0, then the *CPI* for that RPV is calculated (in this case, for two flaws) as

$$CPI = 1 - (1 - CPI_1)(1 - CPI_2)$$

8. The mean *CPI* value is the sum of the values of *CPI* (i.e., summed over the total number of simulated RPVs) divided by the total number of simulated RPVs.

As previously discussed, each PFM analysis was performed for a specific flaw depth. There was no weighting to account for the fact that a shallower flaw is more likely to exist than a deeper flaw.

It should be noted that the flaw density and distribution for the various aspect ratios was predicted previously by the VFLAW computer code for the Oconee RPV during the PTS re-evaluation.

Example numerical problem

For clarity, a numerical example (taken from the PFM analysis for the shallow 0.03t flaw included in the plot of *CPI* versus flaw depth shown Fig. A-1) is illustrated for a single RPV in the Monte Carlo analysis. This particular RPV, taken from the Monte Carlo analysis, was selected for this illustration because both flaws were predicted to have a *CPI* > 0. Also, one flaw is in a weld region and the other in a plate region.

Table A-2 illustrates the computation of *CPI* for the first flaw (Flaw #1) which has an aspect ratio of 6:1 and resides in weld material; therefore, $K_I(t)$ includes through-wall weld residual stress.

The RT_{NDT} at the crack tip was 338.35 °F which, as can be seen in Fig. A-3, is on the very tail of the distribution of RT_{NDT} values. Applied $K_I(t)$ reaches its maximum value at $t = 554$ minutes, i.e. the previously discussed “2nd peak”, which corresponds to the time at which the coolant temperature reaches the assumed ambient temperature of 70 °F. The $CPI_1 = 1.12E-2$ for this flaw corresponds to the maximum value of instantaneous *cpi*(t).

Similarly, Table A-3 illustrates the computation of CPI for the second flaw (Flaw #2) that also had an aspect ratio of 6:1 but resided in plate material; therefore, $K_I(t)$ does not include through-wall weld residual stress. The RT_{NDT} at the crack tip was 184.88 °F. Again, $K_I(t)$ reaches its maximum value at $t = 554$ minutes. The $CPI_2 = 3.17E-7$ for this flaw corresponds to the maximum value of instantaneous $cpi(t)$.

The CPI for the RPV is calculated as

$$CPI = 1 - (1 - CPI_1)(1 - CPI_2) = 1 - (1 - 1.12E-2) (1 - 3.17E-7) = \underline{\underline{1.12E-2}}$$

Table A-4 specifies the allocation of CPI to weld / plate regions and aspect ratio for the case that includes through-wall weld residual stress in the model.

Effects of Weld Residual Stresses

Figure A-4 illustrates the results of PFM analyses with and without inclusion of through-wall weld residual stress for the flaws placed in welds. Table A-5 provides a listing of the analysis results plotted in Fig. A-4.

Effects of Surface Flaw Aspect Ratio

Figure A-5 illustrates $K_I(t)$ versus time curves for the shallow flaw depth $a/t = 0.03$ for aspect ratios of 2:1, 6:1, 10:1, and infinity. Figure A-5 also illustrates the $K_{Ic \text{ Weibull-}a}$ fracture toughness curve versus time for a crack tip $RT_{NDT} = 338.35$ °F, which corresponds to Flaw #1 (in weld material) given in the numerical example discussed above.

The $K_I(t)$ for the aspect ratio of 10:1 at time $t = 554$ minutes was 28.12 ksi $\sqrt{\text{in}}$, which increases the CPI for this flaw (and RPV) from 1.12E-02 (for the aspect ratio of 6:1) to 2.58E-02. Similarly, the $K_I(t)$ for the aspect ratio of infinity at time $t = 554$ minutes was 29.84 ksi $\sqrt{\text{in}}$, which increases the CPI for this flaw (and RPV) to 5.23E-02.

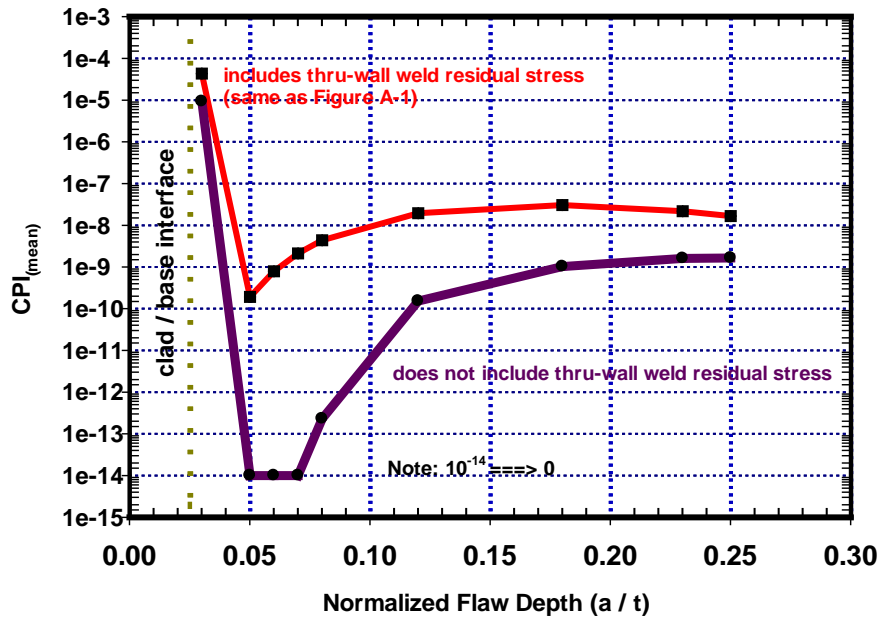


Fig. A-4 Results of PFM analyses with and without inclusion of through-wall weld residual stress

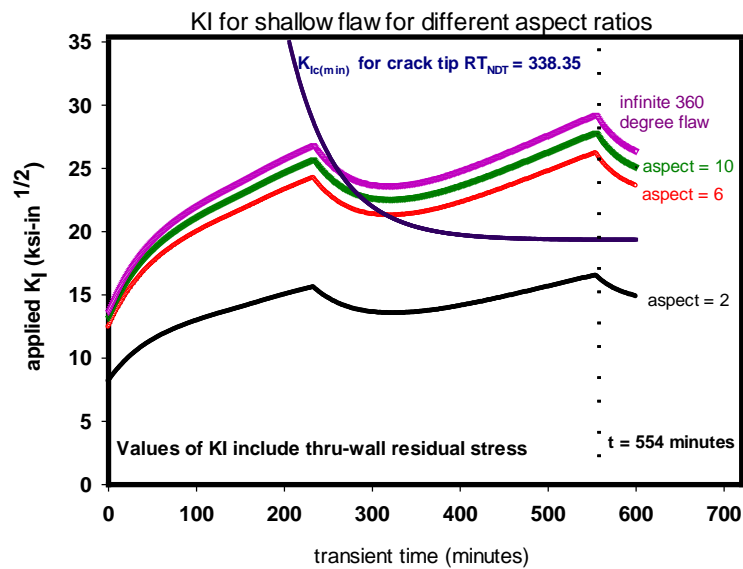


Fig. A-5 Interaction of K_I versus time for shallow flaws of different aspect ratios with $K_{IcWeibull-a}$ versus time for crack tip $RT_{NDT} = 338.35$ °F

Table A-2 Flaw number 1: $a/t = 0.03t$ flaw, aspect ratio of 6:1, located in weld material, $K_I(t)$ includes through-wall weld residual stress

Time (min)	T(t) (°F)	$K_I(t)$ ksi \sqrt{in}	RT _{NDT} (°F)	K_{Ic} Weibull-a	W(b)	cpi(t)
545	83.26	26.21	338.35	19.38	22.12	9.06E-03
546	82.43	26.24	338.35	19.38	22.08	9.29E-03
547	81.60	26.27	338.35	19.38	22.04	9.53E-03
548	80.77	26.30	338.35	19.38	22.00	9.78E-03
549	79.94	26.32	338.35	19.37	21.95	1.00E-02
550	79.11	26.35	338.35	19.37	21.91	1.02E-02
551	78.28	26.38	338.35	19.37	21.87	1.05E-02
552	77.45	26.41	338.35	19.37	21.83	1.07E-02
553	76.62	26.43	338.35	19.37	21.79	1.09E-02
554	75.79	26.46	338.35	19.37	21.75	1.12E-02
555	75.15	26.42	338.35	19.37	21.71	1.10E-02
556	74.84	26.36	338.35	19.37	21.70	1.07E-02
557	74.60	26.25	338.35	19.37	21.69	1.01E-02
558	74.41	26.13	338.35	19.37	21.68	9.40E-03
559	74.23	26.07	338.35	19.37	21.67	9.09E-03

Table A-3 Flaw number 2: $a/t = 0.03t$ flaw, aspect ratio of 6:1, located in plate material, $K_I(t)$ does not includes through-wall weld residual stress

Time (min)	T(t) (°F)	$K_I(t)$ ksi \sqrt{in}	RT _{NDT} (°F)	K_{Ic} Weibull-a	W(b)	cpi(t)
545	83.26	20.68	184.88	20.19	37.85	2.73E-08
546	82.43	20.71	184.88	20.18	37.70	3.97E-08
547	81.60	20.73	184.88	20.16	37.55	5.21E-08
548	80.77	20.76	184.88	20.15	37.41	7.18E-08
549	79.94	20.79	184.88	20.13	37.26	9.68E-08
550	79.11	20.82	184.88	20.12	37.12	1.28E-07
551	78.28	20.84	184.88	20.10	36.98	1.57E-07
552	77.45	20.87	184.88	20.09	36.84	2.01E-07
553	76.62	20.90	184.88	20.08	36.70	2.54E-07
554	75.79	20.93	184.88	20.06	36.56	3.17E-07
555	75.15	20.89	184.88	20.05	36.45	2.79E-07
556	74.84	20.83	184.88	20.05	36.40	2.13E-07
557	74.60	20.71	184.88	20.04	36.36	1.13E-07
558	74.41	20.60	184.88	20.04	36.33	5.61E-08
559	74.23	20.54	184.88	20.04	36.30	3.65E-08

Table A-4 Allocation of *CPI* to region and aspect ratio for model that includes through-wall weld residual stress

RPV region	% of <i>CPI</i> by aspect ratio				Total
	2:1	6:1	10:1	infinite	
weld	0	25.68	11.97	48.29	85.94
plate	0	0.17	1.10	12.79	14.06
total	0	25.85	13.07	61.08	100.00

Table A-5 Results of PFM analyses with and without inclusion of through-wall weld residual stress

Flaw depth (a/t)	With through-wall weld residual stress		Without through-wall weld residual stress	
	<i>CPI</i> _{mean}	<i>CPF</i> _{mean}	<i>CPI</i> _{mean}	<i>CPF</i> _{mean}
0.03	4.33E-05	8.08E-06	9.28E-06	7.46E-06
0.05	1.93E-10	8.36E-14	0.00E+00	0.00E+00
0.06	7.95E-10	2.54E-12	0.00E+00	0.00E+00
0.07	2.13E-09	3.64E-12	0.00E+00	0.00E+00
0.08	4.40E-09	1.35E-11	2.29E-13	0.00E+00
0.12	1.95E-08	9.03E-11	1.53E-10	1.30E-13
0.18	3.06E-08	1.89E-10	1.03E-09	1.62E-12
0.23	2.18E-08	6.35E-11	1.61E-09	3.74E-12
0.25	1.67E-08	7.07E-11	1.65E-09	2.28E-12

References

- A1. P.T. Williams, T.L. Dickson, and S. Yin, *Fracture Analysis of Vessels – Oak Ridge FAVOR, v12.1, Computer Code: Theory and Implementation of Algorithms, Methods, and Correlations*, ORNL/TM-2012/567, Oak Ridge National Laboratory, Oak Ridge, TN, November 2012.
- A2 F.A. Simonen, S.R. Doctor, G.J. Schuster, and P.G. Heasler, *A Generalized Procedure for Generating Flaw Related Inputs for the FAVOR Code*, NUREG/CR-6817, Rev. 1, U.S. Nuclear Regulatory Commission, October 2003, available in ADAMS under Accession #ML051790410.

APPENDIX B: 2-D AXISYMMETRIC MODEL ANALYSES

Cool-Down Transients that Follow P-T Limit Curves

A range of reactor pressure vessel geometries subjected to postulated normal cool-down transients were analyzed using the probabilistic fracture mechanics (PFM) code FAVOR [B1] to determine trends for conditional probability of failure (*CPF*) as a function of postulated inner surface breaking flaw depths.

Figure B-1 depicts the pressure-temperature limits versus time curves computed according to those procedures for the *Vessel A* at 60 effective-full-power-years (EFPY) and a cool-down rate of 50 °F/hr. Other input variables required to perform the analyses of *Vessel A* presented in this report are summarized below.

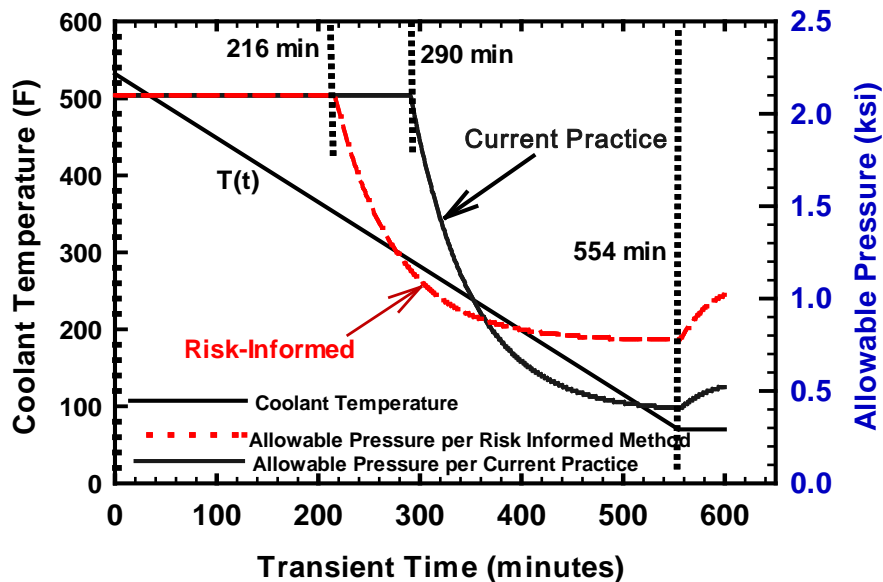


Fig. B-1 Pressure-temperature limits for normal cool-down transients determined using (1) standard ASME code procedures and (2) the recently proposed EPRI-MRP-250 risk-informed procedures. Results are shown for *Vessel A* at 60 EFPY for cool-down rate of 50 °F/hr.

Those postulated cool-down transients were defined using (1) standard ASME code procedures [B2] and (2) the recently proposed EPRI-MRP-250 risk-informed procedures [B3]. It should be noted that the allowable pressure below in Figure B-1, designated as Current Practice, is different from the one earlier illustrated in Figure 1-1 (also designated as Current Practice). The difference

is that Regulatory 1.99, revision 2, was used to calculate the RT_{NDT} at the ($t/4$) location for the derivation in of allowable pressure illustrated in Figure 1-1, whereas the 10 CFR 50.61a was used for the derivation of the allowable pressure illustrated in Figure B-1.

Vessel A Geometry and Material Properties

An idealized cylindrical wall RPV geometry model is used to simulate a PWR RPV designated as *Vessel A*. Input parameters required for the analyses of that vessel are summarized as follows:

- Geometric parameters include an inner radius (R_i) of 86 in. (2184.4 mm) with an 8.75 in. (222.25 mm) thick (inclusive of cladding), low-alloy carbon steel wall (t), giving an inner radius to wall thickness ratio (R_i/t) of approximately 10. The cladding thickness (t_{clad}) is 0.25 inches (6.35 mm). These dimensions are used in both the FAVOR and ABAQUS [B4] analyses.
- Temperature-dependent thermal-mechanical properties for the base (ferritic steel) and cladding (austenitic stainless steel) materials were used in both FAVOR and ABAQUS analyses.
 - For linear elastic analyses, the thermo-elastic property data for the base and cladding¹⁸ were adopted from Ref. [B6].
 - For elastic-plastic analyses, the temperature-dependent plasticity data for the base material were generated for the Shoreham plate using the Zerrilli-Armstrong (ZA) constitutive model [B7]. Those data were listed in Chapter 5 of Ref. [B8].
 - Temperature-independent plasticity data for the cladding material were used, as temperature-dependent data were not available.
 - Plasticity data are input to ABAQUS in the form of tables of true stress as a function of effective plastic strain.
- Embrittlement data for the beltline inner surface were obtained from the fluence maps of the three nuclear plants analyzed in the PTS re-evaluation studies [B9]. Those embrittlement data are included in Ref. [B10].

¹⁸ Effects of irradiation on material properties of cladding are not considered in the FAVOR LEM-based model of clad behavior. Reference [B5] provides post-irradiation test results for specimens extracted from 3-wire series-arc cladding applied to pressure vessel plate. Those data show limited effects of irradiation on tensile properties over the temperature range of interest herein.

Two-Dimensional (2-D) Axisymmetric Model Analyses

Analyses were conducted for a shallow, fully-circumferential, inner-surface breaking flaw with *Vessel A* geometry at 60 EFPY subjected to the EPRI-MRP-250 risk-informed derived pressure limits [B3], with a 50 °F/hr cool-down transient. The loading conditions for the postulated transient are depicted in Fig. B-1. Figure B-2 illustrates the finite element (FE) model for the RPV with a postulated 360° circumferential, ID flaw ($a/t = 0.03$). Version 6.11-1 of ABAQUS/CAE was used to generate the FE model. A very refined mesh in the vicinity of the clad-to-base metal interface was adopted to capture the steep stress gradients. Only half of the RPV cylindrical wall was directly modeled in the 2-D ABAQUS simulation and symmetry conditions were applied on the crack plane. The loading conditions of the postulated transient (consisting of coolant temperature, internal pressure, and convective heat transfer coefficient versus time curves) were applied to the RPV inner wall of the FE model. The same loading conditions were also used in the FAVOR calculation. Figure B-3 shows good agreement between ABAQUS and FAVOR solutions of the through-wall axial stress profiles for the uncracked RPV for two times in the transient, specifically at the first and second peaks of the applied K_I .

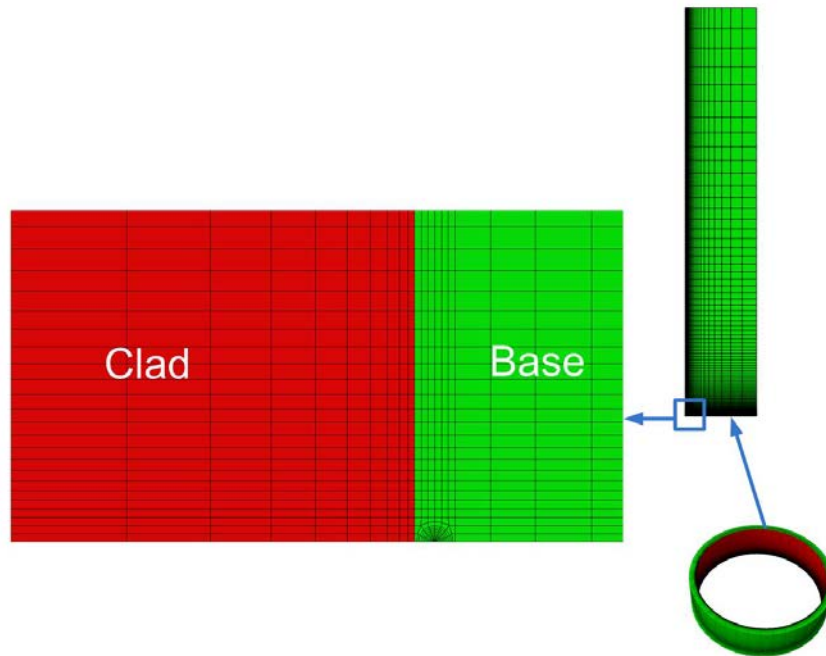


Fig. B-2 2-D axisymmetric finite element model with 360° shallow circumferential surface flaw ($a/t=0.03$).

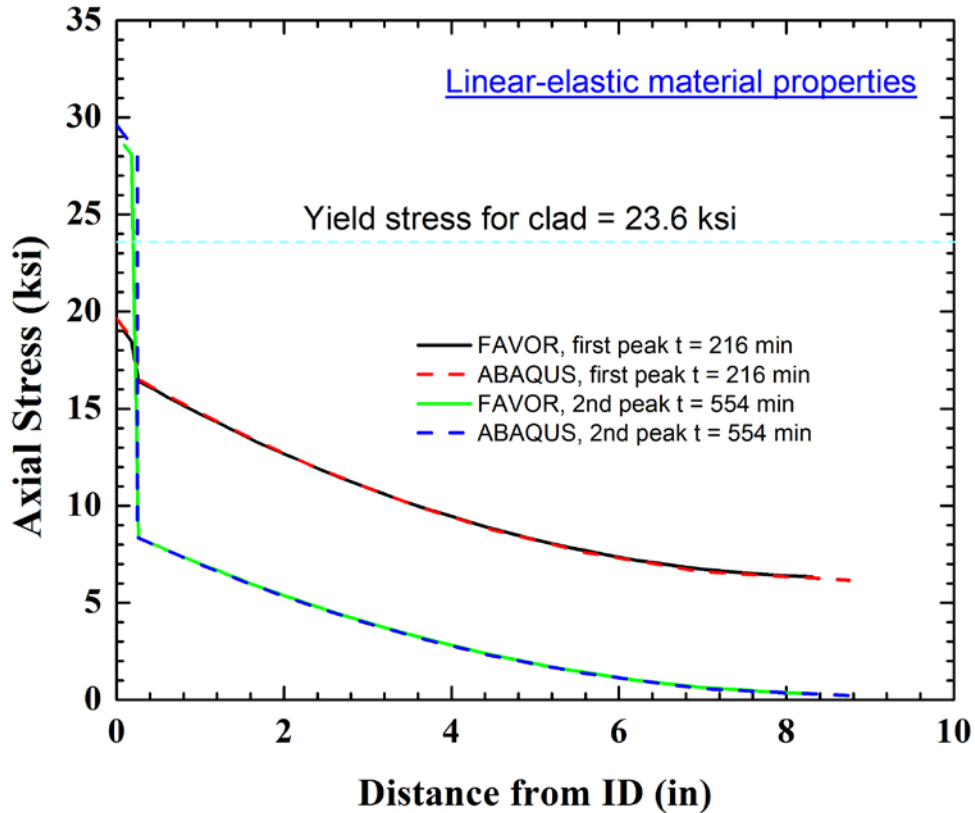


Fig. B-3 Comparison of FAVOR and ABAQUS finite-element (linear elastic) results of axial through-wall stresses for uncracked RPV. *Vessel A* geometry at 60 EFY subjected to the EPRI-MRP-250 risk-informed derived pressure limits [B3], with a 50 °F/hr cool-down transient.

Detailed 2-D LEFM analyses of shallow, circumferential, surface flaws having normalized depths $a/t = 0.03$ and 0.05 were performed with the ABAQUS finite element code [B4] to study the relative deformation of the two flaws. The same model conditions described previously in this Appendix were used in the ABAQUS analyses, except the two finite element models were subjected to 50 °F/hr cool-down thermal-only loading. Figure B-4 displays the deformed FE models at a time of 554 minutes, which is when the maximum applied K_I occurs under the thermal-only loading. The peak K_I for the $a/t = 0.03$ flaw is $23.8 \text{ ksi}\sqrt{\text{in}}$, which is higher than that for the $a/t = 0.05$ flaw at $K_I = 19.15 \text{ ksi}\sqrt{\text{in}}$.

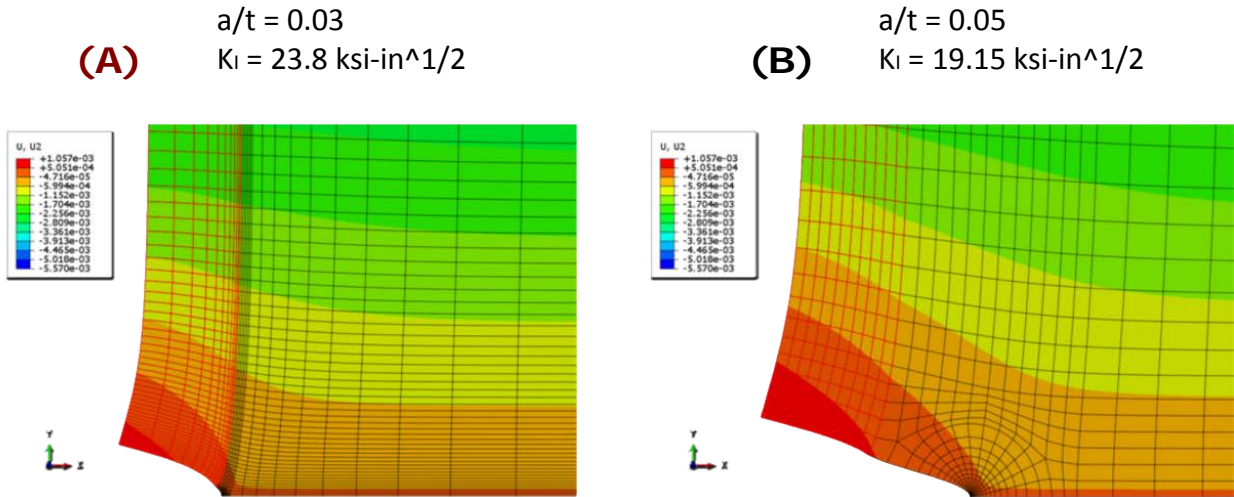


Fig. B-4 Deformed FE Models with different shallow flaw depths subjected to thermal loading. (100x amplification factor used for visualization of deformation). Vessel A geometry subjected to thermal-only loading from a 50 °F/hr cool-down transient.

Figure B-5 compares the crack opening displacement (COD) for shallow flaw models subjected to the thermal loading. The shallower flaw ($a/t = 0.03$) has a larger COD value due to the cladding effect. Clad stresses produce enhanced opening deformation of a surface flaw having its crack tip closer to the clad interface and, thereby, an elevated crack driving force. This result demonstrates that the enhanced deformation and driving force produced by clad stresses dissipate quickly with increasing surface flaw depth into the base metal. As shown in Fig. B-6, K_I values for the deeper flaw ($a/t = 0.05$) are slightly larger than those for the shallower flaw ($a/t = 0.03$) early in the transient (before 230 minutes); later, the K_I values for the shallower flaw increase above those for the deep flaw. The shallower flaw thus has larger peak K_I values than the deeper flaw when subjected to thermal only loading.

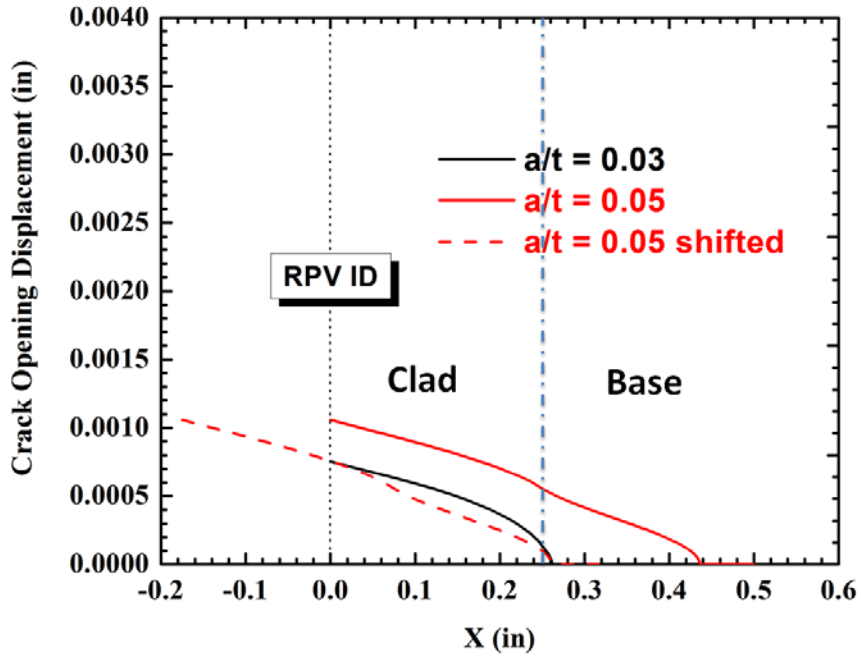


Fig. B-5 Crack opening displacement (COD) for shallow flaws with different flaw depths subjected to thermal-only loading.

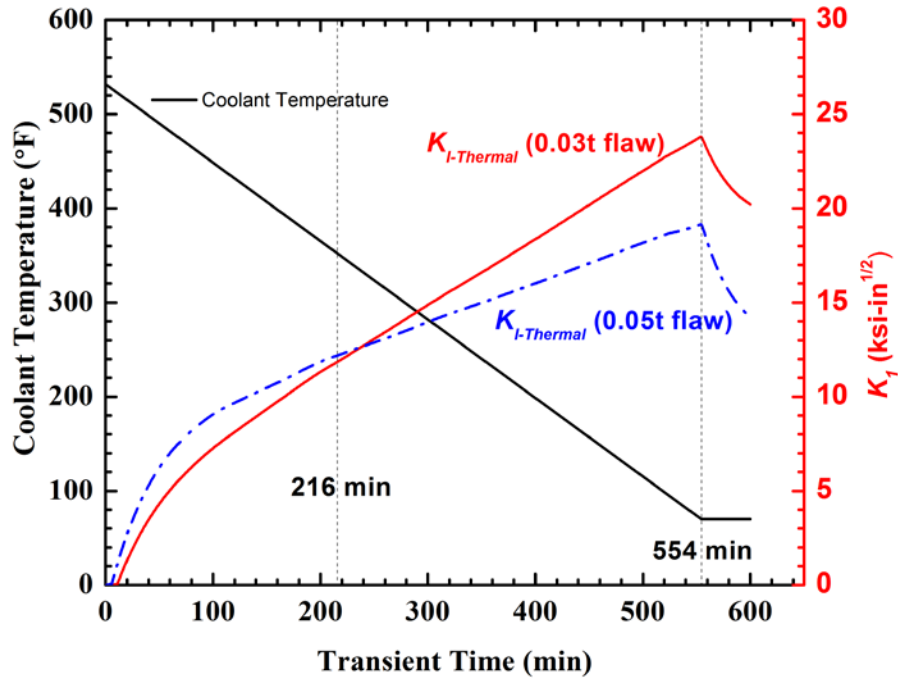


Fig. B-6 Comparison of K_I time history for the 2-D axisymmetric models ($a/t = 0.03$ and 0.05) subjected to 50° F/hr cool-down thermal-only transient.

Elastic-plastic fracture mechanics (EPFM) analyses were conducted for the same ABAQUS shallow flaw model with normalized depth ($a/t = 0.03$). Temperature-dependent plasticity data for base material were used in the EPFM analysis. Temperature-independent plasticity data for the cladding material were used, as temperature-dependent data were not available. At the time of second peak K_I (554 minutes), cladding materials deform plastically, as shown in Figure B-7. A small plastic zone develops around the crack-tip at the second peak, but it is still well contained by the elastic deformation, which validates the applicability of LEFM to this problem. In Sect. 2.2.1 of the main report, more detailed ABAQUS EPFM results generated from fully 3-D finite element models are compared with FAVOR LEFM calculations.

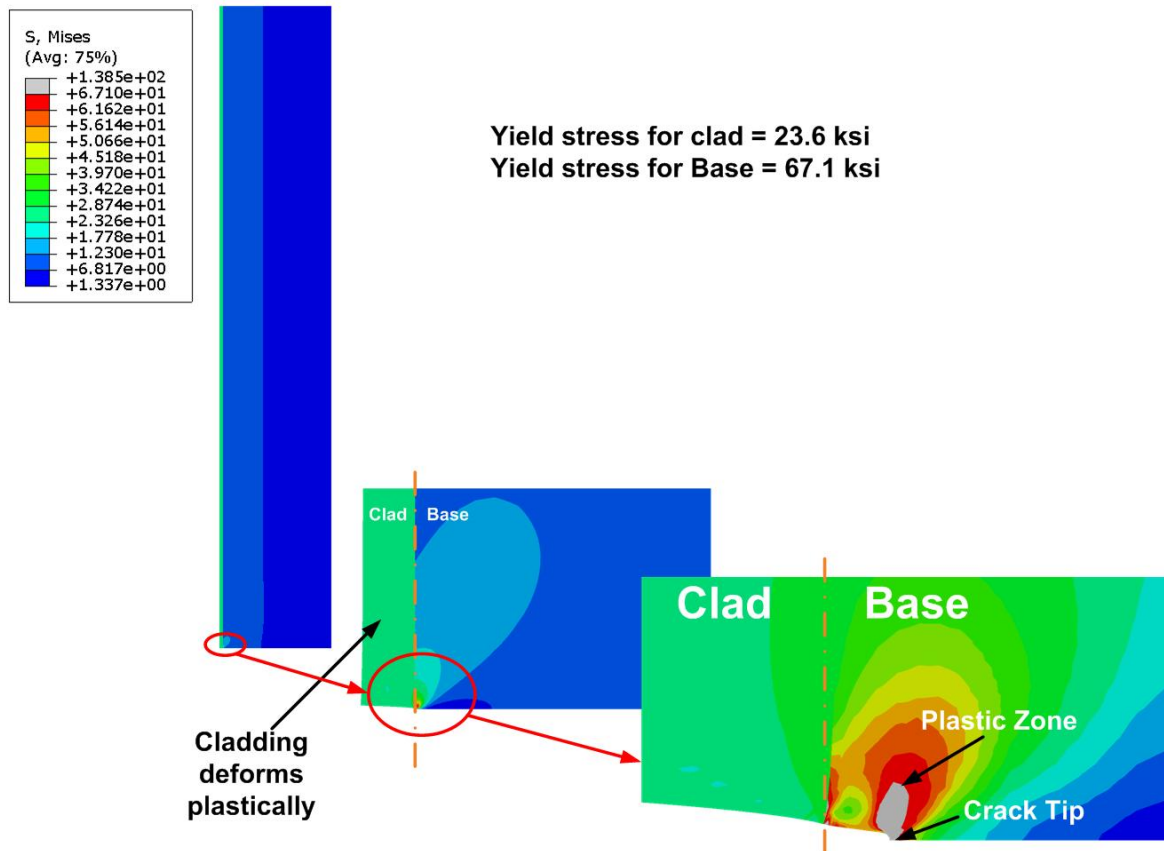


Fig. B-7 von Mises stress at the crack-tip for the 2-D axisymmetric model ($a/t = 0.03$) at time of 554 minutes.

REFERENCES

- B1. P.T. Williams, T.L. Dickson, and S. Yin, *Fracture Analysis of Vessels – Oak Ridge FAVOR, v12.1, Computer Code: Theory and Implementation of Algorithms, Methods, and Correlations*, ORNL/TM-2012/567, Oak Ridge National Laboratory, Oak Ridge, TN, November 2012.
- B2. *ASME Boiler and Pressure Vessel Code, Section XI, Appendix G*, “Fracture Toughness Criteria for Protection Against Failure”, New York, 2004.
- B3. EPRI MRP-250 – RI Appendix G: *Risk-Informed Method to Determine ASME Section XI Appendix G Limits for Ferritic Reactor Pressure Vessels - An Optional Approach Proposed for ASME Section XI Appendix G* (MRP-250) and (BWRVIP-215NP).
- B4. *ABAQUS Finite Element Software*, Version 6.11, Dassault Systems Simulia Corp., 2011.
- B5. F. M. Haggag, W. R. Corwin, and R. K. Nanstad, “Effects of Irradiation on the fracture properties of stainless steel weld overlay cladding,” *Nuclear Engineering and Design* 124 (1990) 129-141.
- B6. T. L. Dickson, P. T. Williams, and S. Yin, *Fracture Analysis of Vessels – Oak Ridge FAVOR, v09.1, Computer Code: User’s Guide*, ORNL/TM-2010/4, Oak Ridge National Laboratory, Oak Ridge, TN, January 2010.
- B7. F. J. Zerilli and R. W. Armstrong, “Dislocation-Mechanics-Based Constitutive Relations for Material Dynamics Calculations,” *J. Appl. Phys.* **61**(5), (1987) 1816-1825.
- B8. M. Wagenhofer, *Modeling the Transition Region Fracture Behavior of Ferritic Steels*, Ph.D. dissertation, University of Maryland, 2002.
- B9. M. EricksonKirk, et al., Technical Basis for Revision of the Pressurized Thermal Shock (PTS) Screening Limit in the PTS Rule (10 CFR 50.61) – Summary Report, NUREG-1806, Vol. 1, U.S. Nuclear Regulatory Commission, August, 2007
- B10. T.L. Dickson, et al., “Electronic Archive for the Results of Pressurized Thermal Shock Analyses for Beaver Valley, Oconee, and Palisades Reactor Pressure Vessels Generated with the 06.1 Version of FAVOR,” ORNL/NRC/LTR-07/04, Oak Ridge National Laboratory, Oak Ridge, TN, April 2007

APPENDIX C: SENSITIVITY STUDIES FOR OCCURRENCE OF LATE-PEAKING OF MAXIMUM APPLIED K_I

Effect of crack tip proximity to clad/base interface on contribution of cladding to total K_I

Analysis results in Section 1 of this report showed that the contribution of cladding to the total K_I diminishes rapidly as the distance from the crack tip to the clad/base metal interface increases, such that a $0.03t$ flaw can exhibit *2nd Peak Dominant* behavior, while the deeper $0.05t$ flaw will exhibit *1st Peak Dominant* behavior. In Fig. C-1, additional results illustrate the monotonically decreasing contribution of cladding to the total K_I over normalized flaw depths (a/t) ranging from 0.03 to 0.25. Table C-1 provides a tabulation of various K_I parameters computed at time $t = 554$ min in the P-T limits transient depicted in Fig. 1-1; the percentage contribution of $K_{I_{clad}}$ to the K_I total reflects a decreasing contribution with increasing distance from the clad/base interface. That drop in $K_{I_{clad}}$ contribution to total K_I is responsible for the abrupt drop (orders of magnitude) in *CPI vs. a/t* shown by most of the FAVOR-generated results.

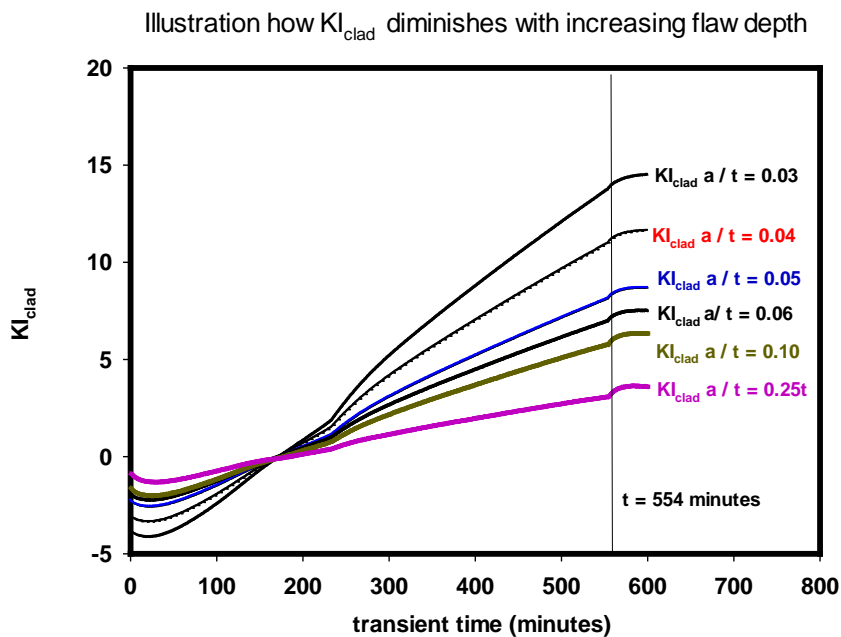


Fig. C-1 $K_{I_{clad}}$ versus transient time for values of normalized flaw depth (a/t) ranging from 0.03 to 0.25; P-T limits for postulated normal cool-down transient determined using ASME code procedures; *Vessel A* at 60 EFPY with a cool-down rate of 50 °F/hr.

Table C-1 Tabulation of various K_I parameters computed for range of normalized flow depths at time $t = 554\text{min}$ of P-T versus time limit curves used for analyses of Fig. C-1.

Flaw depth (a/t)	K_{Iclad} ksi $\sqrt{\text{in}}$	K_{Ibase} ksi $\sqrt{\text{in}}$	K_{Itotal} ksi $\sqrt{\text{in}}$	K_{Iclad} / K_{Itotal} (%)
0.03	13.75	7.18	20.93	65.7
0.04	10.97	8.13	19.10	57.4
0.05	8.14	8.91	17.05	47.7
0.06	6.96	9.56	16.52	42.1
0.10	5.80	11.64	17.44	33.3
0.25	3.10	15.35	18.45	16.8

Effects of Clad Stress-Free Temperature on Occurrence of Maximum Applied K_I at Second Peak

FAVOR analyses for different values of clad stress-free temperature (488 °F and 532 °F) exhibit the same trends of maximum K_I -values occurring at a second peak late in transient, as shown in Fig. C-2.

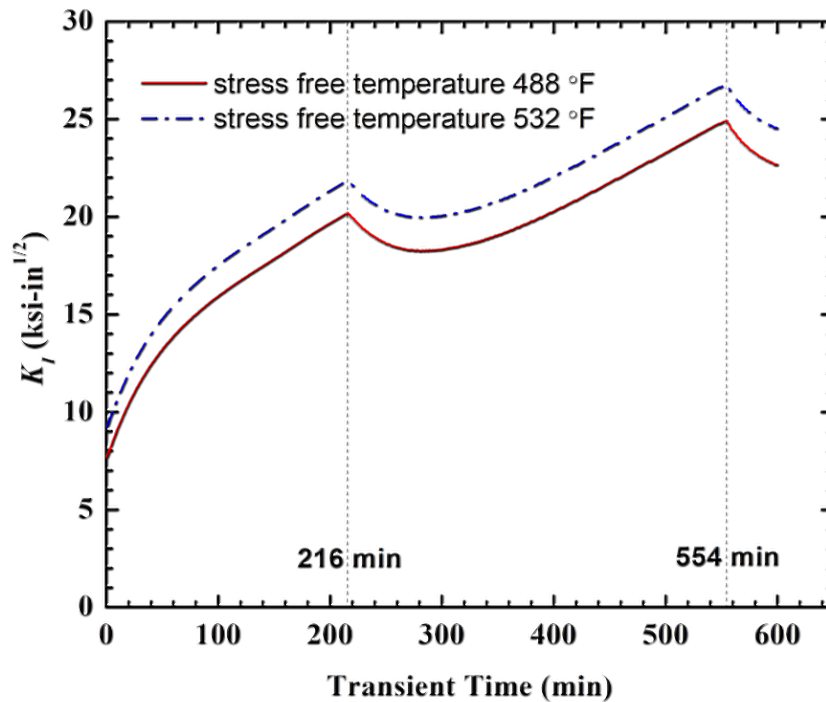


Fig. C-2 FAVOR analyses for different values of clad stress-free temperature exhibit same trends of maximum K_I occurring at second peak late in transient; results shown for $a = 0.03t$ flaw depth. Loading/vessel parameters are the same as those used for analyses depicted in Fig. C-1.

Minor variations in stress-free temperature do not change this behavior. For the particular case illustrated in Fig. C-3, a very low¹⁹ stress-free temperature of 225 °F is needed to reduce the 2nd peak sufficiently such that the applied K_I always remains below the minimum K_{Ic} , which would make the conditional probability of brittle fracture always zero.

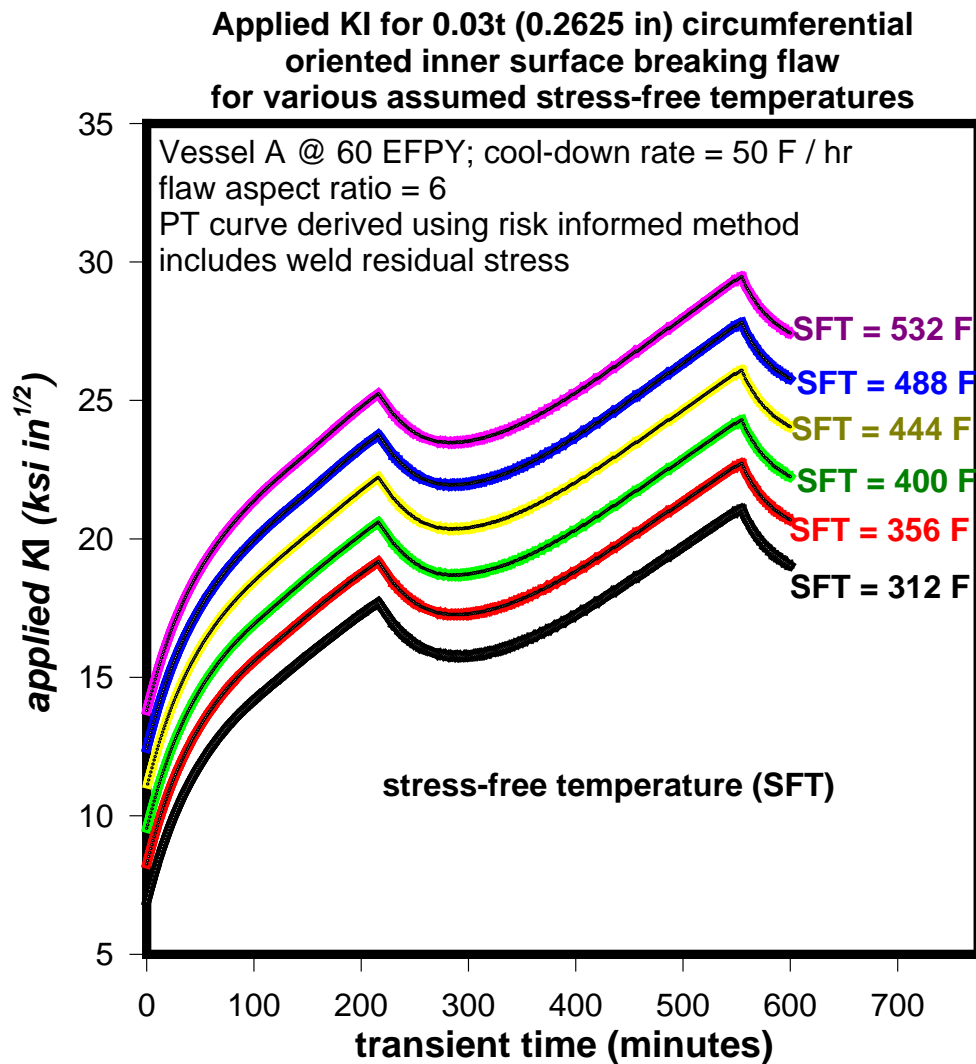


Fig. C-3 Minor variations in stress free temperature do not change the shallow flaw behavior

¹⁹ Based on experimental data [C1] and analyses [C2] developed at ORNL, the value for the stress-free temperature adopted in FAVOR is 488 °F. In the absence of specific experimental data, a common assumption (see for example [C3] and [C4]) is that, providing the post-weld heat treatment of the clad has been completely successful, it can be reasonably assumed that no underlying residual stresses exists in the base material, and that the stress-free temperature for the RPV is equal to the nominal operating temperature (~ 550°F). Thus, stress-free temperatures in the range of 488 to 550 °F are well accepted and can be supported by experimental evidence.

Some observations about time of occurrence of the 1st peak in applied K_I

Figure C-4 illustrates three different pressure transients that occur with a constant cool-down transient of 50 °F / hr. The three pressure transients have different values (188, 233, and 283 min) of $\Delta t_{\text{initial}}$ – the transient time at which the pressure is initially reduced below the steady state pressure. The coolant temperature reaches an assumed ambient temperature of 70 °F at 554 min.

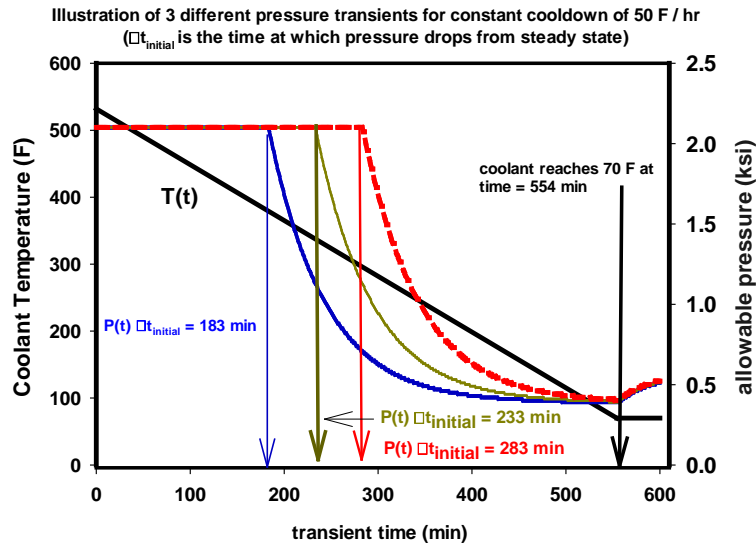


Fig. C-4 Illustration of three different pressure transients – each with distinct value of $\Delta t_{\text{initial}}$ – the time at which pressure is reduced below steady state pressure. The thermal transient is same for all three transients.

Figure C-5 illustrates the three K_I time histories for a shallow $0.03t$ circumferentially oriented inner surface breaking flaw (with an aspect ratio = 6) subjected to the three distinct transients illustrated in Figure C-4. For each of the three transients, the value of K_I reaches its 1st peak at $\Delta t_{\text{initial}}$ whereas the magnitude of K_I reaches its 2nd peak (for all three transients) at the transient time of 554 min corresponding to the time when the coolant temperature reaches 70 °F.

The magnitudes of K_I at the 1st peak for $\Delta t_{\text{initial}} = 183$ min and 233 min are 24.2 ksi $\sqrt{\text{in}}$ and 25.7 ksi $\sqrt{\text{in}}$ which are less than the magnitude $K_I = 26.5$ ksi $\sqrt{\text{in}}$ at the 2nd peak. However, for the case where $\Delta t_{\text{initial}} = 283$ min, the magnitude of the K_I at the 1st peak for $\Delta t_{\text{initial}} = 283$ min is 27.1 ksi $\sqrt{\text{in}}$ which exceeds magnitude $K_I = 26.5$ ksi $\sqrt{\text{in}}$ at the 2nd peak.

Illustration that the magnitude of K_I @ 1st peak is proportional to $\Delta t_{\text{initial}}$

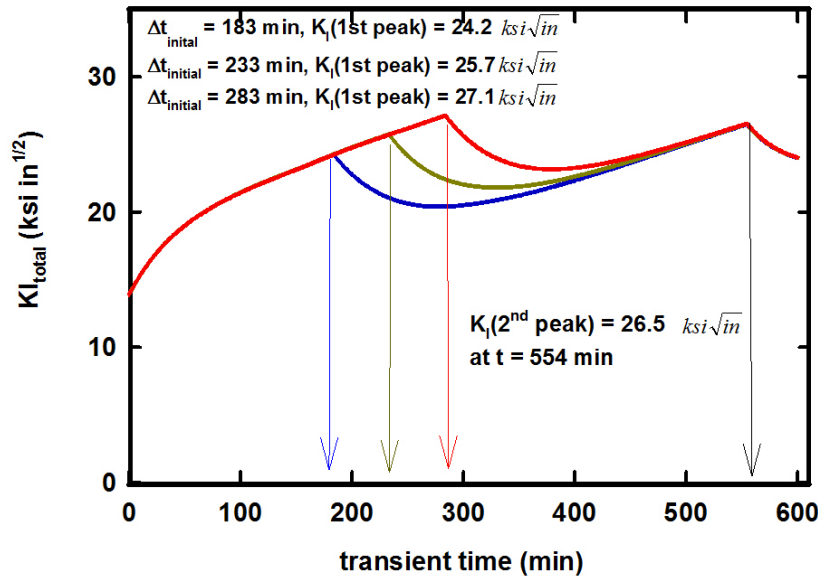


Fig. C-5 – Illustration that the magnitude of the 1st peak of K_I corresponds to $\Delta t_{\text{initial}}$; therefore, the smaller $\Delta t_{\text{initial}}$, the greater the likelihood that the magnitude of K_I at the 2nd peak will exceed the magnitude of K_I at the 1st peak.

Therefore, as illustrated in Figures C-4 and C-5:

- (1) The transient time at which the 1st peak of K_I occurs corresponds to the time at which pressure is reduced below steady state ($\Delta t_{\text{initial}}$).
- (2) The smaller the value of $\Delta t_{\text{initial}}$, the greater the likelihood that the magnitude of the K_I at the 2nd peak will exceed the magnitude of K_I at the 1st peak.

Sensitivity of the Occurrence of Maximum Applied K_I at Second Peak to Variables of Nuclear Plant RPV, Length of Operation (EFPY), and Plant Cool-Down Rate

A sensitivity study was conducted using the FAVOR code to evaluate the late peaking of total applied K_I for very shallow, circumferentially oriented, inner surface flaws. A non-monotonic variation of CPI with flaw depth occurs because, depending upon the conditions being modeled, either the first peak (*1st peak dominant*, depicted in Fig. C-6) or the second peak (*2nd peak dominant* in Fig. C-6) in applied K_I may control the value of CPI . The late second peak in applied

K_I for the very shallow flaws is caused by a differential in thermal expansion coefficients for cladding and base material. Variables in this study were

- RPVs in three NPPs modeled as part of the PTS re-evaluation studies [C5-C6]. These vessels have different clad thicknesses; Table C-2 summarizes relevant geometric dimensions for these vessels. The flaw depth is not exactly equal to the clad depth because in FAVOR the flaw depth must be an even 1/100th of the vessel wall thickness.
- EFPY
- cool-down rate
- method of calculating maximum allowable pressure
 - EPRI-MRP-250 risk-informed approach [C7]
 - ASME Code procedure [C8]

Table C-2 RPV / flaw geometry for three plants used in sensitivity study

Nuclear Plant RPV	Internal radius (in)	Wall thickness including clad (in)	Clad thickness (in)	Flaw depth a		
				a / t	(in)	percentage of flaw depth covered by clad
Plant A	86.0	8.750	0.250	0.03	0.2526	98.9
Plant B	85.5	8.626	0.188	0.03	0.2588	72.6
Plant C	78.5	8.036	0.156	0.02	0.1607	97.0

Postulated cool-down transients computed according to both EPRI risk-informed and ASME code methods were applied to the RPVs postulated to contain a circumferential, through-clad, inner surface-breaking flaw just penetrating into the base metal; see Table C.2 for RPV geometry/flaw parameters. The matrix of cases included a range of cool-down rates and EFPYs.

Table C-3 provides a summary of results from this study. For the EPRI risk-informed method [C7] of deriving maximum allowable pressure curves, the maximum K_I for a circumferential, shallow, inner surface-breaking flaw occurred at the second peak late in the transient for 31 out of the 36 cases involving the three RPVs; a sampling of results for the three RPVs demonstrating the maximum second peak in applied K_I are shown in Fig. C-7. The ASME code procedure [C8] of deriving maximum allowable pressure curves resulted in 23 out of 36 cases have a maximum K_I

at the second peak; sample results for the three RPVs based on 60 EFPY and 50 °F/hr cool-down rate are shown in Fig. C-8.

The following observations are made with respect to the analyses presented herein:

- When the shallow surface-flaw tip is closer to the clad/base interface, the cool-down problem is driven more by the thermal contribution to applied- K_I than the pressure contribution to applied- K_I .
- Application of risk-informed methodology tends to reduce the time $\Delta t_{\text{initial}}$ at which pressure must decrease from steady state, which gives rise to the late-peaking phenomena.
- For the higher levels of embrittlement (beyond 60 EFPY), the 2nd peak is higher than the 1st peak for nearly all cases, for both the risk-informed and ASME Code methodologies (Note that the level of embrittlement differs between plants for the same EFPY).
- For those transients in which the risk-informed methodology was used to derive the maximum allowable pressure, the 2nd peak is higher than the 1st peak, with the exception of Plant B through 60 EFPY. An explanation for that result is given as follows:
 - Analyses of the postulated flaw in Plant B predict the 1st peak higher than the 2nd peak for all but one case (through 60 EFPY).
 - Plants A, B and C have different clad thicknesses, ranging from 0.156 in to 0.250 in. Table C-2 indicates the tip of the flaw postulated in Plant B is more distant from the clad/base interface, when compared to flaws in the other two plants; only 73% of the flaw in Plant B is covered by the cladding, as opposed to almost 99% for the flaw in plant A.
 - Figure C-1 and Table C-1 indicate the percentage contribution of $K_{I\text{clad}}$ to the K_I total **decreases** with increasing distance of the flaw tip from the clad/base interface.
 - That reduced contribution of $K_{I\text{clad}}$, a thermally-driven part of K_I total, reduces the likelihood of a maximum late peak in applied- K_I .

The summary of Table C-3 was compiled from more detailed results generated during analyses of Plants A, B and C and shown in Tables C-4 through C-7. These results are representative of a larger body of analyses indicating the postulated transient based on the EPRI risk-informed method leads to higher *CPI* values for very shallow surface flaws, when compared with ASME methods.

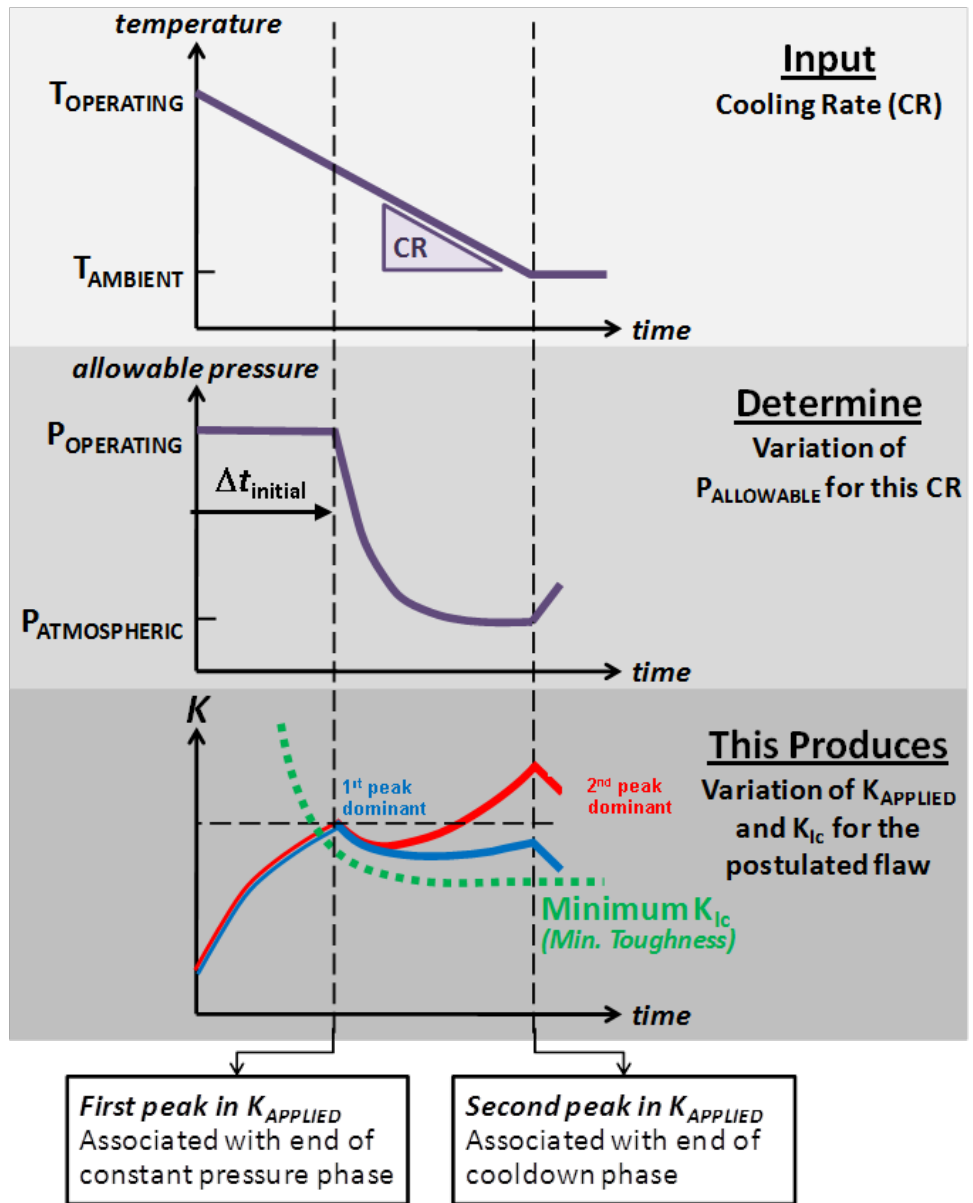


Fig. C-6 Illustration of the possible variations of applied $K_I (=K_{APPLIED})$ with time during a postulated cool-down.

Table C-3 Summary sensitivity study on the joint influence of the three parameters [RPV geometry, embrittlement (i.e., EFPY), and cool down rate] on whether the 1st peak or the 2nd peak in the total applied K_I is higher.

EFPY (yrs.)	Cool-Down Rate (°F/hr)	Method Used to Calculate Maximum Allowable Pressure that Defines the Postulated Cool-Down Transient					
		Plant A $t_{CLAD} = 0.25$ -in.		Plant B $t_{CLAD} = 0.188$ -in.		Plant C $t_{CLAD} = 0.156$ -in.	
		Risk Informed	ASME Code	Risk Informed	ASME Code	Risk Informed	ASME code
32	50	2 nd	1 st	1 st	1 st	2 nd	2 nd
	75	2 nd	1 st	1 st	1 st	2 nd	2 nd
	100	2 nd	1 st	1 st	1 st	2 nd	1 st
60	50	2 nd	2 nd	2 nd	1 st	2 nd	2 nd
	75	2 nd	1 st	1 st	1 st	2 nd	2 nd
	100	2 nd	1 st	1 st	1 st	2 nd	2 nd
Y1	50	2 nd	2 nd	2 nd	2 nd	2 nd	2 nd
	75	2 nd	2 nd	2 nd	1 st	2 nd	2 nd
	100	2 nd	2 nd	2 nd	2 nd	2 nd	2 nd
Y2	50	2 nd	2 nd	2 nd	2 nd	2 nd	2 nd
	75	2 nd	2 nd	2 nd	2 nd	2 nd	2 nd
	100	2 nd	2 nd	2 nd	2 nd	2 nd	2 nd

For Plant A; EFPY = Y1 = 200; EFPY = Y2 = 500
 For Plant B; EFPY = Y1 = 500; EFPY = Y2 = 1000
 For Plant C; EFPY = Y1 = 100; EFPY = Y2 = 200

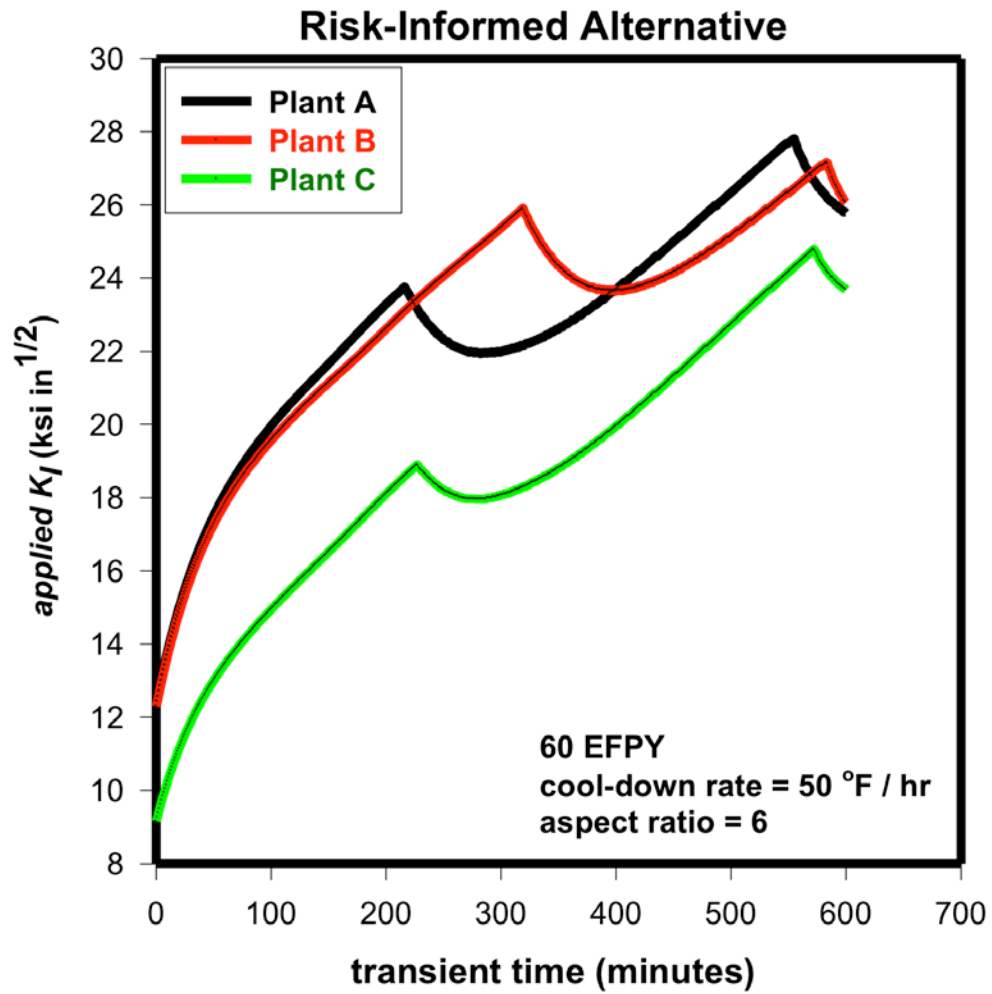


Fig. C-7 For P-T curves derived from the EPRI risk-informed method and cool-down rate of 50 °F /hr, the maximum K_I for shallow internal surface breaking flaw occurred at the 2nd peak late in the postulated transient for 35 out of 36 cases examined; three cases are shown here for illustration.

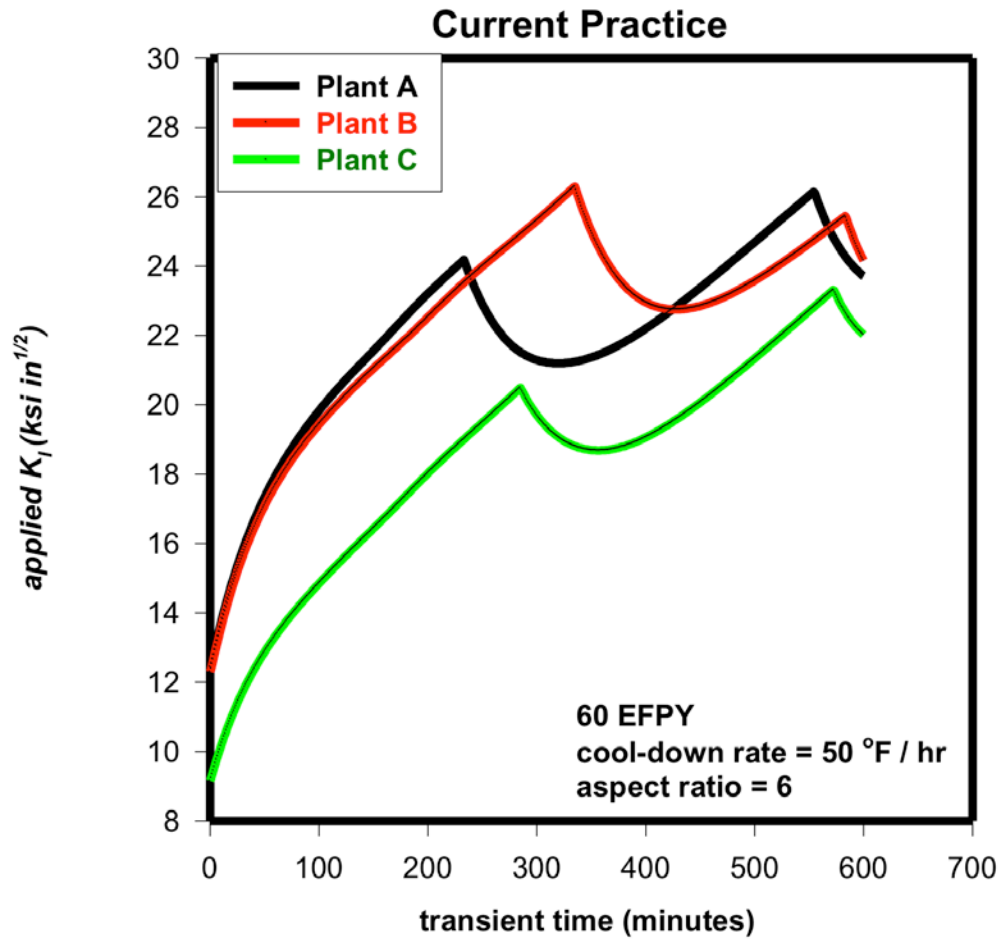


Fig. C-8 For P-T curves derived from the ASME code procedure and cool-down rate of 50 °F/hr., the maximum K_I for shallow internal surface-breaking flaw occurred at the 2nd peak, late in the postulated transient for 20 out of 36 cases examined; three cases are shown here for illustration.

Table C-4: Nomenclature for Tables C-5, C-6, and C-7

Column Name	Definition
Case No.	case identifier
Plant	RPV geometry* used in analysis – from Plant A, B, or C
EFPY	effective full power years of operation
Rate	constant rate of cool-down (°F/hr) - used in derivation of maximum allowable pressure
Pressure Derivation Rule	method used in derivation of maximum allowable pressure: EPRI risk-informed (RI) method in [C7] or ASME code procedure (CP) in [C8]
Pressure Derivation ETC	Embrittlement Trend Curve - used to calculate $RT_{NDT}(t/4)$ as required in derivation of maximum allowable pressure. ASME CP uses RG 1.99 – revision 2 [C9], and EPRI RI uses 10 CFR 50.61(a) [C10].
$\Delta t_{initial}$	period of time in minutes at which pressure remains at steady state after beginning of cool-down transient (see Fig. C-4).
t_{peak}	the transient time in minutes at which the applied K_I for the shallow inner surface breaking circumferential flaw (with 6:1 aspect ratio) reaches its maximum value (see Fig. C-4).
$T(t_{peak})$	the temperature [°F] at the crack tip at transient time t_{peak}
$K_I(t_{peak})$	the value of K_I [ksi-√in)]for the shallow inner surface breaking circumferential flaw (with 6:1 aspect ratio) at t_{peak} .
Maximum (1 st or 2 nd)	the peak that has the higher value of K_I for the shallow flaw

* Analyses of RPVs from plants A and B assumed a shallow surface flaw of depth $a = 0.03t$, whereas the flaw assigned to the RPV of plant C had depth $a = 0.02t$. An objective here was to analyze a flaw that penetrated the cladding and extended just slightly into the base metal. Thus, the thinner cladding used in the RPV of plant C (see Table C-1) required a shallower flaw to achieve that objective.

Table C-5 Results generated in sensitivity study for Plant A assuming a circumferential, inner surface-breaking flaw with depth $a = 0.03t$ and 6:1 aspect ratio (including weld residual stress)

Case No.	Plant	EPY (years)	Rate (°F / hr)	Maximum Pressure Derivation		$\Delta t_{\text{initial}} = t_{\text{peak1}}$ (min.)	t_{peak2} (min.)	$K_I(0.03t)$ (at t_{peak1})	$K_I(0.03t)$ (at t_{peak2})	Max peak 1 st or 2 nd	$T(0.03t)$ (at max t_{peak})
				Rules	RT _{NDT} (t/4)						
1	A	32	50	RI ⁽¹⁾	208.4	245	554	26.05	28.40	2 nd	75.79
	A	32	50	CP ⁽²⁾	250.4	269	554	26.72	26.51	1 st	314.08
2	A	32	75	RI ⁽¹⁾	208.4	165	369	28.58	29.68	2 nd	79.01
	A	32	75	CP ⁽²⁾	250.4	184	369	29.38	28.24	1 st	310.17
3	A	32	100	RI ⁽¹⁾	208.4	125	277	30.94	31.01	2 nd	81.47
	A	32	100	CP ⁽²⁾	250.4	142	277	31.99	30.02	1 st	306.18
4	A	60	50	RI ⁽¹⁾	232.8	216	554	25.24	28.35	2 nd	75.79
	A	60	50	CP ⁽²⁾	281.2	233	554	25.72	26.46	2 nd	75.79
5	A	60	75	RI ⁽¹⁾	232.8	145	369	27.66	29.63	2 nd	79.01
	A	60	75	CP ⁽²⁾	281.2	160	369	28.36	28.19	1 st	340.15
6	A	60	100	RI ⁽¹⁾	232.8	110	277	29.87	30.96	2 nd	81.47
	A	60	100	CP ⁽²⁾	281.2	123	277	30.81	29.97	1 st	339.36
7	A	200	50	RI ⁽¹⁾	296.3	141	554	22.85	28.35	2 nd	75.79
	A	200	50	CP ⁽²⁾	338.5	164	554	23.60	26.46	2 nd	75.79
8	A	200	75	RI ⁽¹⁾	296.3	95	369	24.93	29.63	2 nd	79.01
	A	200	75	CP ⁽²⁾	338.5	114	369	26.01	28.14	2 nd	79.01
9	A	200	100	RI ⁽¹⁾	296.3	72	277	26.52	30.96	2 nd	81.47
	A	200	100	CP ⁽²⁾	338.5	89	277	28.14	29.93	2 nd	81.47
10	A	500	50	RI ⁽¹⁾	374.6	48	554	18.86	28.35	2 nd	75.79
	A	500	50	CP ⁽²⁾	366.4	131	554	22.53	26.46	2 nd	75.59
11	A	500	75	RI ⁽¹⁾	374.6	32	369	19.53	29.63	2 nd	79.01
	A	500	75	CP ⁽²⁾	366.4	91	369	24.7	28.14	2 nd	79.01
12	A	500	100	RI ⁽¹⁾	374.6	25	277	20.12	30.96	2 nd	81.47
	A	500	100	CP ⁽²⁾	366.4	71	277	26.52	29.92	2 nd	81.47

(1) RI: risk informed methodology of deriving maximum allowable pressure ($\alpha = 1, \beta=110, \Delta RT_{\text{NDT}}$ correlation from 10CFR 50.61a)

(2) CP: current practice methodology of deriving maximum allowable pressure ($\alpha = 2, \beta=0, \Delta RT_{\text{NDT}}$ correlation from RG1.99 rev 2 [C10])

Magnitude of K_I for 0.03t increased by 5.53 ksi $\sqrt{\text{in}}$ due weld residual stress of magnitude 5.53 ksi $\sqrt{\text{in}}$

Table C-6 Results generated in sensitivity study for Plant B assuming a circumferential, inner surface-breaking flaw with depth $a = 0.03t$ and 6:1 aspect ratio (including weld residual stress)

Case No.	Plant	EPY (years)	Rate (°F / hr)	Maximum Pressure Derivation		$\Delta t_{\text{initial}} = t_{\text{peak1}}$ (min.)	t_{peak2} (min.)	$K_I(0.03t)$ (at t_{peak1})	$K_I(0.03t)$ (at t_{peak2})	Max peak 1 st or 2 nd	$T(0.03t)$ (at max t_{peak})
				Rules	RT _{NDT} (t/4)						
1	C	32	50	RI	149.1	370	583	28.80	25.89	1 st	252.63
	C	32	50	CP	186.2	339	583	27.96	27.75	1 st	278.44
2	C	32	75	RI	149.1	227	389	30.35	29.00	1 st	279.75
	C	32	75	CP	186.2	251	389	31.31	27.56	1 st	249.77
3	C	32	100	RI	149.1	172	292	32.81	30.24	1 st	279.38
	C	32	100	CP	186.2	192	292	33.87	29.24	1 st	246.12
4	C	60	50	RI	160.0	319	583	27.40	27.70	2 nd	75.12
	C	60	50	CP	215.6	335	583	27.85	25.77	1 st	281.78
5	C	60	75	RI	160.0	214	389	29.82	28.95	1 st	295.99
	C	60	75	CP	215.6	228	389	30.39	27.41	1 st	278.50
6	C	60	100	RI	160.0	162	292	32.28	30.19	1 st	296.01
	C	60	100	CP	215.6	174	292	32.92	29.13	1 st	173.00
7	C	500	50	RI	230.3	242	583	25.33	27.65	2 nd	75.12
	C	500	50	CP	306.7	226	583	24.88	25.67	2 nd	75.12
8	C	500	75	RI	230.3	163	389	27.77	28.90	2 nd	77.31
	C	500	75	CP	306.7	155	389	27.40	27.31	1 st	369.71
9	C	500	100	RI	230.3	124	292	26.62	29.35	2 nd	79.65
	C	500	100	CP	306.7	120	292	26.34	28.57	2 nd	79.65
10	C	1000	50	RI	267.3	198	583	24.03	27.65	2 nd	75.12
	C	1000	50	CP	324.1	205	583	24.25	25.67	2 nd	75.12
11	C	1000	75	RI	267.3	133	389	26.34	28.85	2 nd	77.31
	C	1000	75	CP	324.1	141	389	26.73	27.26	2 nd	77.31
12	C	1000	100	RI	267.3	101	292	24.99	29.35	2 nd	79.65
	C	1000	100	CP	324.1	109	292	25.57	28.57	2 nd	79.65

(1) RI: risk informed methodology of deriving maximum allowable pressure ($\alpha = 1, \beta=110, \Delta RT_{\text{NDT}}$ correlation from 10CFR 50.61a)

(2) CP: current practice methodology of deriving maximum allowable pressure ($\alpha = 2, \beta=0, \Delta RT_{\text{NDT}}$ correlation from RG1.99 rev 2 [C10])

Magnitude of K_I for 0.03t increased by 5.49 ksi $\sqrt{\text{in}}$ due weld residual stress

Table C-7 Results generated in sensitivity study for Plant C assuming a circumferential, inner surface-breaking flaw with depth $a = 0.02t$ and 6:1 aspect ratio (including weld residual stress)

Case No.	Plant	EFPY (years)	Rate (°F / hr)	Maximum Pressure Derivation		$\Delta t_{\text{initial}} = t_{\text{peak1}}$ (min.)	t_{peak2} (min.)	$KI(0.03t)$ (at t_{peak1})	$KI(0.03t)$ (at t_{peak2})	Max peak 1 st or 2 nd	$T(0.03t)$ (at max t_{peak})
				Rules	RT _{NDT} (t/4)						
1	C	32	50	RI	210.9	256	572	21.31	25.47	2 nd	73.52
	C	32	50	CP	233.6	302	572	22.68	23.70	2 nd	73.52
2	C	32	75	RI	210.9	171	382	22.89	26.19	2 nd	74.55
	C	32	75	CP	233.6	205	382	24.37	24.75	2 nd	74.55
3	C	32	100	RI	210.9	131	286	24.58	27.02	2 nd	76.81
	C	32	100	CP	233.6	157	286	26.10	25.87	1 st	291.75
4	C	60	50	RI	235.3	227	572	20.49	25.43	2 nd	73.52
	C	60	50	CP	248.0	285	572	22.16	23.70	2 nd	73.52
5	C	60	75	RI	235.3	152	382	22.06	26.19	2 nd	74.55
	C	60	75	CP	248.0	194	382	23.88	24.75	2 nd	74.55
6	C	60	100	RI	235.3	115	286	23.57	27.02	2 nd	76.81
	C	60	100	CP	248.0	148	286	25.58	25.87	2 nd	76.81
7	C	100	50	RI	261.0	196	572	19.57	25.43	2 nd	73.52
	C	100	50	CP	256.9	274	572	21.83	23.70	2 nd	73.52
8	C	100	75	RI	261.0	132	382	21.11	26.19	2 nd	74.55
	C	100	75	CP	256.9	183	382	23.41	24.69	2 nd	74.55
9	C	100	100	RI	261.0	100	286	22.55	27.02	2 nd	76.81
	C	100	100	CP	256.9	140	286	25.11	25.83	2 nd	76.81
10	C	200	50	RI	307.7	140	572	17.80	25.43	2 nd	73.52
	C	200	50	CP	263.8	266	572	21.60	23.68	2 nd	73.52
11	C	200	75	RI	307.7	94	382	19.22	26.15	2 nd	74.55
	C	200	75	CP	263.8	181	382	23.32	24.69	2 nd	74.55
12	C	200	100	RI	307.7	72	286	20.51	26.98	2 nd	76.81
	C	200	100	CP	263.8	139	286	25.05	25.83	2 nd	76.81

(1) RI: risk informed methodology of deriving maximum allowable pressure ($\alpha = 1, \beta=110, \Delta RT_{\text{NDT}}$ correlation from 10CFR 50.61a)

(2) CP: current practice methodology of deriving maximum allowable pressure ($\alpha = 2, \beta=0, \Delta RT_{\text{NDT}}$ correlation from RG1.99 rev 2)

Magnitude of K_I for 0.02t increased by 4.45 ksi $\sqrt{\text{in}}$ due weld residual stress

REFERENCES

- C1. T.L. Dickson, et al., "Evaluations of Margins in the ASME Rules for Defining the P-T Curve for a RPV, *Proceedings of the 1999 ASME Pressure Vessel and Piping Division Conference*, July 1999, Boston, MA.
- C2. P.T. Williams, T.L. Dickson, and S. Yin, *Fracture Analysis of Vessels – Oak Ridge FAVOR, v12.1, Computer Code: Theory and Implementation of Algorithms, Methods, and Correlations*, ORNL/TM-2012/567, Oak Ridge National Laboratory, Oak Ridge, TN, November 2012.
- C3. C. Jang, I-S. Jeong, and S-Y Hong, "Treatment of Stainless Steel Cladding in Pressurized Thermal Shock Evaluation: Deterministic Analyses," *Journal of the Korean Nuclear Society* **33(2)**, (2001) 132-144.
- C4. I. Sattari-Far and M. Andersson, *Cladding Effects of Structural Integrity of Nuclear Components*, SKI Report 2006:23, Swedish Nuclear Power Inspectorate, June 2006.
- C5. M.T. EricksonKirk and T.L. Dickson, *Recommended Screening Limits for Pressurized Thermal Shock*, NUREG 1874, U.S. Nuclear Regulatory Commission, <http://www.nrc.gov/reading-rm/doc-collections/nuregs/staff/sr1874/>, March 2010.
- C6. T.L. Dickson, et al., "Electronic Archive for the Results of Pressurized Thermal Shock Analyses for Beaver Valley, Oconee, and Palisades Reactor Pressure Vessels Generated with the 06.1 Version of FAVOR," ORNL/NRC/LTR-07/04, Oak Ridge National Laboratory, April 2007.
- C7. EPRI MRP-250 – RI Appendix G: Risk-Informed Method to Determine ASME Section XI Appendix G Limits for Ferritic Reactor Pressure Vessels - An Optional Approach Proposed for ASME Section XI Appendix G (MRP-250) and (BWRVIP-215NP).
- C8. ASME Boiler and Pressure Vessel Code, Section XI, Appendix G, "Fracture Toughness Criteria for Protection Against Failure", New York, 2004.
- C9. U.S. Nuclear Regulatory Commission, Regulatory Guide 1.99, Revision 2, *Radiation Embrittlement of Reactor Vessel Materials*, May 1988.
- C10. NRC 10 CFR 50.61a Alternate fracture toughness requirements for protection against pressurized thermal shock events.

APPENDIX D: SOME RELEVANT EXPERIMENTAL STUDIES OF RPV CLADDING

ORNL Thermal Shock Experiments

A series of thermal shock experiments [D1] were performed on a large, clad, steel cylinder that contained both through-clad and sub-clad flaws spaced at intervals on the inner surface. The objective of those experiments was to evaluate the effects of cladding on the initiation and propagation of flaws in reactor pressure vessels. The thermal shock was achieved by heating the cylinder and then exposing the inner surface to a liquid nitrogen bath. One of those experiments (TSE-8) is summarized in the following because of its relevance to an assumption used in the FAVOR code: all internal, surface-breaking and sub-clad, finite-length flaws that initiate in cleavage fracture are assumed to become infinite length (or uniform depth) internal surface-breaking flaws.

TSE-8 Experiment

Information about the cylinder includes the following [D1] data.

- Outer diameter: 991 mm
- Length: 1221 mm
- Wall thickness: 152 mm (including clad thickness)
- Ferritic material: A508 class 2 chemistry; $RT_{NDT} = 66\text{ }^{\circ}\text{C}$
- Clad material: 304L stainless (90 degree segment); Inconel 600 (270° segment)
- Clad application: strip-weld (25 mm wide) submerged arc process (strips applied in longitudinal direction); two strips applied, followed final machining to reduce thickness to 4.6 mm.

All six flaws in the cylinder were located at mid-length of the test cylinder and oriented axially; flaws were sub-clad, semi-elliptical (aspect ratio of 6:1), and 19mm in depth measured relative to the clad/base interface. Reference D1 describes the thermal shock transient applied to the vessel and provides the following observations regarding transient events for flaw #3:

- Two initiation/arrest events were recorded during transient
- Extension of the flaw was completely sub-clad, with the length extending to approximately 1 m and the maximum depth to 71 mm (measured from the inner surface of the vessel); one bifurcation of the flaw occurred near the lower end. Figure D-1

shows the locus of the flaw traced on the inner surface of the vessel, as well as the through-wall contour of the arrested flaw.

- Stretch zones in the cladding were observed on the inner surface above the flaw (see photograph in Fig. D-2), but no breaching or tearing of the cladding was found.

None of the other flaws initiated, but slight stretch zones were visible on the inner surface above the flaws.

The TSE-8 experiment provides compelling evidence in support of assumptions employed in the FAVOR model regarding the transition of finite-length flaws to infinite (uniform depth) flaws following cleavage initiation. As shown in Figs. D-1 and D-2, flaw #3 initiated and propagated long and deep in cleavage beneath the clad layer when subjected to thermal-shock loading. The intact cladding (with stretch zone) immediately above the flaw did not impede that substantial cleavage run-arrest event. This experimental evidence was factored into development of the FAVOR LEFM model that assumes finite-length flaws transition instantly to infinite flaws upon cleavage initiation. An additional (computational) simplification of the model assumes that the clad layer is breached above the post-initiation infinite flaw. The latter assumption, required for the linear elastic modeling of the cladding, is consistent with the outcome of the TSE-8 experiment.

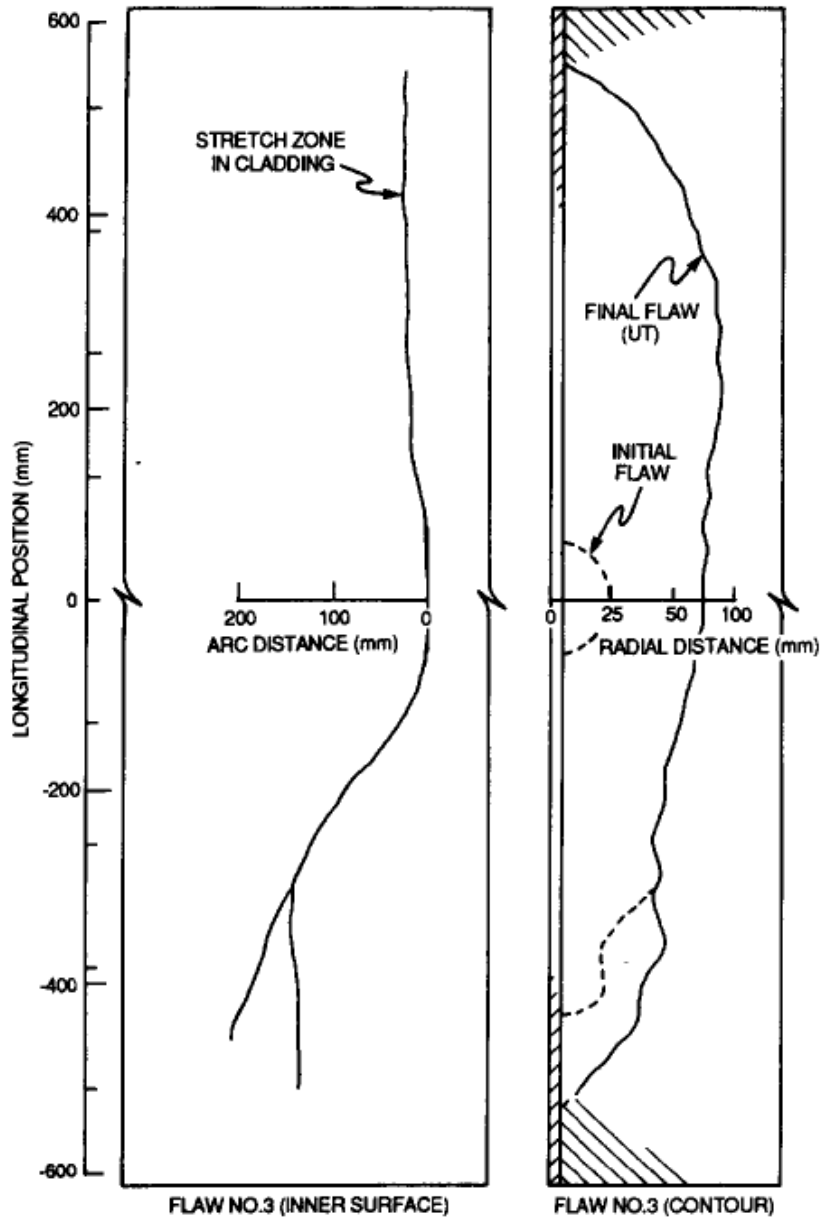


Fig. D-1 Stretch zone and UT indications for flaw #3 extension by cleavage propagation beneath clad layer in TSE-8 (Fig. 8 in Ref. D1).

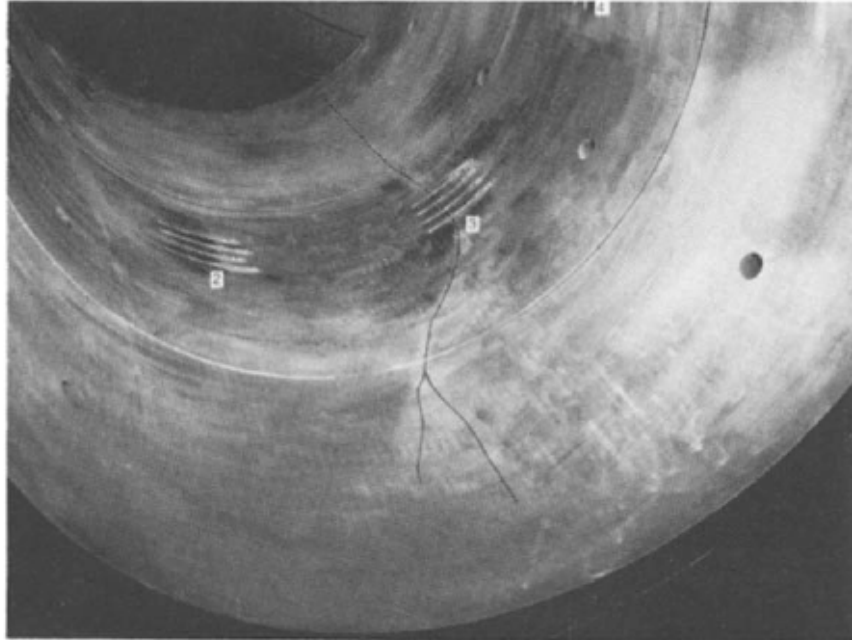


Fig. D-2 Stretch zone in cladding above extended flaw #3; center of stretch zone marked with pen; note bifurcation of flaw in foreground (Fig. 9 in Ref. D1).

References

- D1 R. D. Cheverton, J. W. Bryson, D. J. Alexander, and T. Slot, "Thermal shock experiments with flawed clad cylinders," Nuclear Engineering and Design 124 (1990) 109-119

APPENDIX E: KEY ASPECTS OF THE CLAD/BASE MODEL IN FAVOR

This Appendix summarizes key aspects of the model of the cladding-to-base metal interface as implemented in the FAVOR code²⁰. All of this information can be found in the FAVOR theory manual [E3]; it is repeated here for convenience. Specific features of the model discussed herein include the following:

- LEFM analyses of flaws subjected Mode I loading
- Calculation of K_I factors in clad and base material using superposition/influence coefficient techniques
- Determination of clad-base stress-free temperature
- Modeling of through-wall weld distribution of residual stress

Mode I Loading and Linear Elastic Fracture Mechanics Assumptions

The linear-elastic stress model of the FAVOR code treats circumferential flaws exposed to a generalized plane-strain stress field. The flaws are, therefore, assumed to experience only a Mode I loading, where the principal load is applied normal to the crack plane, thus tending to open the crack. It is also assumed that the plastic zone around the crack tip for the shallow surface breaking flaw is fully contained, and the overall deformation-load response of the structure is linear, which is validated with elastic-plastic analysis. For these high-constraint conditions, the principles of linear-elastic fracture mechanics (LEFM) apply when calculating driving forces (applied K_I) for the crack.

Method of Superposition and Stress Intensity Factor Influence Coefficients

The FAVOR code uses the method of superposition to calculate the applied K_I . The method of superposition requires the calculation of stress intensity factor influence coefficients (SIFICs). The main concept is that the results of a finite element stress analysis of an un-cracked vessel can be combined with previously derived SIFICs to calculate accurate values of applied K_I for a range of flaw geometries subjected to an arbitrary stress distribution. The FAVOR Theory manual [E3] provides further technical details of the method of superposition and SIFICs. FAVOR uses this method because it provides considerable generality to calculate K_I for complex time-history loading conditions. Equally important is that considerable economy is achieved with this approach because 3-D models are required only once to calculate the SIFICs. FAVOR includes a comprehensive database of SIFICs for internal and external surface breaking flaws applicable to

²⁰ The clad/base model employed in this study is identical to that used in the PTS re-evaluation effort [E1-E2].

pressurized water reactor (PWR) and boiling water reactor (BWR) geometries. This database provides a capability to quickly calculate accurate values of K_I over a range of surface breaking flaw geometries for complex time history loading conditions. These values of K_I are in close agreement with those generated by the general-purpose finite element code ABAQUS [E4, E5].

Details Regarding the FAVOR methodology for Calculating K_I

Figure E-1 illustrates the through-wall stress profile at an arbitrary transient time. The stress discontinuity arises from the difference in thermal-elastic properties of the stainless steel clad and base materials. When using superposition and SIFICs for 3-D flaws, it is necessary to represent the stress distribution in the uncracked cylinder with a third-order polynomial. Therefore, the discontinuity in the stress at the clad-base material interface presents a problem inasmuch as a third-order polynomial cannot represent a discontinuity. The solution to this problem adopted by FAVOR is described in the following paragraphs.

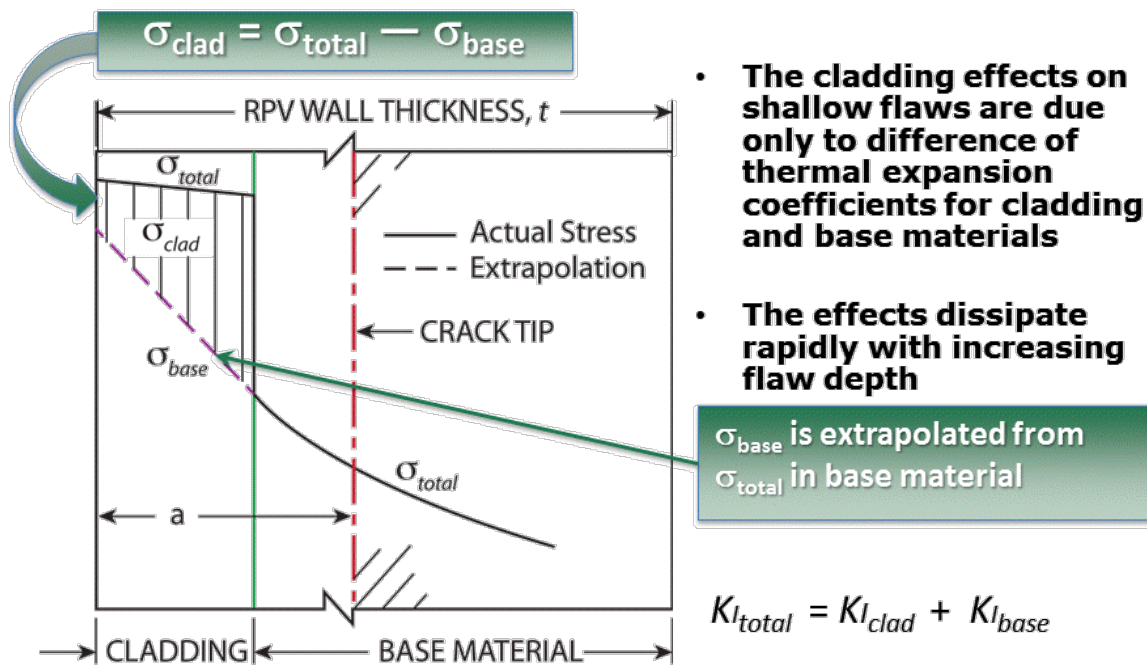


Fig. E-1 Cladding model implemented in FAVOR.

To accommodate the stress discontinuity, a methodology was developed in which SIFICs were calculated separately for the stresses in the clad and base regions. Figure E-1 illustrates the cladding model implemented in FAVOR. The presence of a thin layer of stainless steel cladding on the inner surface of RPVs can have a significant effect on the K_I values for inner-surface breaking flaws because of high thermal stresses generated in the clad during a thermal transient.

FAVOR applies the superposition technique and stress intensity factor influence coefficients (SIFICs) when calculating the K_I for surface breaking flaws.

At a specific transient time, the crack-opening stress profile through the wall generated from the thermal-stress analysis of the uncracked RPV is applied to postulated flaws. As illustrated in Fig. E-1, there is a stress discontinuity on the clad/base interface due to the different material properties of cladding and base materials. The total stress (σ_{total}) in the base metal is linearly extrapolated into the cladding material, and the difference of the total stress in the cladding ($\sigma_{total-clad}$) and the extrapolated σ_{base} is defined as σ_{clad} . For an arbitrary stress distribution and for the case of a semi-elliptic surface flaw, the truncated stress distribution in the base material can be approximated by a third-order polynomial of the form

$$\sigma_{total-base}(a) = C_0 + C_1 a + C_2 a^2 + C_3 a^3 \quad (E-1)$$

where C_0 , C_1 , C_2 , and C_3 are curve fit coefficients (calculated by a generalized least-squares regression analysis in FAVLOAD) for the through-wall stress distribution in the base material at a specific transient time for the uncracked structure across the crack depth a .

For the cladding material,

$$\sigma_{clad}(a) = C_4 + C_5 a \quad (E-2)$$

the C_4 , C_5 are curve fit coefficients for the through-wall stress distribution in the cladding material at a specific transient time for the uncracked structure across the crack depth a .

For finite length internal surface breaking flaws, to accommodate the stress discontinuity associated with the cladding, SIFICs were calculated separately for the base material and the clad such that the total K_I , designated as K_{Itotal} , is the sum of the contribution of the base material, designated as K_{Ibase} , and the clad, designated as K_{Iclad} ,

$$K_{Ibase}(a) = (K_0 C_0 + K_1 C_1 + K_2 C_2 + K_3 C_3) \sqrt{\pi a} \quad (E-3)$$

$$K_{Iclad}(a) = (K_4 C_4 + K_5 C_5) \sqrt{\pi a} \quad (E-4)$$

(K_0 , K_1 , K_2 , and K_3) are SIFICs pre-calculated for each flaw geometry (depth and length) for the base material, and (K_4 and K_5) are SIFICs pre-calculated for each flaw geometry (depth and length) and clad thickness for the cladding material. This procedure has been verified against ABAQUS analyses that do not require the separation of base and clad stresses needed for the SIFIC approach [E4, E5].

Determination of Stress-Free Temperature (SFT)

The recommended clad-base SFT of 488 °F, from which differential thermal expansion (DTE) stresses are calculated, was developed in a 1999 study [E6] from a combination of (1) experimental measurements taken from a RPV shell segment made available from a cancelled pressurized-water reactor and (2) finite element stress analyses using temperature-dependent thermal-elastic material properties; that process is illustrated in Fig. E-2.

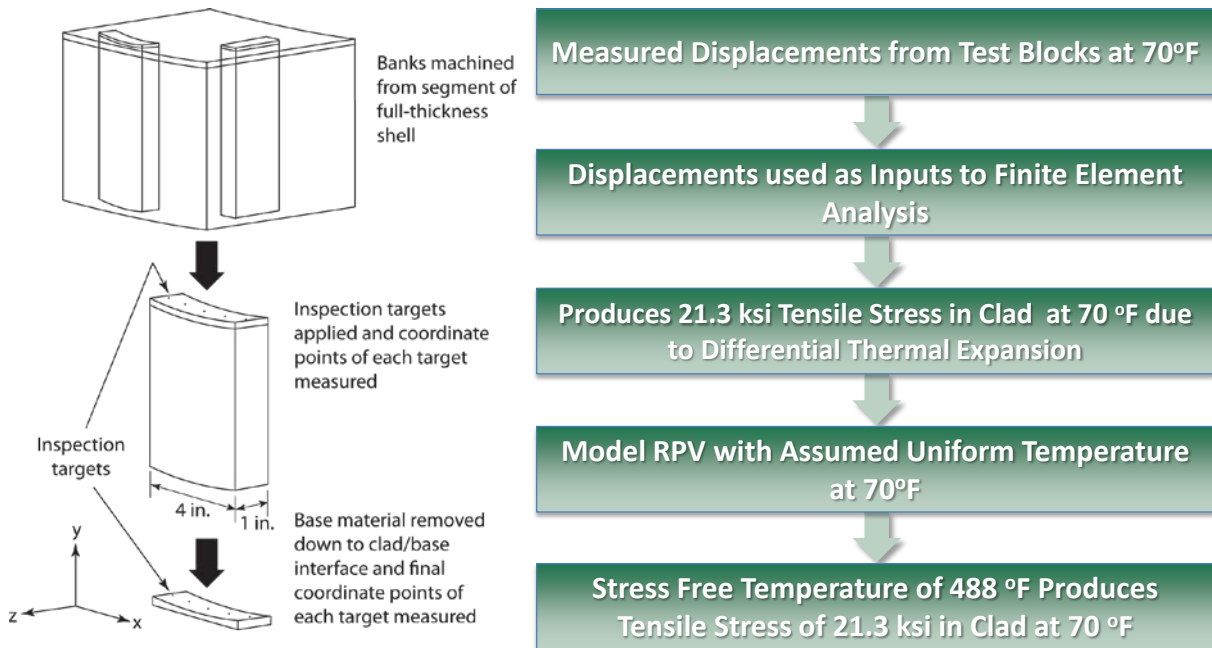


Fig. E-2 Stress-free temperature was determined through combined experimental measurements and finite element analysis.

A block of the shell material (with intact cladding) measuring 10 in. square and having the full-RPV-wall thickness was used. Two smaller full-thickness blocks were saw-cut from this block (see Fig. E-2). Each of these smaller blocks was machined to a parallelepiped 4 in. x 1 in. x 91/4 in. thick (shell thickness). One block was taken with the clad-layer length (4 in. dimension) in the circumferential direction of the shell (parallel to the cladding deposition direction) and the other in the longitudinal direction (transverse to the cladding deposition direction). As part of the machining process, inspection points (fiducial marks) were applied at points on the original and machined-end surfaces of the clad layer. These points were drilled to a depth not exceeding 0.010 in. using a conical point drill. This procedure assured an inspection point with uniform dimensions for repeatability of the subsequent measurements.

Precision dimensional inspections were performed to measure the x , y , and z coordinates of each of these fiducial marks. After the initial measurements, the base layer was machined away from the plate material until the clad/base metal fusion zone was completely revealed, as illustrated in Fig. E-3. To estimate the mid-thickness of the fusion zone, visual inspection was used to judge when approximately equal amounts of plate and clad materials were exposed on the machined surface. The location of the fiducial marks on the remaining clad layer parts were re-measured to quantify the distortion imparted to the block by the removal of the base material. The change in shape of the parts was then determined by subtracting the initial coordinates of each inspection point from the final (deformed) coordinates. Using the deformed coordinates for each fiducial mark, maximum and average values (for the sets of measurements) of circumferential and longitudinal strain were calculated; those values are shown in Table E-1.

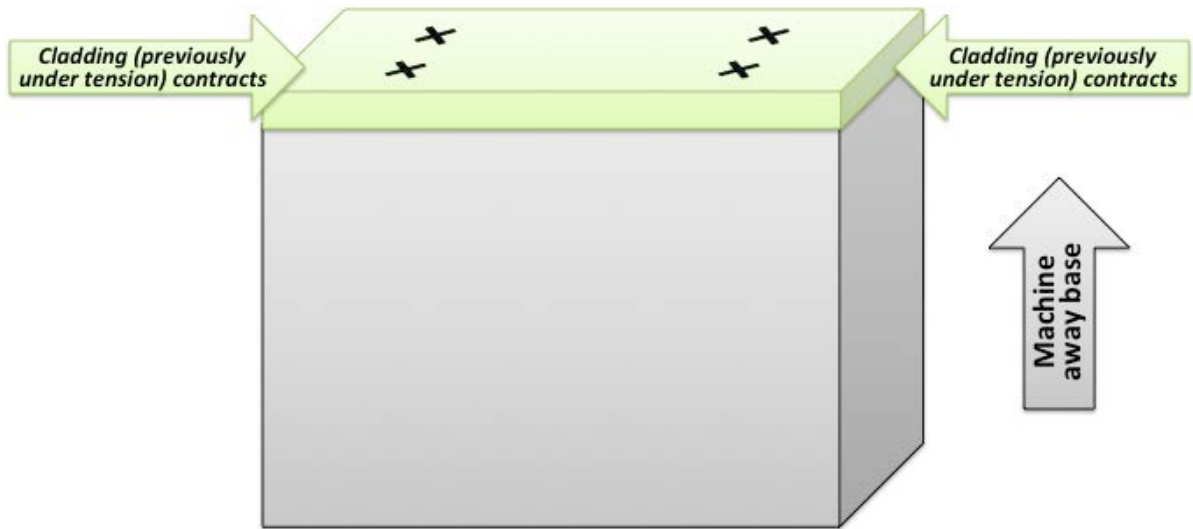


Fig. E-3 Inspection targets applied to clad inner surface prior to machining away the base material.

The strains in Table E-1 were used as boundary conditions for a finite-element analysis to determine the maximum and average values of clad residual (tensile) stress components that were relieved by the machining step. The residual stresses calculated from that analysis for the two cases considered, i.e., maximum and average strains, are given in Table E-2.

Table E-1 Strains* Measured when Cladding was Released from the Base Material of a RPV Shell Segment

	Strain ϵ_{xx} (in/in)	Strain ϵ_{yy} (in/in)
Maximum	-0.00086	-0.00041
Average	-0.00070	-0.00033

*Strain values were hand-calculated from measured changes in coordinates of fiducial marks depicted in Fig. E-3.

Table E-2 Stress Components Computed from Strains Measured in Cladding taken from a RPV Shell Segment; stresses are calculated at room temperature (70 °F)

Strain Combination	Circumferential Stress (ksi)	Longitudinal Stress (ksi)
Maximum	26.2	17.8
Average	21.3	14.4

The average value of circumferential stress in Table E-2 was used to calculate SFT; the circumferential and longitudinal stresses would not necessarily go to zero simultaneously, so the calculation was based on the larger circumferential component. That application of FAVOR (utilizing temperature-dependent thermal-elastic material properties) determined that a through-clad, average tensile stress of 21.3 ksi at room temperature of 70 °F corresponds to a value of SFT = 488 °F.

Determination of SFT from combined RPV data/analysis allows FAVOR to account accurately for effects of (1) residual stresses produced by weld deposition of the cladding and (2) mismatch in CTE between the cladding and base metal during any loading transient specified by pressure/temperature versus time curves. Additional details of the procedure for determining the SFT are given in Ref. [E6].

Residual Stress Produced by the Structural Welds in the RPV Shell

The FAVOR code incorporates a through-wall weld residual stress [E6] distribution derived from a combination of

- experimental measurements taken from a RPV shell segment from a cancelled PWR plant and
- finite-element thermal and stress analyses

Residual stresses in a RPV structural weld are caused by (a) the clad-base metal differential thermal expansion (which were quantified by use of the SFT, as just described), and (b) the residual stresses generated by the structural welding process that are not completely relaxed by the post-weld heat-treatment. Data required for calculation of the weld residual stresses were obtained by cutting a radial slot in the longitudinal weld in a shell segment from a RPV, and measuring the deformation of the slot width after cutting. The measured slot openings are assumed to be the sums of the openings due to the clad-base material differential thermal expansion and the weld residual stresses. Slot opening measurements were made during the machining of full-thickness clad beam specimens with 2-D flaws. The blanks measured 54 in. long (circumferential direction), 9 in. wide (longitudinal direction), and 9 in. thick (radial direction). The blanks were cut so as to have a segment of a longitudinal seam weld from the original RPV at the mid-length of the blank. Using the wire-electro-discharge machining process, a slot was cut along the weld centerline in a radial direction from the inside (clad) surface of the blank. Measurements were made on three specimens having final slot depths of 0.045 in., 0.90 in., or 4.50 in., respectively. After machining, the widths of the slots were measured along each radial face of the blanks. Finite element analyses were used to develop a through-thickness stress distribution that gave a deformation profile matching the measured values. This distribution is shown in Fig. E-4, where the contribution from differences in CTE for the clad and base materials has been removed. Additional details concerning the estimation of the residual stress distribution used in FAVOR are given in ref. [E6].

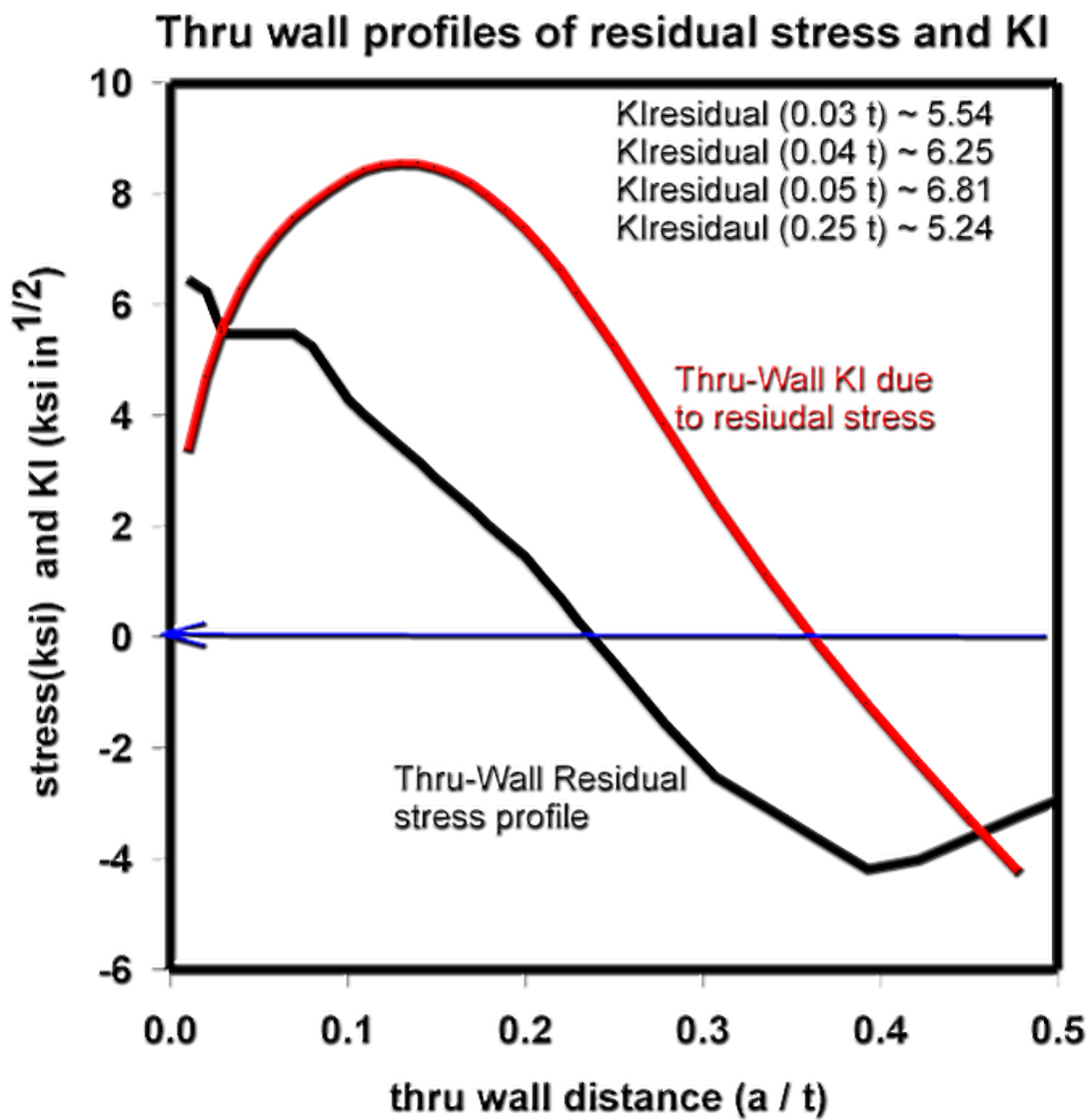


Fig. E-4 Through-wall profile of residual stresses and K_I used in the FAVOR code.

REFERENCES

- E1. M. EricksonKirk, et al., *Technical Basis for Revision of the Pressurized Thermal Shock (PTS) Screening Limit in the PTS Rule (10 CFR 50.61) – Summary Report*, NUREG-1806, Vol. 1, U.S. Nuclear Regulatory Commission, August, 2007.
- E2. M. EricksonKirk, et al., *Technical Basis for Revision of the Pressurized Thermal Shock (PTS) Screening Limit in the PTS Rule (10 CFR 50.61) – Appendices*, NUREG-1806, Vol. 2, U.S. Nuclear Regulatory Commission, August, 2007.
- E3. P.T. Williams, T.L. Dickson, and S. Yin, *Fracture Analysis of Vessels – Oak Ridge FAVOR, v12.1, Computer Code: Theory and Implementation of Algorithms, Methods, and Correlations*, ORNL/TM-2012/567, November 2012, Oak Ridge National Lab, Oak Ridge, TN.
- E4. B.R. Bass, et al., “Verification and Validation of FAVOR Code – Deterministic Load Variables,” ORNL/NRC/LTR-04/11, March, 2004, Oak Ridge National Lab, Oak Ridge, TN.
- E5. S. Yin, T.L. Dickson, P.T. Williams, and B.R. Bass, “Verification of New Capabilities of Deterministic Load Module of FAVOR 09.1”, Paper number PVP2010-25439, Proceedings of 2010 ASME Pressure Vessels and Piping Division Conference July 18-22, 2010, Bellevue, Washington.
- E6. T.L. Dickson, et al., “Evaluations of Margins in the ASME Rules for Defining the P-T Curve for a RPV, Proceedings of the 1999 ASME Pressure Vessel and Piping Division Conference, July 1999, Boston, MA.

BIBLIOGRAPHIC DATA SHEET

(See instructions on the reverse)

1. REPORT NUMBER
(Assigned by NRC, Add Vol., Supp., Rev.,
and Addendum Numbers, if anv.1

ORNL/TM-2015/59531/REV-01

2. TITLE AND SUBTITLE

The Effect of Shallow Inside-Surface-Breaking Flaws on the Probability of Brittle Fracture of Reactors Subjected to Postulated and Actual Operational Cool-Down Transients: A Status Report. Rev 01.

3. DATE REPORT PUBLISHED

MONTH	YEAR
February	2016

4. FIN OR GRANT NUMBER

N6438

5. AUTHOR(S)

B. R. Bass, T. L. Dickson, P.T. Williams, H. B. Klasky and R. H. Dodds, Jr.

6. TYPE OF REPORT

technical

7. PERIOD COVERED (Inclusive Dates)

8. PERFORMING ORGANIZATION - NAME AND ADDRESS (If NRC, provide Division, Office or Region, U.S. Nuclear Regulatory Commission, and mailing address; if contractor, provide name and mailing address.)

Probabilistic Structural and Material Modeling (ProSaMM) Program
Oak Ridge National Laboratory
P. O. Box 2008, Mail Stop 6085
Oak Ridge, TN 37831-6085

9. SPONSORING ORGANIZATION - NAME AND ADDRESS (If NRC, type "Same as above"; if contractor, provide NRC Division, Office or Region, U.S. Nuclear Regulatory Commission, and mailing address.)

Division of Engineering
Office of Nuclear Regulatory Research
U. S. Nuclear Regulatory Commission
Washington, DC 2055-0001

10. SUPPLEMENTARY NOTES

11. ABSTRACT (200 words or less)

Reactor pressure vessel (RPV) geometries subjected to normal cool-down transients were analyzed using the probabilistic fracture mechanics (PFM) code FAVOR. The objective was to determine trends for conditional probability of initiation (CPI) and failure (CPF) as a function of inner diameter (ID) surface-breaking flaw depth. The analyses produced unanticipated results, i.e., shallow, circumferential, ID surface-breaking flaws (1) dominate the RPV failure probability and (2) exhibit CPI and CPF values that exceed those for the 1/4 t flaw referenced in the ASME Code, Section XI, Appendix G. Those results were observed not only for a majority of cases using the current practice procedures in the ASME Code, but also for the EPRI-MRP 250 risk-informed methodology.

The above-referenced analyses of cool-down transients demonstrated trends in CPI and CPF for ID surface-breaking flaws that vary non-monotonically with flaw depth, reaching a global maximum for very shallow flaws just penetrating the base material. That domination of PFM results by very shallow, surface-breaking flaws is shown to be due totally to the additional crack driving force generated for shallow flaws by the mismatch in coefficient of thermal expansion (CTE) between cladding and base material; that CTE contribution is demonstrated to diminish rapidly as flaw depth increases.

12. KEY WORDS/DESCRIPTORS (List words or phrases that will assist researchers in reading the report.)

FAVOR, Shallow Flaw, Stress Intensity Factor, Reactor Pressure Vessel (RPV), Failure Probability

13. AVAILABILITY STATEMENT

unlimited

14. SECURITY CLASSIFICATION

(This Page)

unclassified

(This Report)

unclassified

15. NUMBER OF PAGES

16. PRICE